PERSISTENT PHOTOCONDUCTIVITY
OF STRONTIUM TITANATE

By

VIOLET MARY POOLE

A dissertation submitted in partial fulfillment of
the requirements for the degree of

DOCTOR OF PHILOSOPHY

WASHINGTON STATE UNIVERSITY
Department of Physics and Astronomy

JULY 2016

To the Faculty of Washington State University:

The members of the Committee appointed to examine the dissertation of VIOLET MARY POOLE find it satisfactory and recommend that it be accepted.

Matthew D. McCluskey, Ph.D., Chair

Gary S. Collins, Ph.D.

Yi Gu, Ph.D.

ACKNOWLEDGEMENTS

This work is supported by the U.S. Department of Energy, Office of Basic Energy Sciences, Division of Materials Sciences and Engineering under Award DE-FG02-07ER46386.

I would like to thank all the people who made this work possible. First off, my advisor, Dr. Matt McCluskey, for guiding my research, and his patience. His in depth knowledge of the subject and superior editing skills have shaped my research enormously. I would also like to thank the other members of my committee: Dr. Gary Collins and Dr. Yi Gu. I also thank Marianne Tarun for first discovering PPC in STO.

I thank my collaborators who contributed valuable measurements and insight to this work: Dr. Yi Gu and his graduate students, Shengwen Zhou and Qiaoming Wang, for the KPFM measurements and Mary Ellen Zvanut and J. Dashdorj at the University of Alabama at Birmingham for EPR spectra.

I thank my fellow graduate students, for the many interesting scientific discussions and friendship throughout my years here. Specifically, Caleb Corolewski for showing me how to operate all of the machines in our lab and keep them running. Jacob Ritter for help with Seebeck measurements and listening to me complain when lab equipment broke down. I would also like to thank a former post doctoral student, Narendra Parmar, who often worked in our lab, for help in lab, especially with the Hall-effect machine.

I would like to thank Washington State University and the Department of Physics and Astronomy for giving me the opportunity to do this research. I thank the professors I worked for prior to joining McCluskey's research group, Guy Worthey and Sukanta Bose for their time and patience. I also thank the graduate school, and Mary Stormo, for letting me have the extensions needed to finish this work. I thank the wonderful people at Owen Science Library for finding so many obscure references for me. I thank the wonderful department office staff, Laura Kruger, Mary Guenther, Kris Boreen, Robin Stratton, Sabreen Dodson, and Leslee Kimbleton, for there valuable work throughout the years. Finally, I thank the janitors, such as Susan Lewis.

Lastly, I would like to thank all my friends and family for their encouragement, support and friendship throughout the years. Especially: my Mom, Dad and Brother, Tamie, Sam, Ashley and Justin, and of course Josh.

PERSISTENT PHOTOCONDUCTIVITY
OF STRONTIUM TITANATE

Abstract

by Violet Mary Poole, Ph.D.
Washington State University
July 2016

Chair: Matthew D. McCluskey

Strontium titanate ($SrTiO_3$) is a transparent conducting oxide with a range of interesting properties, including a large, temperature-dependent dielectric constant and superconductivity at low temperatures. It has a wide indirect band gap of 3.2 eV at room temperature. Annealing in a reducing atmosphere with additional strontium oxide (SrO) powder at 1200^{o}C results in the creation of native defects. These annealed samples show persistent photoconductivity (PPC) at room temperature, when exposed to light of energy 2.9 eV or greater. The three or more order of magnitude change in resistance persists long after the light is turned off. This effect is attributed to an electron being excited from an acceptor defect, with a large barrier for recapture, to the conduction band.

This work investigates many of the changes that occur and factors that affect PPC. The right amount of SrO powder is crucial to the formation of PPC. The presence of some oxygen vacancies is also necessary for PPC; however, too many will mute the dramatic change in resistivity. Peaks at 430 nm and 520 nm appear in the visible region of the spectrum. The peak at 430 nm is due to iron, while the peak at 520 nm has not been identified. The infrared region of the spectrum also shows changes. First, the intensity of the transmitted signal drops significantly after light exposure, due to free carrier absorption.

Additionally, a hydrogen line at 3500 cm^{-1} and satellites are often observed in as-received samples. The satellites disappear during annealing and return during PPC. The hydrogen lines have the same thermal kinetics as the 520 nm peak. Hydrogen lines at 3355 and 3384 cm^{-1}, if present, will prevent PPC. An exposed chip can be erased (i.e. returned to its pre-light exposed

state) by using a heat treatment.

Erasing and polishing an annealed chip prior to light exposure can result in weakly *p*-type behavior with high mobility holes ($>$ 100 cm^2/Vs). This is an order of magnitude higher than those commonly measured for electrons (5-10 cm^2/Vs). The average hole densities were in the 10^9-10^{10} cm^{-3} range, consistent with a deep acceptor.

TABLE OF CONTENTS

LIST OF TABLES

LIST OF FIGURES

Dedication

For Seren, my little star.

Chapter ONE

INTRODUCTION

1.1 Outline of Dissertation

Important basics of semiconductor physics are reviewed in Chapter 1. Chapter 2 discusses the experimental techniques used in this work. Chapter 3 looks at persistent photoconductivity (PPC) and the changes that can be observed when this occurs. The role of hydrogen and oxygen are discussed in Chapter 4. Erasing PPC is discussed in Chapter 5. Electrical properties are discussed in Chapter 6, while the special case of *p*-type measurements are in Chapter 7. The effect of changing the annealing conditions is explored in Chapter 8. The line shape from free carrier absorption in the IR region is discussed in Appendix C.

1.2 Semiconductor Basics

Matter in the solid state is either noncrystalline or crystalline [Long, 1968]. Crystals are composed of atoms arranged in a highly ordered, repeating structure called a lattice, with covalent or ionic bonds between neighboring atoms [Jarzebski, 1973]. Elemental semiconductors are covalently bonded, while compound semiconductors all exhibit some degree of ionic bonding. This structure gives crystals interesting electronic properties. Semiconductors are neither conductors, which allow current to flow easily, nor insulators, which prevent the flow of current. All modern electronic devices, from phones to television and computers, rely on the unique way current flows in semiconductors to function.

The electrons in the crystal experience a periodic potential. A crystal can be visualized as an entity composed of immobile positive ions in a regular array, with a cloud of valence electrons around them. The core electrons are so tightly bound they can essentially be thought of as part of the positive ions. Each valence electron moves in the average potential field of all positive ions and the remaining electrons. The regular lattice of atoms bonded together have vibrational properties. The thermal motion of the atoms around their equilibrium positions within the lattice cause collective modes of vibration that propagate through the crystal.

Electrons are confined to a number of possible energy states by quantum mechanics. These energy levels become bands since crystals are composed of millions of atoms and electrons. At absolute zero, an intrinsic semiconductor has a band structure that consists of entirely filled or completely empty bands. The ground state valence electrons of the atoms fill up the lower levels, with the highest filled level being the valence band. The lowest unoccupied energy band is the conduction band. The difference in energy between the valence band edge and the conduction band edge is the forbidden zone called the band gap. For an electron in the valence band to jump up to the conduction band, a certain minimum energy is needed, that of the band gap. When the electron leaves the valence band, a hole, which carries positive charge, is left behind. The probability of an individual electron gaining this necessary energy increases with increasing temperature. The electron in the conduction band is analogous to a free electron in a conductor and can carry current. The hole in the valence band also acts like a positive charge carrier, moving between neighboring atoms freely.

The band gap of a semiconductor can be either direct or indirect. Direct absorption is where a photon of sufficient energy excites an electron into the conduction band. This can easily be measured by looking at the optical absorption data, where the threshold at frequency ω_g measures the band gap $E_g = \hbar\omega_g$. The band gap energy can also be obtained from an Arrhenius plot of the logarithm of carrier concentration versus the inverse of temperature. The momentum of the electrons and holes is the same in the conduction and valence bands, respectively. However, in an indirect band gap semiconductor, the conduction band minimum and the valence band maximum are widely separated in wavevector $\mathbf{k}$ space. To conserve momentum, the indirect transition involves both a photon and a phonon, or quantum of lattice vibration. The phonon energy $\hbar\Omega$, (10 to 30 meV) is much smaller than that of the band gap (1 to 4 eV), so it results in an approximately horizontal transition in energy. This results in weaker optical absorption near the threshold, and the indirect transition is characterized by $\hbar\omega = E_g + \hbar\Omega$.

The properties of the semiconductor will change significantly when a small amount of an impurity is added, either unintentionally or by design (doping). On the order of one impurity atom per 10 million atoms of the crystal is all that is required to change, for instance, the conductivity. The crystal structure is no longer perfectly repeating so the translational symmetry is broken.

This will introduce new vibrational modes, called local vibrational modes (LVMs). These are often localized in both real space and frequency space. When a light atom, such as hydrogen, is present in the crystal bonded to one of the lattice atoms, LVMs arise that correspond to narrow infrared (IR) absorption peaks if the atomic oscillations cause a change in the dipole moment. Additionally, if the defect is electrically active, it will introduce energy levels within the band gap.

There are many types of defects a crystal structure can have, but for simplicity only lattice substitution is discussed here. If the impurity has more valence electrons than the host atom that it replaces, it is called a donor. On the other hand, if the impurity atom has fewer electrons than the regular lattice site occupant, it is called an acceptor. If the impurity will easily accept or give up an electron it is called a shallow acceptor or donor, respectively. These can be modeled as an electron or hole orbiting around an ion, analogous to a hydrogen atom. By using the effective mass m^* of the electron in the crystal's periodic potential, m_e as the mass of the free electron, and the relative dielectric constant ε of the material, the binding energy for the electron is:

$$E = \frac{13.6\ \text{eV}}{\varepsilon}\frac{m^*}{m_e} \tag{1.1}$$

The extra electron can be easily excited from the shallow donor; i.e., the energy level lies near the conduction band. A shallow acceptor has its energy level located close to the valence band, and it will easily take on an extra electron, leaving a mobile hole in the valence band. At room temperature, most electrons (holes) are promoted into the conduction (valence) band. If the energy required to add or remove electrons from the impurity is too large, the defect is no longer considered shallow, and instead is a deep acceptor or donor. These impurities are more complicated, and often have their energy levels somewhere in the middle of the band gap.

Semiconductors have two types of defects, intrinsic or extrinsic. Intrinsic or native defects involve only atoms that are present in a perfect crystal. One example is a vacancy, which is a missing atom. Extrinsic defects, on the other hand, are composed of atoms that are not part of the normal crystal structure, such as phosphorous in silicon. In intrinsic semiconductors the number of holes and electrons are equal. Extrinsic doped semiconductors can have an excess of either electrons or holes. In general, semiconductors will contain a mixture of donor and acceptor impurities. P-type (n-type) semiconductors will have the majority of charge carriers be from holes (electrons) introduced by a predominance of acceptor (donor) impurities.

1.3 Transparent Oxide Semiconductors

Materials that transmit light in the visible region of the spectrum and simultaneously conduct electricity are vital to the development of solar cells, flat panel displays and light emitting diodes. However, the coexistence of both of these properties is unexpected from standard solid-state physics concepts [Jarzebski, 1973]. The large band gap (3-4 eV) required for transparency is normally accompanied by insulating properties, while metals and semiconductors with smaller band gaps readily conduct electricity but are opaque to visible light. One class of materials, transparent conducting oxide (TCO), semiconductors are unique and combine these two features not typically found together, optical transparency and electrical conductivity.

The first transparent conductive oxide reported was a thin film of CdO discovered in 1907 [Badekar, 1907]. The most commonly used TCO materials today exist in the form of thin films of In_2O_3, SnO_2 and ZnO, which have optical transmittances of greater than 80% in the visible range of the spectrum and sheet resistances around 100 Ω/cm^2 [Treharne, 2011]. This unique feature of oxide materials could add many new capabilities to electronic devices. Flat-panel displays and solar cells use an indium based oxide material to achieve this. However, indium is rare and expensive, so other materials are desired. Many other *n*-type TCOs can be produced rather cheaply and are quite stable. *P*-type is harder, but some TCOs with useful hole conductivities have been found, such as $CuAlO_2$ [Bright, 2007]. Another TCO, zinc oxide (ZnO), has reports of *p*-type doping, but the reliability is being questioned as most have not been reproducible [Bierwagen et al., 2008].

The origins of the conductivity in TCOs are not well understood due to occurrence of ionic bonds in the oxide material [Jarzebski, 1973]. The transport mechanism of the current carriers is more complex than in elemental semiconductors or in compounds with covalent bonds. In the absence of donor or acceptor states in the band gap, the thermal excitation is negligible and there are no free carriers. If however there is a small population of shallow donors, thermal excitation allows electrons to be promoted into the conduction band and the Fermi level is raised from mid gap to just below the conduction band [Treharne, 2011]. Oxides tend to form shallow native point defects, such as oxygen vacancies, where the concentration depends on the temperature and partial pressures of the constituents, such as oxygen, surrounding the crystals. Additionally, oxide compounds can show large deviations from stoichiometry [Tuller and Bishop, 2011]. If the concentration of donor states reaches a critical density, the impurity band merges into the conduction band and metallic like behavior is obtained from the free charge carriers [Mott and Friedman, 1974]. Additionally, hydrogen can also be readily incorporated into the lattice, and dramatically affect its electrical properties [Norby, 2009, Minami, 2005].

Despite these challenges, this class of materials has already found many practical applications in devices requiring a transparent contact. Some examples include use in transparent contacts for solar cells and for enhancement of optical power output in light emitting diodes [King and Veal, 2011]. Additionally, fluorine doped SnO_2 has been employed extremely successfully as a low emissivity coating for architectural applications [Treharne, 2011]. $InGaO_3(ZnO)_5$ has been successfully used as the channel layer in an all oxide transparent field effect transistor [Nomura et al., 2003]. In addition to their electronic applications, oxides have been used in hydrogen fuel cells [Tuller and Bishop, 2011].

1.4 Strontium Titanate

Strontium titanate (STO) has the chemical formula $SrTiO_3$. This transparent oxide has an indirect wide band gap of 3.2 eV at room temperature [Trepakov et al., 2009]. It has a perovskite structure, which is cubic at room temperature (Figure 1). Below 105 K, the crystal undergoes a phase transition, where the oxygen octahedron rotates around the titanium atom and neighboring cells rotate in the opposite direction, lowering the symmetry to that of a tetragonal structure [Cowley, 1996]. STO is usually *n*-type [Moos et al., 1995]; however, its conductivity depends on the concentration of oxygen vacancy defects. Certain conditions of oxygen partial pressure may make it weakly *p*-type [Menesklou et al., 1999, Moos et al., 1995].

STO has a wide variety of applications, from being a photocatalyst used to hydrolyze water [Jeong et al., 2012] to serving as a substrate for growing high temperature superconductors [Nassau and Miller, 1988]. STO is also used as anodes in fuel cells [Ma et al., 2010], and in making high temperature oxygen sensors [Menesklou et al., 1999]. Chromium doped STO has been shown to have bi-stable resistance, which could possibly be used for resistance change memory

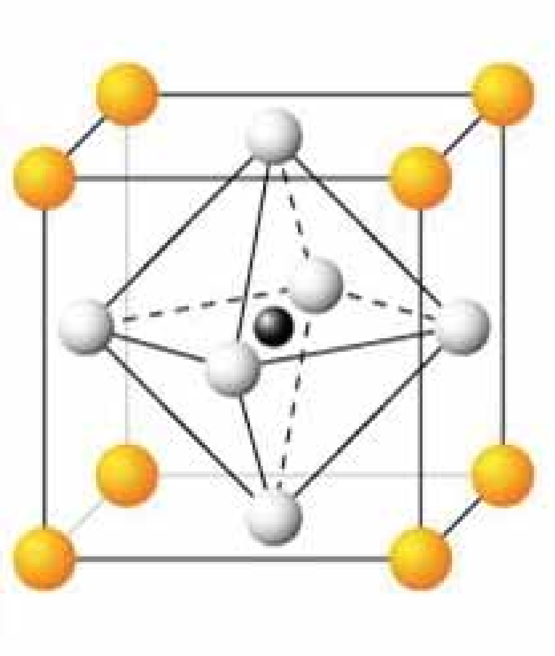

Figure 1: Ideal cubic representation of the perovskite structure of STO at room temperature. Orange represents strontium atoms, white is for the oxygen atoms, and black is the titanium atom.

[Janousch et al., 2007].

Recently Tarun et al. [Tarun et al., 2013] found that STO can be made to exhibit persistent photoconductivity (PPC) with a specific annealing treatment, which means the sample goes from being insulating to conductive upon light exposure. The enhanced conductivity persists even after the light is turned off. This could possibly open the door for the creation of photo-lithographic circuits.

1.5 Crystal Growth

My first attempts to induce PPC in STO by following Tarun's recipe only worked some of the time. Whether or not a sample had PPC after the annealing treatment, depended not on what manufacturing company it was from but on what batch it was from. All chips from the same batch would either work or not. We will discuss more about what makes a working or non-working sample in Chapters 3, 4, and 8. The batch to batch variability is related to how these crystals are created.

Most, if not all, commercial STO single crystal chips are grown by the flame-fusion (Verneuil) process. The principle of the Verneuil process involves melting the finely ground feed powder using an oxyhydrogen flame, and then crystallizing the melted droplets into boules [Levin, 1913]. Very high purity, 99.9995% or more, starting materials are required and extremely precise control over flame and feed rates are needed [Jarzebski, 1973]. While crystals grown with the Verneuil method are chemically and physically equivalent to naturally occurring crystals, the excess of oxygen present in the furnace can cause the formation of defects or even deviations from stoichiometry [Scheel et al., 1976]. Kulagin et al. [Kulagin and Hieckmann, 2012] point out that the results of studying various properties of STO by different authors has yielded significantly different results. This discrepancy is believed to be caused by the differences in the concentration and species of impurities present and possible deviations from stoichiometry that can occur during the growth process.

Chapter TWO

EXPERIMENTAL TECHNIQUES

Semiconductors are studied by a wide variety of different experimental techniques. Spectroscopy is the study of the interactions of electromagnetic radiation with matter. It provides a non-destructive way of characterizing semiconductors over a wide range of energies, since photons essentially provide pure energy for probing the lattice. The optical properties are linked to electronic and vibrational properties of the crystal, leading to well defined peaks in various regions of the spectrum that can provide information about the band structure and defects present in the crystal. Electrical characterization measures the basic properties of the semiconductor: resistivity, carrier density and mobility. These properties are crucial to the semiconductor's behavior within a circuit. Measurements are accomplished by attaching contacts to the material, and applying or measuring voltage, current or resistance across the contacts.

In the following sections, the basic experimental techniques used in this work are reviewed.

2.1 Fourier Transform Infared (FTIR) Spectroscopy

The infrared (IR) region of the spectrum, 100-5000 cm^{-1}, has energy sufficient to excite vibrations of the molecules in the crystal lattice [Harris and Bertolucci, 1978]. Quantum mechanically, only certain vibrational frequencies are allowed to exist in the crystal. A vibrational mode is only IR active if the atomic oscillations induced cause a change in the dipole moment [Hollas, 2004, McCluskey and Haller, 2012]. Water vapor and carbon dioxide absorb strongly in the IR region of the spectrum, so the optical compartment is often kept under vacuum.

Temperature can also influence the appearance of a peak. As a semiconductor heats up, the lattice will expand and thermal motion of the atoms increases, resulting in the populating of phonon modes. The oscillations of the neighboring host atoms can perturb the frequency of the defect mode, and cause damping of the vibrational mode of the defect. This results in a shifting and broadening of the peak present in the spectrum [Harris and Bertolucci, 1978, Hollas, 2004, McCluskey and Haller, 2012].

Radio frequency and microwave radiation has a low enough frequency that the detectors can respond fast enough to record the time domain spectra. For high frequency light, such as infrared and visible light, this is no longer true. The detectors cannot respond fast enough to the incoming radiation, so an interferometer is used to record the spectrum in the length domain rather than the frequency domain [Hollas, 2004]. This results in an interferogram, which is a plot of detected intensity of the interfered beam versus the optical path length [McCluskey and Haller, 2012]. All frequencies are being measured simultaneously, so measurements are quite fast. A Fourier transform allows us to covert this interferogram back into the frequency domain, giving an IR spectrum. This technique is called Fourier transform infrared (FTIR) spectroscopy, since it is mainly used in the infrared region of the spectrum.

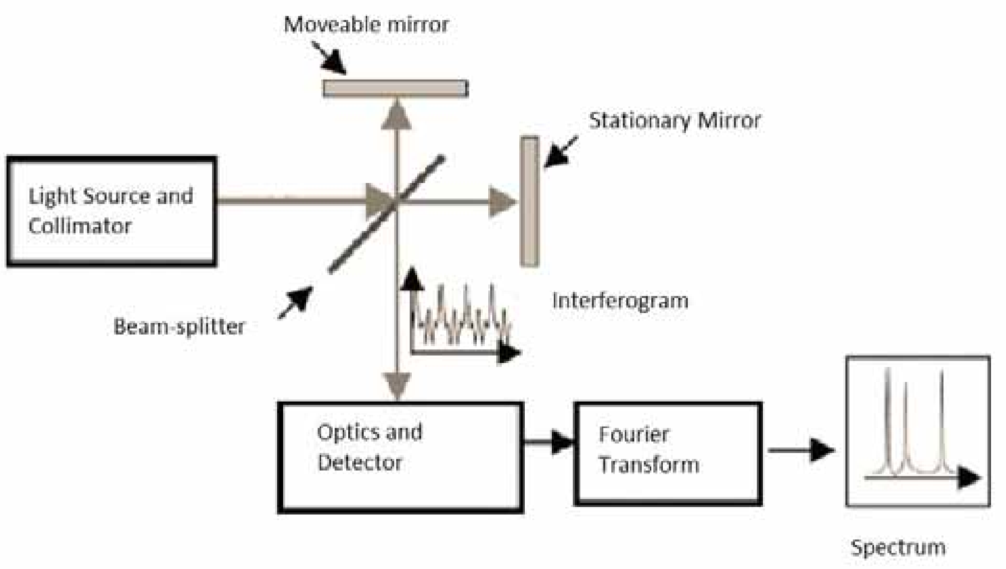

Figure 2: Schematic diagram of how the FTIR works. The main component is a Michelson interferometer.

Figure 2 shows the schematic diagram of a typical FTIR setup. The main optical component is a Michelson interferometer, where a beam of collimated light from a broadband source is directed towards a beamsplitter, dividing the light into two paths. The reflected light hits a movable mirror, while the transmitted light hits a stationary mirror. The two beams recombine and pass though the sample to the detector. Some of the radiation incident on the sample will be absorbed. Following the derivation given in [McCluskey and Haller, 2012], the two beams of light can be described as the superposition of two electromagnetic plane waves:

$$E = E_0 \exp[i(kz - \omega t)] + E_0 \exp[i(kz - \omega t + k\delta)] \tag{2.1}$$

where the optical path length difference δ depends on the position of the movable mirror. The motion of the mirror needs to be smooth for this to give good results. For each wavelength of light, if $\delta = n\lambda$ the two rays interfere constructively, while if $\delta = (2n+1)/2$ they interfere destructively. The average intensity hitting the detector is proportional to the square of the electric field incident on the detector.

$$I \propto \frac{1}{2}\langle E\rangle^2 = E_0^2[1 + \cos(k\delta)] \tag{2.2}$$

If we consider all the wavelengths of light, the intensity received by the detector can be written as:

$$I \propto \int_0^\infty E_0(k)^2 dk + \int_0^\infty E_0(k)^2 \cos(k\delta) dk \tag{2.3}$$

The first term is constant, so can be treated as an offset. The second term is called the interferogram, and varies with δ, which can written as:

$$I(\delta) = \int_0^\infty E_0(k)^2 \cos(k\delta) dk \tag{2.4}$$

where equation 2.4 is the Fourier transform of the spectrum $I_0(k)$. The desired spectrum described in the usual frequency domain can be obtained by taking the inverse Fourier transform:

$$I_0(k) \propto \int_0^\infty I(\delta) \cos(k\delta) d\delta \tag{2.5}$$

Notice that in equation 2.5 we are integrating the distance the mirror can move (δ), to infinity. In reality, the mirror can only move a finite distance, L. This introduces instrumental broadening, and limits the resolution of the spectrometer to $\sim 1/L$. Mathematically, the Fourier transform of the truncated interferogram results in a spectrum where peaks are surrounded by side lobes. These side lobes can be suppressed by multiplying he interferogram by an apodization function.

Additionally, the Fourier transform is usually computed by a dedicated computer running an algorithm called a Fast Fourier Transform (FFT).

The FTIR method of spectroscopy has several advantages over dispersive methods, where the light source is dispersed with a prism or diffraction grating, selecting only a narrow band of radiation that is incident on the sample at any one time. Because all frequency ranges are sampled simultaneously with each mirror oscillation, measurements are much faster than they would be if we scanned through each frequency. This is is known as the Fellgett advantage [Fellget, 1958], and allows many scans to be taken in a relatively short period of time and averaged to reduce noise. Additionally, dispersive spectrometers employ a narrow entrance slit, which restricts the intensity of the incident radiation. The FTIR method does not, since the throughput is determined by the diameter of the collimated beam. The increased light intensity available is known as Jacquinot's advantage [Jacquinot, 1960]. This is especially important in the IR range of the spectrum, since most detectors are not very sensitive.

IR spectra were taken using a Bomen DA8 vacuum Fourier transform infrared spectrometer (FTIR). This versatile spectrometer has many interchangeable parts, such as several detector modules and optical ports. The light source consists of a silicon carbide rod, called a globar, which is heated to 1200^{o}C. It emits blackbody radiation from $\sim$ 200 to 4000 cm^{-1}. The beamsplitter is made out of potassium bromide (KBr), which splits IR light well in the range of 450 to 5000 cm^{-1}. KBr is hygroscopic, so must be kept under vacuum to prevent degradation from the absorption of water. In fact, all the optics are kept under a vacuum system to prevent unwanted absorption from H_2O and CO_2. Two different detectors were used to collect the IR light, a mercury cadmium telluride (MCT) detector and the indium antimonide (InSb) detector. Both detectors need to be cooled to liquid nitrogen temperatures to reduce thermally excited current. The MCT detector is sensitive to light in the range 450 to 5000 cm^{-1} while the InSb is more sensitive in the range 1800 to 7000 cm^{-1}. The shapes of the spectra from these two detectors are different due to the different sensitivity vs. wavelength profiles of the devices. However, it is easy to see changes in intensity, which correspond to changes in the free carrier absorption, or the appearance of a defect peak, with either detector.

Light from the source passes through an adjustable mechanical iris, called an aperture, before reaching the beamsplitter. An additional beam switching mirror is used to direct the IR light to different ports on the spectrometer. The back port of the FTIR is equipped with a Janis closed-cycle helium cryostat system, capable of reaching ~ 10 K, for low temperature measurements. The detectors are equipped with an ellipsoidal mirror to focus the collimated beam onto the detecting area. The spectrometer is connected to a computer and control and data acquisition are performed by BOMEM PCDA software.

The FTIR spectrometer uses a He-Ne laser as an internal calibration standard, and therefore does not require external calibration. This gives better wavelength accuracy and is referred to as Connes' advantage [Connes and Connes, 1966]. This is done by creating an interference pattern with the He-Ne laser and counting the fringes. There are approximately 31600 cycles of laser cosine waves per cm displacement of the scanning mirror, so high precision measurements of the optical path length difference, δ, can be made. The addition of multiple scans through the Fourier transform algorithm requires the use of a positional reference. A visible white light source is used to determine the zero-path-difference (ZDP). A well defined maximum in intensity is seen at the ZDP, so each scan of the mirror can be aligned and averaged before taking the Fourier transform. Both the He-Ne and the white light source pass through the same optical path and beam splitter as the IR radiation from the globar. A beam splitter for the white light source is actually mounted on the center of the KBr IR beam splitter.

Typically a 405 nm high brightness LED was used for light exposure, commercially available from Radio Shack. A nominal voltage of 3.3 V was used at room temperature. This light source was set up inside the sample compartment of the FTIR so we did not have to break vacuum when a chip was exposed to light. The LED was also attached to the sample holder rod in the closed-cycle helium cryostat for low temperature measurements. Higher voltages were used at lower temperatures, to maintain the same approximate current of 20 mA across the LED. For example, a voltage of 3.8 V is needed at 175-180 K, while 5.0 V is needed around 95 K. A sample window allowed visual inspection of the light source, so it could be verified that the LED was on and shining with approximately the same brightness and color. Occasionally, other light sources were used, such as LEDs of other wavelengths, or a 405 nm laser diode shining through the sample window, and are indicated as such.

2.2 Ultraviolet and Visible (UV Vis) Spectroscopy

Ultraviolet and visible spectroscopy involves looking at photons in the visible and ultraviolet range of the spectrum. In this region of the spectrum, molecules undergo electronic transitions. This technique is complimentary to fluorescence spectroscopy, since fluorescence deals with transitions from the excited state to the ground state, while absorption measures transitions from the ground state to the excited state. Radiation is absorbed by the sample at specific frequencies, which correspond to the difference in energy between the two quantum states of the molecule. In solid state semiconductors, this corresponds to the energy difference between the valence and conduction bands, or a defect level to the conduction band.

In this region of the spectrum the most common type of spectrometer is a double-beam spectrophotometer that splits the light into two beams, one containing the sample, and one as a reference [Hollas, 2004]. The detector receives radiation alternately from the sample and reference beams, and a phase-sensitve treatment of the signal allows the two to be separated. The light source is a broad band source that emits over a wide wavelength range and a dispersing element is used to split the radiation into its component wavelengths.

UV Vis spectra in the wavelength range of 350 nm to 800 nm were all obtained on a Perkin Elmer Lambda 900 Series UV/VIS/NIR Spectrometer. See Figure 3 for the schematic diagram of this instrument. It is a double-beam spectrophotometer, with a double monochromator ratio recording system that uses both tungsten-halogen (NIR) and deuterium lamp sources (UV-Vis) [PerkinElmer Instruments, 2001]. This instrument is capable of measuring transmission, reflectance and absorption in solid or liquid state materials over the wavelength range of 185 nm to 2500 nm. It has an accuracy of 0.08 nm in the UV Vis range and 0.3 nm in the NIR range. It uses holographic gratings for dispersing the light into a spectrum with 1440 lines/mm in the UV Vis and 360 lines/mm in the NIR. Two detectors are used to collect the radiation from the sample and reference arms: a photomultiplier is used for the UV-Vis range and a lead sulfide (PbS) detector is used for the NIR range. The Lambda 900 automatically changes the light source and detector as needed, as it scans from higher to lower wavelength. Most scans were taken with a 1 nm resolution and a 1 sec/nm integration time.

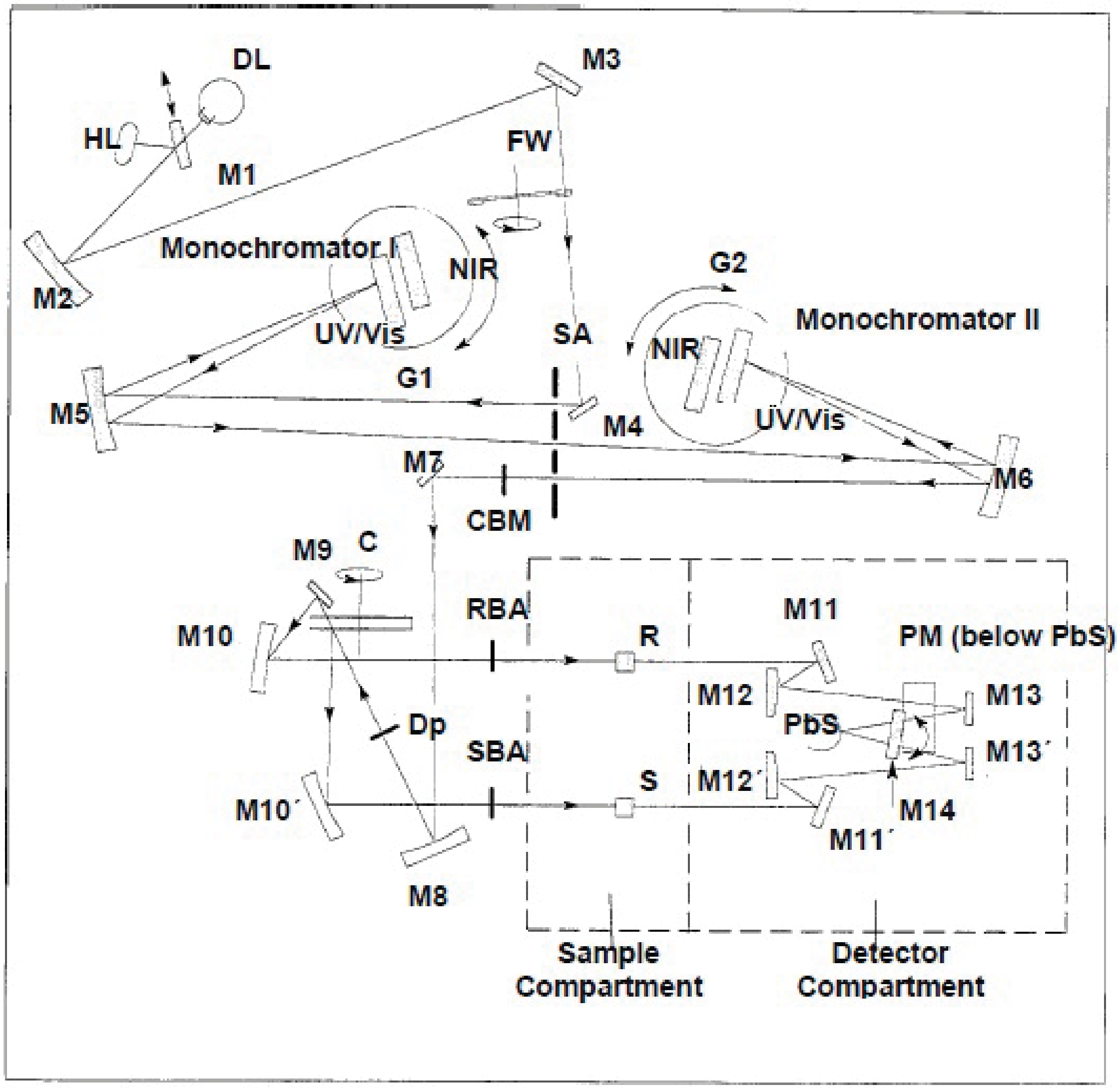

Figure 3: Schematic diagram of the UV Vis spectrometer optics [PerkinElmer Instruments, 2001].

2.3 Hall Effect

The Hall effect uses an applied magnetic field perpendicular to the flow of electrical current in a sample to measure the potential difference (Hall voltage). Hall effect is a great way to measure the electrical properties of a semiconductor, since it can measure carrier type, concentration and mobility. Other types of electrical measurements cannot separate all these quantities. The conductivity σ of a material is related to the concentration of free-carriers n and their mobility μ:

$$\sigma = ne\mu \tag{2.6}$$

where e is the charge of the electron. We can also write this in terms of electrical resistivity $\rho = 1/\sigma$, which is the inverse of the conductivity.

Hall effect measurements are based on the Lorenz force, where a charged particle q moves with velocity $\mathbf{v}$ in the presence of electric and magnetic fields:

$$\mathbf{F} = q(\mathbf{E} + \mathbf{v} \times \mathbf{B}) \tag{2.7}$$

If we have the magnetic field in the z direction and the current from the motion of charged particles in the x direction, the force due to the magnetic field pushes the charge carriers in the $-y$ direction causing them to move to one side of the sample (Figure 4). This results in an electric field, $\mathbf{E_H}$, pointing in the y direction. At equilibrium the Lorentz force becomes:

$$e(\mathbf{v} \times \mathbf{B}) = -e\mathbf{E_H} \tag{2.8}$$

The electric field is given by:

$$E_H = Bv_x \tag{2.9}$$

where v_x is the drift velocity along the x direction.

The Hall coefficient is defined as:

$$R_H = \frac{E_H}{j_x B} \tag{2.10}$$

where j_x is the x component of the current density. Substituting $j_x = nv_x e$ for the current density, Eq. 2.10 becomes:

$$R_H = \frac{1}{ne} \tag{2.11}$$

which expresses the Hall coefficient in terms of the carrier concentration, n.

Mobility is an important property of semiconductors. It characterizes how fast a charge carrier can move through the semiconductor under an applied electric field. Mobility is given by the magnitude of the drift velocity per unit electric field:

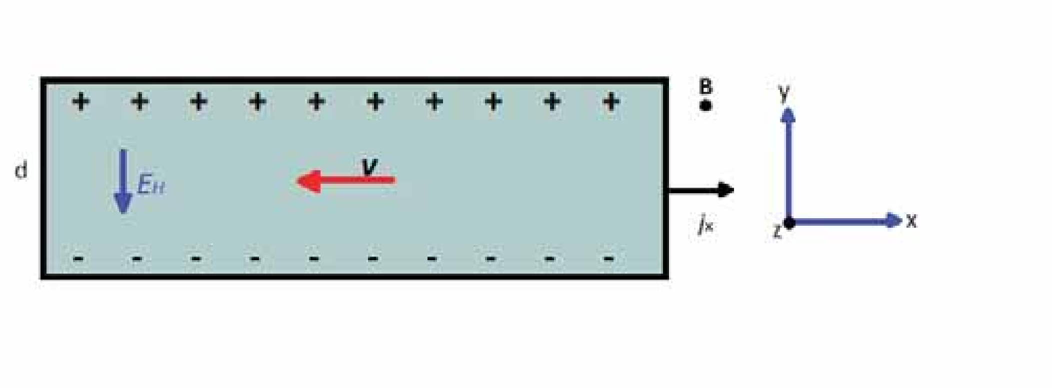

Figure 4: Hall effect configuration.

$$\mu = \frac{v_d}{E_x} \tag{2.12}$$

This quantity is conventionally expressed as a positive value for both holes and electrons, even though the drift velocities occur in opposite directions. Using the formula for the current density we can rewrite this as:

$$\mu = \frac{j_x}{neE_x} \tag{2.13}$$

Measurements of the Hall effect are usually conducted using a four probe method called the van der Pauw geometry [van der Pauw, 1958]. This method can be used on any arbitrarily shaped samples that are uniform and free of topographic holes. Four small ohmic contacts are placed on the periphery of a sample; ours had a square geometry (Figure 5). Inhomogeneities in the surface or contact placement inside the periphery can cause incorrect identification of carrier type [Bierwagen et al., 2008]. A current I_{12} goes into point 1 and out of 2 while the voltage V_{43} is measured between points 4 and 3. The sheet resistance is then given by:

$$R_{12,43} = \frac{V_{43}}{I_{12}} \tag{2.14}$$

Various iterations of this measurement can be performed. For instance if we chose to have the current going into point 3 and out of 2, and measure the potential difference between points 1 and 4, the resistance is:

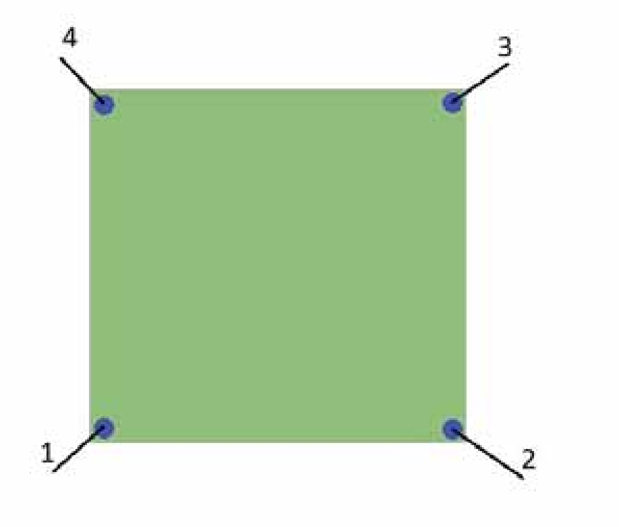

Figure 5: Sample contact geometry.

$$R_{32,41} = \frac{V_{41}}{I_{32}} \tag{2.15}$$

Van der Pauw [van der Pauw, 1958] showed, using conformal mapping, that for flat samples of arbitrary shape the resistivity ρ of the material is given by:

$$\exp(-\frac{\pi d}{\rho}R_{12,43}) + \exp(-\frac{\pi d}{\rho}R_{32,41}) = 1 \tag{2.16}$$

where d is the thickness of the sample. This can be rewritten as:

$$\rho = \frac{\pi d}{\ln(2)}\frac{R_{12,43} + R_{32,41}}{2} f(\frac{R_{12,43}}{R_{32,41}}) \tag{2.17}$$

The form factor f depends on the ratio of the sheet resistances $\frac{R_{12,43}}{R_{32,41}}$. Samples that are nearly circular or square shaped have $f \approx 1$. In these symmetric samples, the resistivity is given by:

$$\rho = \frac{\pi d}{\ln(2)} R \tag{2.18}$$

All Hall effect measurements were obtained using an MMR Technologies, Inc. variable temperature Hall measurement system using the van der Pauw technique. The system is equipped with a K-20 programmable temperature controller, an H-50 Hall-van der Pauw controller, and a

Hall dewar vacuum tight chamber. The sample is mounted onto a cold stage with a thermocouple and heating wire attached underneath. Low temperatures are achieved though a Joule-Thomson refrigerator. High pressure nitrogen gas is allowed to expand adiabatically through capillary channels in the cold stage, and successive pressure drops result in the overall temperature drop. The gas flow, and operation of the heating wire with the K-20, allow the desired temperature in the range from $\sim$ 80 K to 700 K to be selected. The H-20 controls and records the applied current and voltage between the probes for the measurement.

2.4 Seebeck Effect

The flow of heat is related to the flow of electric charge. Mobile charge carriers have higher average thermal energy when the temperature is greater. Imagine a bar of material that is in thermal equilibrium with two reservoirs, A and B. The temperature of side A is T_A and that of B is T_B, where $T_A > T_B$. Side A has more thermal energy, manifested in greater random motion of the charge carriers. We can also think of this in terms of the temperature dependence of the Fermi distribution of the valence electrons. At higher temperature, more valence electrons are present above the Fermi energy.

The mobile charge carriers will diffuse throughout the sample, and since the concentration of them is lower on the cold side (B) it is energetically favorable for them to move from the warmer end of the bar (A) to the colder end (B). The slow diffusion of the charge carriers results in the flow of current. This introduces a voltage difference across the sample, which can be measured. We can exploit this fact to determine the majority charge carrier type in a semiconductor [Harman and Honig, 1967]. If the end with the higher temperature has a negative voltage, the material is *p*-type, while for electrons the end with higher temperature has positive voltage. This was first discovered by Thomas Seebeck around 1821.

Seebeck effect measurements were made using the setup shown in Figure 6. Two copper blocks are attached to an electrically insulating and thermally conductive sapphire wafer on the bottom. This part of the setup can be placed on top of a hot plate, to raise the temperature of entire setup so highly resistive samples can be measured. (Resistance generally decreases with increasing temperatures.)

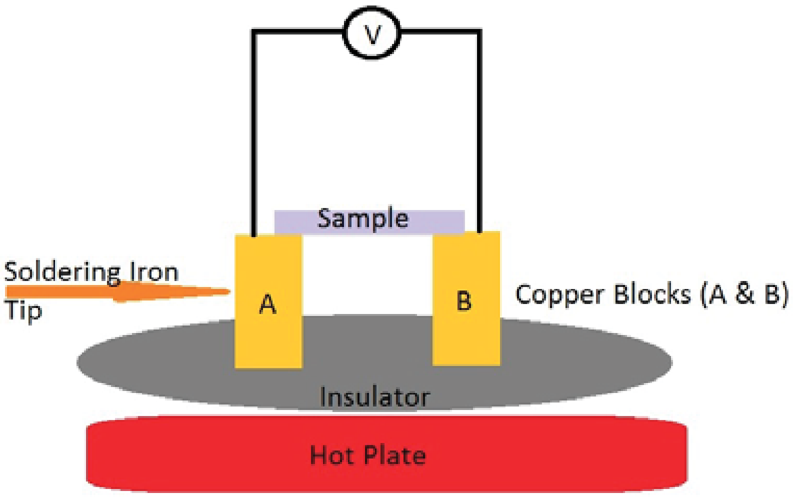

Figure 6: Schematic diagram showing experimental setup for Seebeck effect measurements.

The sample forms a bridge between the copper blocks, and is attached with contacts and silver paint. The temperature difference between the blocks is achieved by touching one copper block with the tip of a variable temperature soldering iron. On the top of the blocks are wires that run to a Keithley model 2400 source meter. The Keithley measures the voltage difference across the sample without pushing a current though it. The voltage will increase or decrease when heat is applied to one side. Our setup only measures the sign, which gives majority carrier type. The sign of the voltage change is measured when heating one side. Then the sample is allowed to cool back down and the other side is then heated.

2.5 Electron Paramagnetic Resonance (EPR) Spectroscopy

Magnetic resonance spectroscopy is a useful tool for characterizing electrically active defects in semiconductors. Microwaves in combination with a magnetic field allow us to detect unpaired electron spins via a technique called electron paramagnetic resonance (EPR) spectroscopy [McCluskey and Haller, 2012]. Only defects in a crystal that contain an unpaired spin are EPR active. For example, single donors have an unpaired spin in their neutral charge state, so they are EPR active, while when they are ionized, they do not and therefore have no EPR signal.

Quantum mechanics underlies the basic mechanism of EPR, with the Zeeman effect. Consider a single electron in an external magnetic field, B_0, that points in the z direction. The electron spin has a magnetic moment, with a z component given by

$$\mu_z = -g\mu_B m_s \tag{2.19}$$

where μ_B is the Bohr magneton (9.274 x 10^{-24} Joules/Tesla), $m_s = \pm\frac{1}{2}$, and g is the Landé g-factor (g =2.00232 for the free electron). The g-factor is a proportionality constant that depends on the electronic configuration of the radical or ion, but is usually close to 2. The energy of the magnetic moment in the magnetic field **B** can be written as:

$$E_e = -\mu \cdot \mathbf{B} = g\mu_b B m_s \tag{2.20}$$

The magnetic field lifts the spin degeneracy, causing the spin-up state to be higher in energy than the spin-down state. This interaction between the electronic spin and the magnetic field is called Zeeman splitting and the energy difference is given by:

$$\triangle E = g\mu_B B = h\nu \tag{2.21}$$

A photon of energy $\triangle E$ can promote an electron from the spin-down state to the spin-up state.

Equations 2.19 and 2.21 show that the spin states have the same energy in the absence of the magnetic field, and the energy difference between the spin states depends linearly on the magnetic field. This allows us to keep the microwave frequency fixed and vary the magnetic field. Due to the limitations of microwave electronics this is much easier to do experimentally. A peak in the absorption will occur when the magnetic field 'tunes' the two spin states so that their energy difference matches the energy of the radiation. The integrated intensity of the EPR signal is proportional to the concentration of the defect [Weber et al., 1998].

This is not a complete picture. Hyperfine interactions between the electron and the nucleus of the atom can add additional structure to the EPR lines, which can give useful information about the chemical identity of the defect. Additionally g is actually a tensor which corresponds to the point group symmetry of the defect, and can show different resonances when the magnetic field is applied along various crystallographic axes.

A typical EPR apparatus has a microwave bridge (metal box to amplify weak signals) that

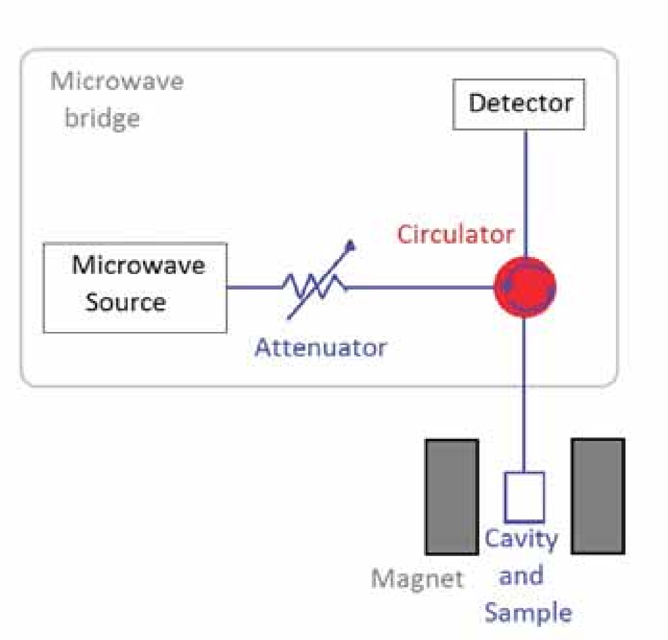

Figure 7: EPR schematic diagram. The circulator delivers microwaves to the sample and directs the reflected microwaves to the detector.

contains the source and detector (Figure 7). The intensity of the microwaves is controlled with an attenuator. The microwaves then travel into the circulator which directs the microwaves into the cavity that is placed between the poles of an electromagnet. The current is modulated at low frequencies in the electromagnet to slowly vary the magnetic field. An empty cavity has a high quality factor Q and reflected microwave power is low. A sample placed in the cavity will absorb microwaves, resulting in a loss in Q, causing the microwaves to be reflected back. The reflected microwaves enter back into the circulator where they are directed to the detector, which is a Schottky diode. This converts microwave power into an electrical current. A lock-in detector will produce an output that is proportional to the corresponding modulation in the EPR signal.

All our EPR measurements were conducted by Mary Ellen Zvanut and J. Dashdorj at the University of Alabama at Birmingham. They have a Bruker Model EMX 9.6 GHz EPR Spectrometer.

Chapter THREE

PERSISTENT PHOTOCONDUCTIVITY (PPC)

Photoconductivity (PC) is the phenomenon where the absorption of electromagnetic radiation by a material leads to the material becoming more electrically conductive. For semiconductors this means that the number of free electrons or holes is increased with light exposure. This can happen in a variety of ways, two of which are: (1) the incident light has enough energy to excite the electrons across the band gap or (2) electrons are promoted from defect levels to the conduction band. This effect will often decay on the order of seconds to minutes after the light is turned off. Persistent photoconductivity (PPC) means the effect is stable over large time scales. Point defects such as DX centers can lead to PPC below room temperature [Lang and Logan, 1977]. Room temperature PPC has been observed in wide bandgap semiconductors before, such as GaN [Hirsch et al., 1997] and GaInNAs [Li et al., 1999], but the increase in conductivity is less than an order of magnitude. STO's increase in conductivity is much larger, at several orders of magnitude, and occurs at room temperature.

The recipe Tarun et al. [Tarun et al., 2013] used for inducing the PPC effect involved sealing a bulk single crystal chip of STO in a fused silica ampoule along with 0.5 grams of strontium oxide (SrO) powder under rough vacuum (∼50-100 mTorr). Then the chip was annealed in a three-zone horizontal tube furnace at 1200°C for 1 hour. After the heat treatment, the ampoule was allowed to cool in the ambient air. It takes approximately ten minutes to reach room temperature, so cooling is relatively rapid.

3.1 FTIR changes with PPC

The change in conductivity can be observed directly by Hall effect measurements, but that is not the only way. By correlating electrical and spectral measurements, Baer [Baer, 1966] was able to show that an increase or decrease in the optical absorption in the IR part of the spectrum corresponds to a change in the free carrier absorption of STO.

In PPC samples an increase in free carrier absorption corresponds to a drop of the transmitted

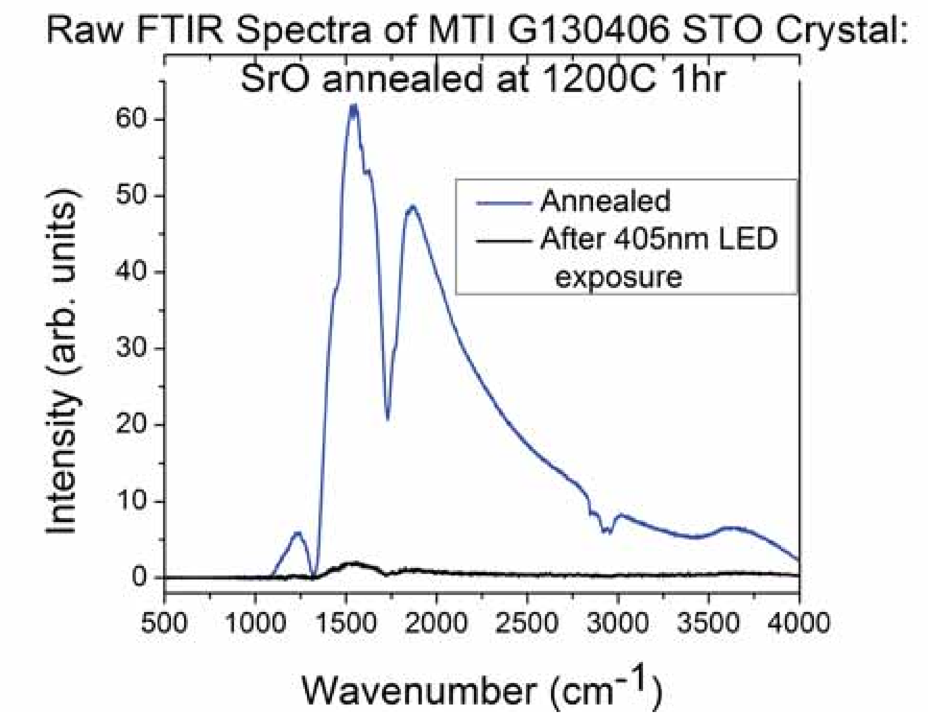

Figure 8: Typical FTIR spectra with MCT detector of SrO annealed STO. Note the large drop in magnitude after light exposure with a 405 nm LED, indicative of PPC.

IR intensity to nearly zero, as illustrated in Figure 8. Contrast this with samples without PPC, as shown in Figure 9 and Figure 10. Samples without PPC either display a small change in absorbance with light exposure or none at all. The small change in absorbance may be due to increased free carriers, but we are interested in the dramatic orders of magnitude change that STO usually displays with PPC. Other spectral indicators are also present that can clarify the results for the case of moderate intensity changes.

Details of the line shape seen in the FTIR spectra are discussed in Appendix C: Free Carrier Line Shape in STO.

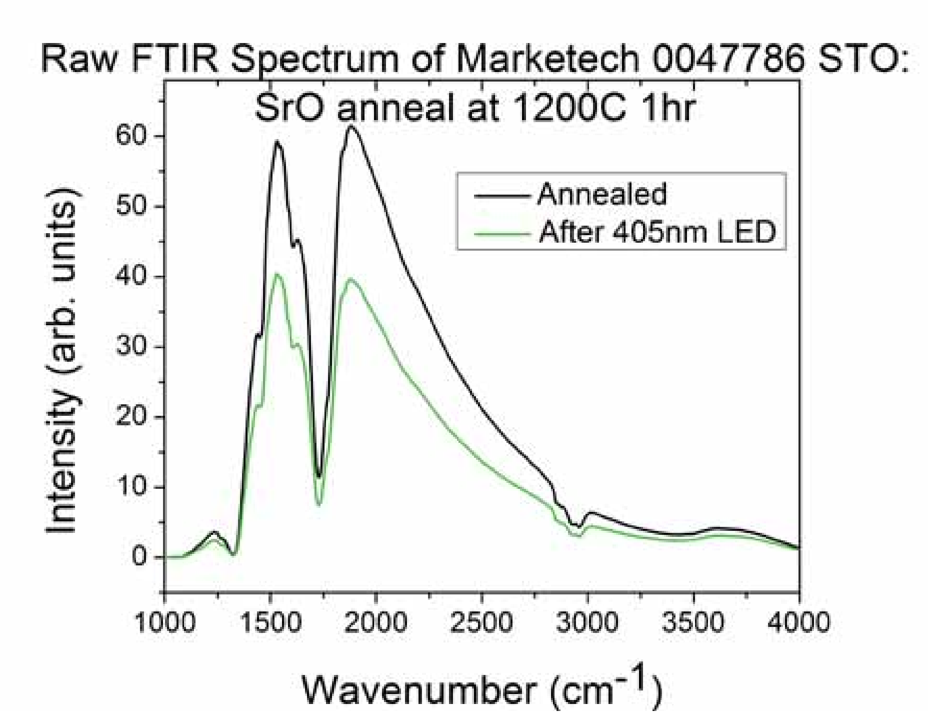

Figure 9: FTIR spectra with MCT detector of STO sample that does not display PPC even though there is a small change with light exposure.

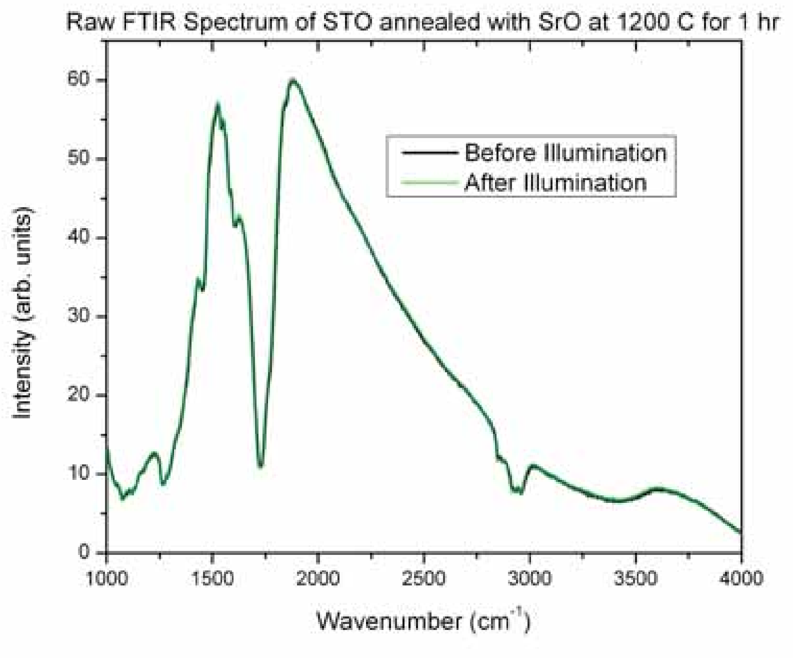

Figure 10: Mateck 14032715 STO. FTIR spectra with MCT detector on a sample without PPC. Notice there is no change in absorbance with light exposure.

3.2 UV Vis changes with PPC

The near ultraviolet (UV) and visible (Vis) regions of the spectrum show distinctive changes when a sample has PPC. While there can be significant differences between samples, especially with different treatments, all annealed STO samples that displayed PPC had a peak around 520 nm that only appeared after light exposure. The intensity of this peak after light exposure varies greatly for different batches, and its strength does not correlate with the observed changes in conductivity or increase in free carrier absorption. The peak at 520 nm can be present for other reasons, so only the appearance after light exposure is indicative of PPC. For example, vacuum annealing will also produce this peak, but it does not change much with light exposure (Figure 11).

The peak at 520 nm (2.4 eV) has not been positively identified. It is present in Nb doped samples and is found in thermally activated samples (pure, Nb, Fe, and Ni doped) [Wild et al., 1973]. Crystals doped with Fe, Co and Ni have this peak present after reduction at high temperatures [Blazey and Weibel, 1984]. Additionally, this peak has been observed in a variety of as-grown crystals (transparent, yellow and blue) as well as those doped with Mn, Co, Ni, Sm and Nd [Kulagin and Hieckmann, 2012]. However, the location and size (after activation) of this peak is independent of the doping, and does not increase appreciably above background as the activation of free carriers is increased, so it must be related to a common impurity or an electronic transition of an atom in the crystal lattice [Wild et al., 1973].

Chromium is a common impurity in all samples at the ppm level and has a crystal field transition at 2.2 eV, which suggests it might be related to the 520 nm peak. However, the oscillator strength of the peak was too high compared to the measured chromium impurity concentration [Wild et al., 1973]. Other explanations have been proposed, such as an interband transition from one conduction band to another of the titanium atom orbitals [Yamada and Miller, 1973]. Another possibility involves oxygen vacancies, which could form a narrow impurity type band, or several overlapping closely spaced levels in the band gap about 0.8 eV from the valence band [Wild et al., 1973]. This peak could be due to the excitation of an electron trapped in an oxygen vacancy [Baer, 1966].

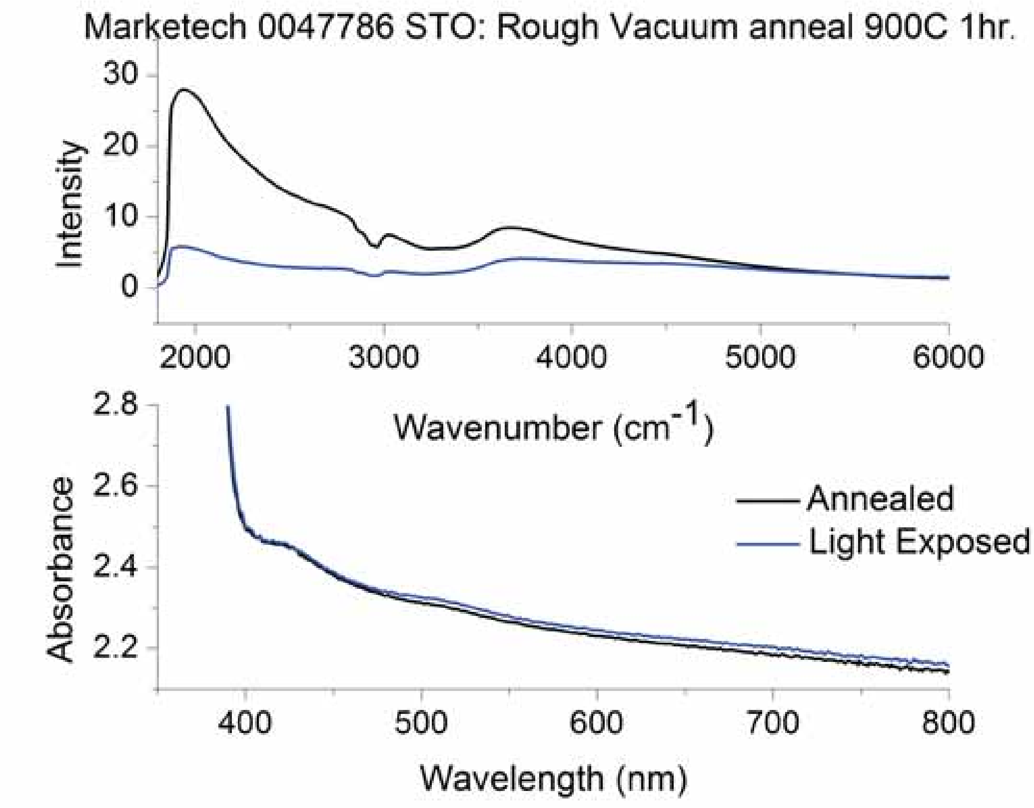

Figure 11: (top) FTIR spectra with InSb detector. This vacuum annealed sample has a change in absorbance with light, but much less so than samples that have PPC (compare with Figure 12). (bottom) UV Vis spectra that do not change significantly with light exposure.

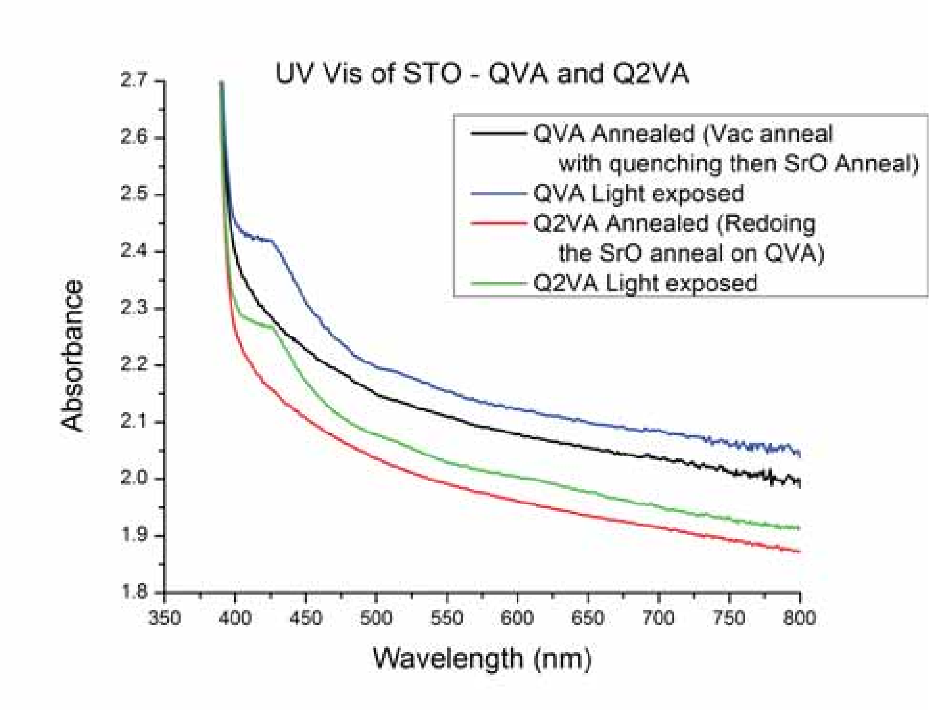

Figure 12: Spectra showing both peaks appearing after light exposure. Redoing the SrO anneal results in the same behavior. This batch G150101 from MTI has a very small PPC peak, yet it still has the same order-of-magnitude increase in conductivity.

Another peak is also present in light exposed PPC samples, at 430 nm, but its behavior after annealing and before light exposure varies. Sometimes the peak at 430 nm is present before light exposure. Other times it appears only after light exposure, like the peak at 520 nm. See Figure 13 and Figure 14 for examples of these two cases. This is not due to differences in the impurity concentrations of the two samples. If the peak at 430 nm is already present, redoing the SrO anneal on a chip results in the same behavior of the peaks (Figure 12). However, if we re-anneal a chip that did not have the 430 nm peak present before light exposure, but cool the chip faster this time, the 430 nm peak is now present before light exposure. The first anneal gave Figure 13, while redoing the annealing process, but cooling the chip faster, resulted in Figure 14. Faster cooling locks in more oxygen vacancies and vacancy complexes which will affect the charge states of the impurities within the lattice (see Section 4.1). The details of this charge transfer process are explained in Section 4.4 when we discuss iron. This suggests that the presence of the peak at 430 nm is related to the charge state of impurities within the crystal.

In the literature, the peak around 430 nm (2.9 eV) has been found using EPR techniques as an

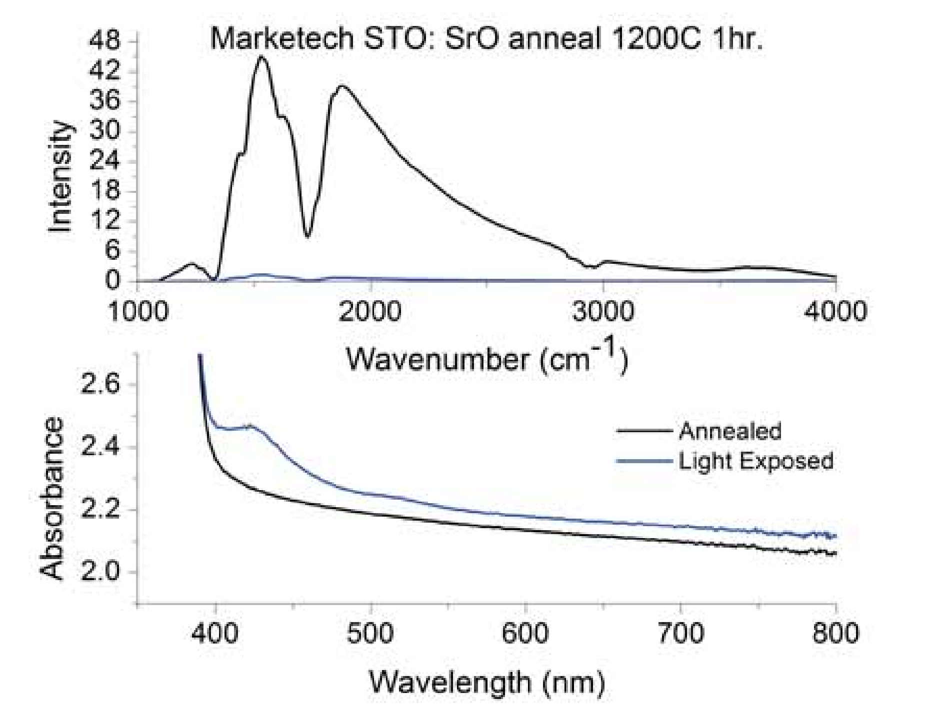

Figure 13: Example spectra where both the 430 nm and 520 nm peaks appear after light exposure. Note: FTIR spectra with MCT detector on top and UV Vis on the bottom.

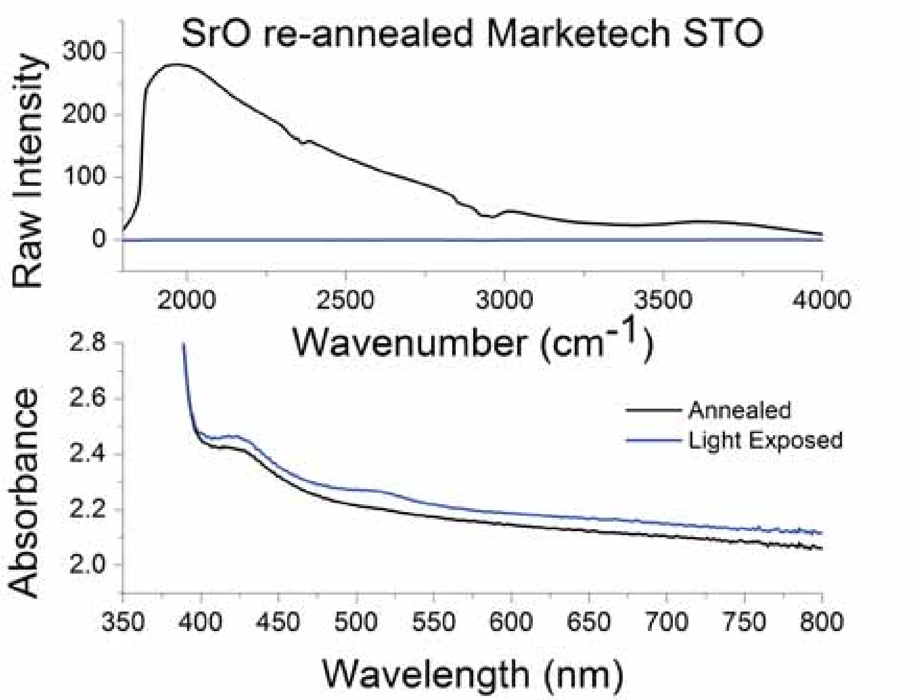

Figure 14: Example spectra showing only the 520 nm peak appearing after light exposure. Note: FTIR spectra with InSb detector on top and UV Vis on the bottom.

absorption by an Fe^{4+} ion in a cubic site in photochromic studies [Faughnan, 1971]. Crystals doped with Cr, Mn, Fe and Co reduced above 1200°C show this absorption band, while it disappears with reduction temperatures of 800°C in Ni doped samples [Blazey and Weibel, 1984].

Both the peaks at 430 and 520 nm are thermally activated and can be destroyed by slow cooling [Wild et al., 1973]. These peaks also appear in photochromic studies, where light irradiation introduces a temporary reversible color change of the material with transition metal doping [Faughnan, 1971]. Transient changes of conductivity accompany the coloring and bleaching of photochromic Fe and Mo doped STO [Williams, 1971]. The changes in coloration and electrical responses for PPC samples are stable at room temperature, unlike the photochromic response, which is stable around 200 K [Wild et al., 1973, Faughnan and Kiss, 1968]. The 520 nm peak will anneal away around 200°C, while the 430 nm peak will anneal way at approximately 300°C, changing the conductivity of the sample dramatically [Lebedeva et al., 1988]. Reduction will remove these light induced bands in Fe doped STO as well as Fe and Mo co-doped STO [Faughnan and Kiss, 1968].

3.3 Light Exposure and the Onset of PPC

As demonstrated earlier, when a chip is exposed to light, several phenomena are observed: a large decrease in the resistance of the sample, the appearance of two peaks in the UV Vis spectrum, and a large increase in the free-carrier absorption. We studied the dynamics of the latter two, by repeatedly taking spectra of the same sample after an incremental amount of light exposure. Resistance measurements require the placement of contacts on the sample, which will block light exposure in the contact region.

At room temperature, PPC occurs quite rapidly with exposure to light (Figure 15). A FTIR spectrum of an annealed sample was taken. Then, the sample was exposed to an LED for 1 minute and another spectrum was obtained. The LED had a wavelength of 405 nm, was approximately 2 inches from the sample, and was operating with a current of 0.01 Amps. Again the sample was exposed to 1 minute of light and another spectrum was obtained. This process was repeated until no further change was observed, which took ~ 6 minutes. The most dramatic change in the intensity occurs during the first minute of exposure.

Another sample (Figure 16) was also exposed at room temperature in a similar incremental

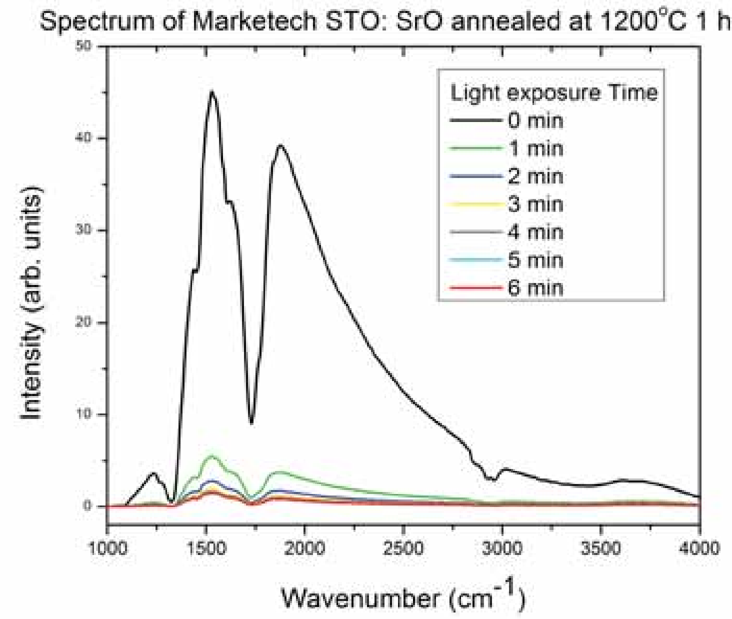

Figure 15: Room temperature FTIR spectra showing intensity change per minute of light exposure.

manner, but with smaller increments, though the time required to expose the sample is shorter. The reason this sample has a shorter exposure time is because a larger current of 0.02 amps was used to power the LED, resulting in higher irradiance of the light source.

This same sample was then "erased" on a hot plate for 20 minutes at 300°C. As shown in Chapter 5, this essentially returns the chip to its pre-light exposure state. The chip was then re-exposed in the UV Vis sample compartment, so we could see the evolution of the 430 and 520 nm peaks (Figure 17). To within experimental uncertainty both peaks appear at roughly the same rate. This is because light photoionizes Fe^{3+} and the PPC defect.

While the current powering the LED was kept the same in the IR and UV Vis experiments, the spacing and orientation of the light source from the sample was not exactly the same. This means the sample exposed at slightly different rates and are not directly comparable. However, we can still see the general trend and correlation that happens over time. It takes a few seconds for the light exposure to start generating free carriers. Light photoionizes Fe^{3+} and the PPC defect. This results in Fe^{3+} giving up an electron to the conduction band and becoming Fe^{4+}. A similar change is expected to occur with the PPC defect, resulting in electrons being promoted from the PPC defect level to the conduction band.

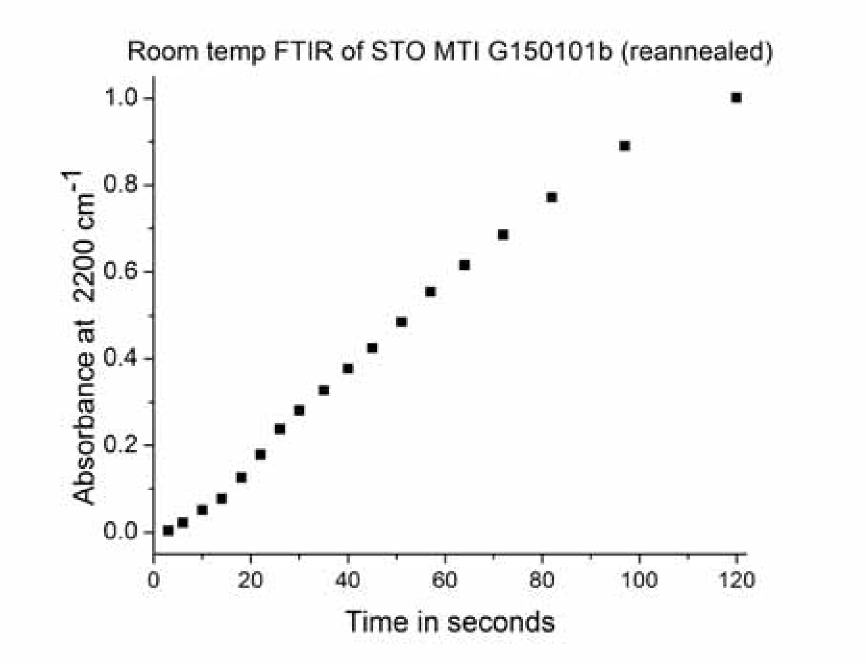

Figure 16: Room temperature FTIR showing how the absorbance at 2200 cm^{-1} changes per second of light exposure.

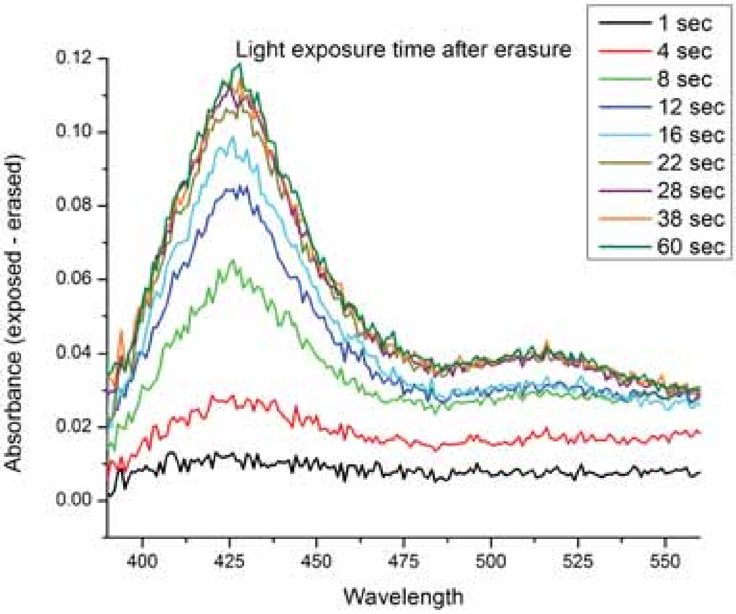

Figure 17: UV Vis spectra showing how the peaks changes per second of light exposure. The spectrum of the erased sample was subtracted from each to show the peaks more clearly. Notice that the 430 nm and 520 nm peaks grow together.

3.4 Effect of Temperature on Exposure

Temperature can dramatically affect the properties of materials, including their structural phase, carrier concentration, brittleness, or reaction rates. Studying how temperature affects the ability of light to induce PPC in a sample could yield useful information about the mechanisms behind this phenomenon. At low temperatures, such as 180 K, the change in IR intensity when exposed to a 405 nm LED inside the cryostat occurs more slowly than at room temperature (Figure 18).

The reason for the difference in time needed to expose a chip is complicated by the fact that the behavior of LEDs at low temperatures is only partially characterized. An LED is a semiconductor diode that emits light when current flows across the $p-n$ junction. During normal operation, an LED requires a direct current power supply, to provide the necessary positive bias or forward voltage across the junction. Most commercial LEDs have a recommended range of operating temperatures, where the low end is usually around -20°C. At temperatures lower than this, the LED will be very dim or fail to turn on at all if the usual forward voltage is still employed. In LEDs, like most semiconductor devices, the band gap increases as the temperature drops [Long, 1968]. This effect becomes significant below -20°C.

Since the LEDs are current driven, if care is taken to maintain the same operating current, rather than voltage, an LED can function at low temperatures of 95 K or possibly lower. A test was performed to measure how the voltage needed to maintain the constant current of 0.02 A across the 405 nm high intensity LED changes with temperature (Figure 19). A constant current power supply was used to drive the LED inside the cryostat on the back side of the FTIR as the system cooled down, and voltage and temperature were recorded. A window allowed visual inspection of the LED during the experiment, so it could be verified that the LED was shining with roughly the same color and intensity. The increase in voltage as the temperature changes is linear, to within the error of the measurement. The central wavelength of an LED shifts to shorter wavelengths when the temperature decreases, due to the temperature dependence of the band gap [Long, 1968]. This decrease in wavelength is on the order of 10-20 nm for temperatures around 100 K [Khanna, 2014].

The uncertainties in LED performance can be bypassed by using a light source outside the

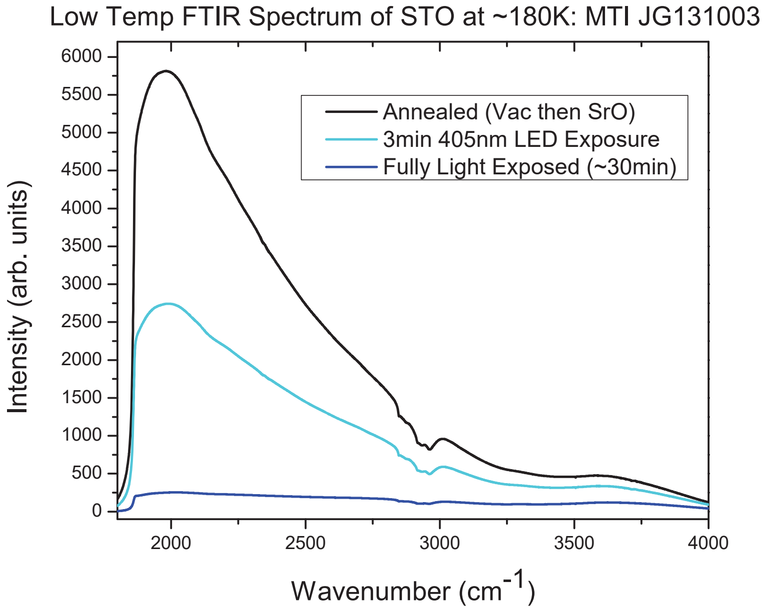

Figure 18: Exposure to light takes longer at low temperatures, with a 405 nm LED.

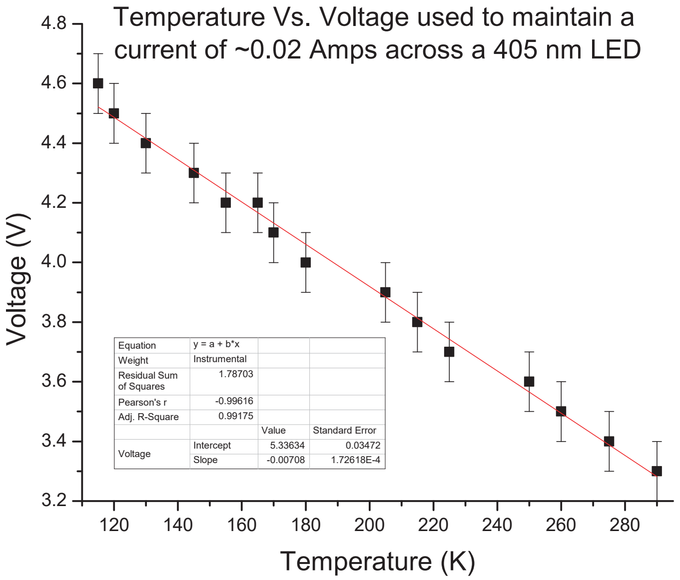

Equation	y = a + b*x		
Weight	Instrumental		
Residual Sum of Squares	1.78703		
Pearson's r	-0.99616		
Adj. R-Square	0.99175		
		Value	Standard Error
Voltage	Intercept	5.33634	0.03472
	Slope	-0.00708	1.72618E-4

Figure 19: Plot of the voltage needed to maintain a constant current through the LED versus temperature. The red line is a linear fit.

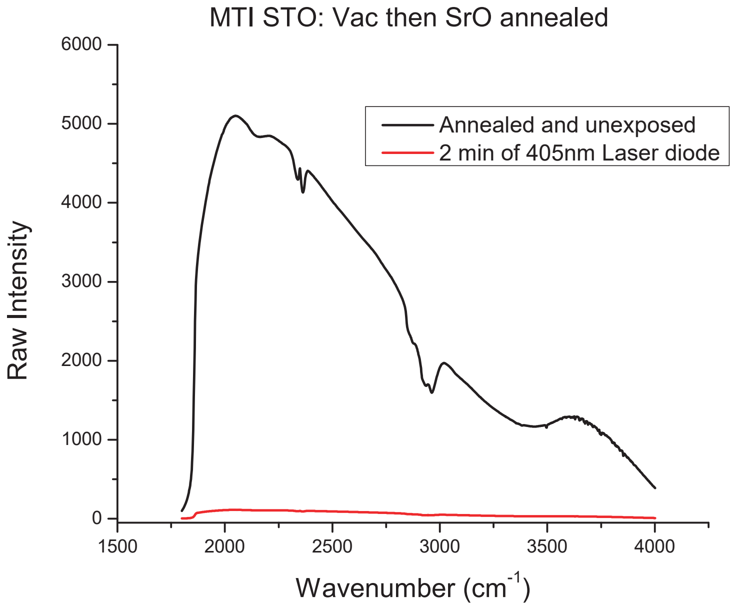

Figure 20: Room temperature FTIR spectra. A 405 nm laser diode will expose a sample at room temperature completely in under 2 minutes.

cryostat and shining it through the window on the FTIR. A 405 nm laser diode was chosen to ensure the source was bright enough to easily shine through the many layers of glass in the windows into the cryostat, and had a very narrow light emission profile. FTIR spectra show that the laser diode will fully expose a sample in under 2 minutes at room temperature (Figure 20). Low temperature is a different story. Figures 21 and 23 show that a 405 nm laser diode will not induce PPC at temperatures of 160 K and below. The UV Vis spectra of Figure 21 can be seen in Figure 22. This chip did display PPC, however, the laser diode was unable to activate it at low temperatures. Using a 405 nm LED placed inside the cryostat, PPC can be activated at temperatures as low as 115 K (Figure 24).

An LED has a wider intensity vs. wavelength profile than a laser diode, and the wavelength of the LED shifts to shorter wavelengths as it cools in the cryostat. Like most semiconductors, the band gap of STO widens as the temperature is reduced, from 3.20 eV at 300 K to 3.23 eV at 100 K for the indirect gap [Trepakov et al., 2009]. However, this change of 0.03 eV corresponds to a very small change in the wavelength of light, about 5 nm. At room temperature, the threshold for activation of PPC is around 2.9 eV or 428 nm [Tarun et al., 2013]. This implies that the defect

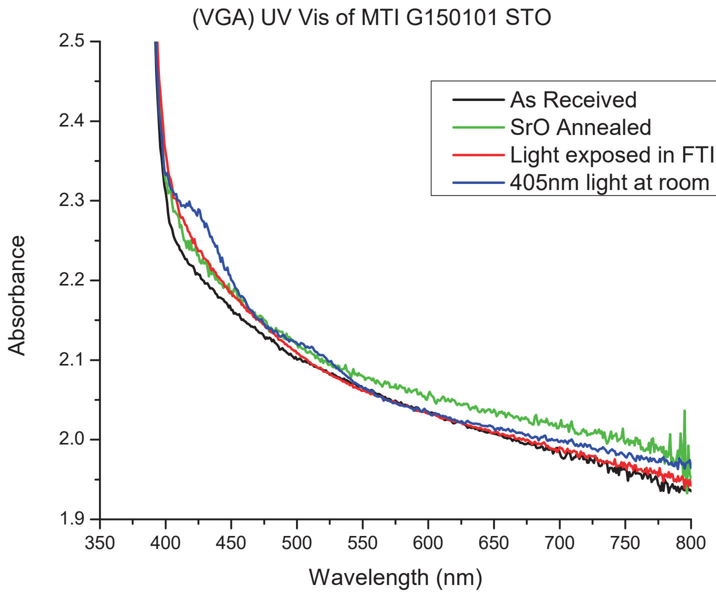

Figure 21: Low temperature FTIR spectra showing that a 405 nm laser diode is insufficient to induce PPC in a sample when the sample is below 140 K. The UV Vis spectra are shown in Figure 22.

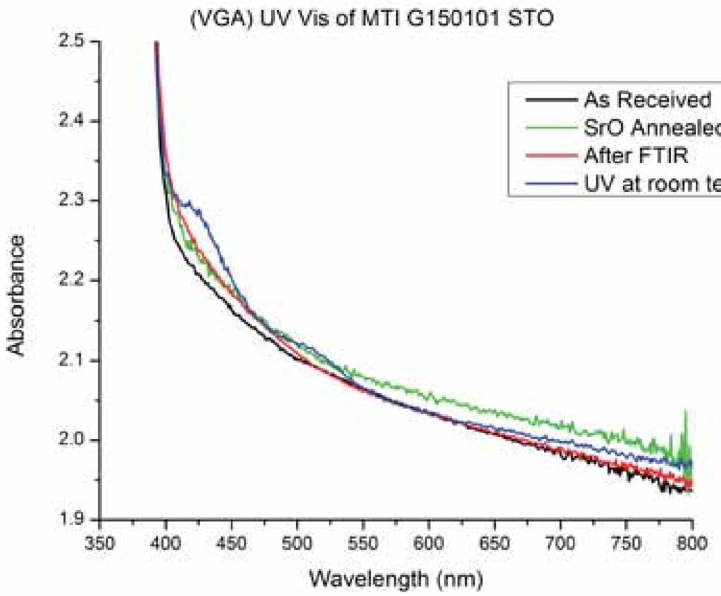

Figure 22: UV Vis spectra of the sample shown in Figure 21. The laser diode was unable to expose the chip while in the cryostat of the FTIR. Later exposure to a 405 nm LED at room temperature induced PPC.

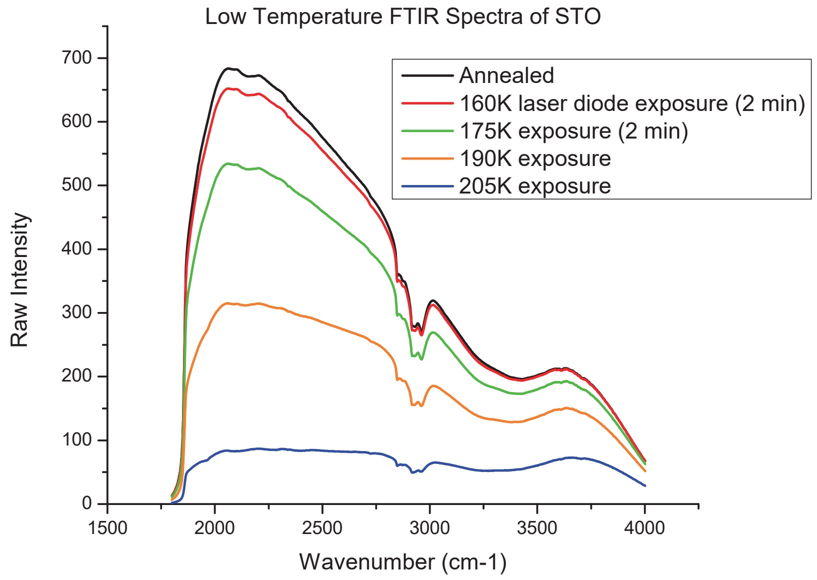

Figure 23: Low temperature FTIR spectra showing how sample temperature affects exposure time, when the light source is a 405 nm laser diode. The chip was exposed for 2 minutes at each temperature.

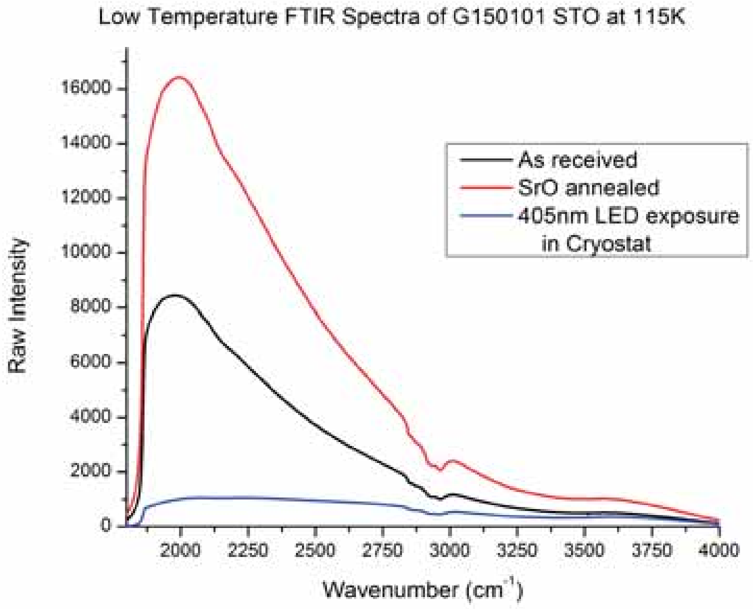

Figure 24: Low temperature FTIR spectra, showing I was successfully able to expose a chip at 115 K with an LED inside the cryostat.

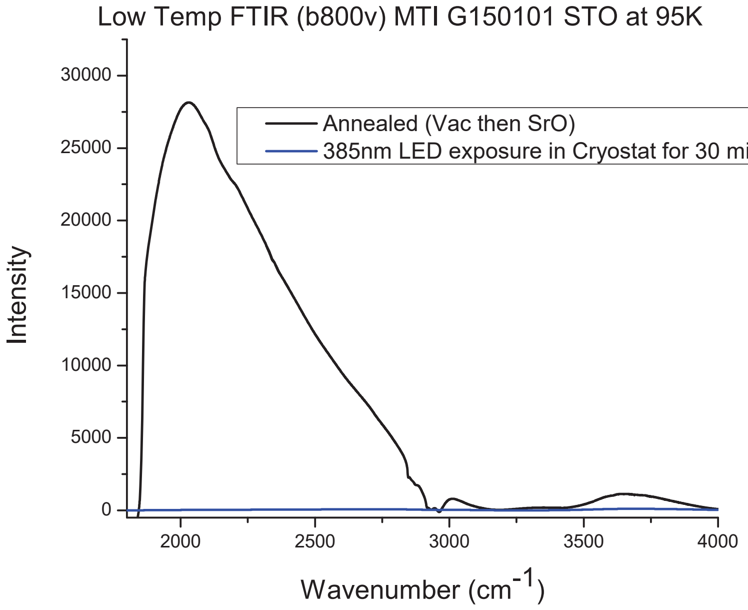

Figure 25: Low temperature FTIR spectra showing that a 385 nm LED will expose a chip below the phase transition temperature. A 405 nm LED will not.

involved in PPC does not shift with the band gap as the temperature is reduced or that the energy required for the onset of PPC sharpens as temperature decreases [Alkauskas et al., 2016]. It is also worth noting that a 385 nm LED will expose a chip below the phase transition temperature, ∼ 105 K, while a 405 nm LED will not (Figure 25). This tells us that the photon energy needed to induce PPC increases as the temperature decreases, and the structural changes that occur below the phase transition temperature do not interfere with PPC.

In conclusion, the energy required for PPC onset increases as the temperature is decreased. This could be due to the sharpening of the onset. Optical absorption from a single acceptor is described by $A^{-}+h\nu \rightarrow A^{\mathrm{o}}+e^{-}$, where e^{-} is the electron in the conduction band. As temperatures increase, higher vibrational modes in the electronic ground state are thermally excited. This smears out the transition induced by a photon of light from the ground state to the excited state (Figure 26).

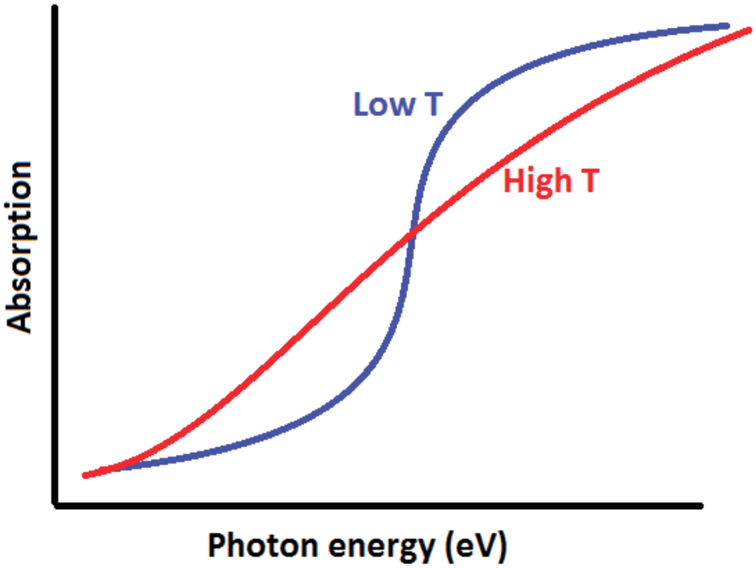

Figure 26: Onset of absorption vs energy for low and high temperatures.

Chapter FOUR

POINT DEFECTS

The properties of semiconductors are largely determined by their defects. Even nominally pure samples contain ppm levels of common impurities such as iron and chromium. Annealing is a process of heat treatment where defects diffuse through the crystal lattice. There are many types of defects possible, but we will focus on point defects, which are imperfections at a single point within the lattice, as opposed to extended defects. Defects often introduce energy levels within the band gap. Figure 27 shows the position of some of the important defects in STO we will discuss in the following sections.

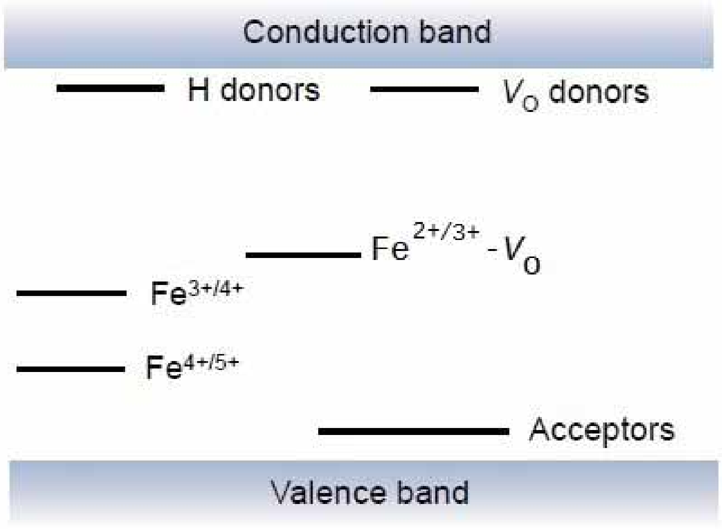

Figure 27: Schematic energy-level diagram of defects in STO [Poole et al., 2015a].

4.1 Role of Oxygen Vacancies

Oxygen vacancies have long been thought to be the dominant factor controlling the conductivity. They introduce energy levels in the band gap near the conduction band (Figure 27). However, there is some controversy in the literature, as some studies have suggested that they are deep, rather than shallow, donors [King and Veal, 2011]. Oxygen vacancies are the most mobile defects in pure STO, with the possible exception of hydrogen [Stocker et al., 2010], and are highly mobile above 850°C [Wild et al., 1973]. In as-grown crystals, oxygen vacancies are brought into the lattice to compensate the positive charge deficiency on 3+ ions, forming oxygen vacancy complexes, such as Fe^{3+} - V_O [Morin and Oliver, 1973]. This complicates the role of oxygen, since the iron-oxygen vacancy complexes have there own set of energy levels within the band gap. When STO is stoichiometric, the compound is an insulator, while the oxygen reduced phase ($SrTiO_{3-x}$) is metallic [Gevorgian, 2009]. Oxygen vacancies might act as electron donors with a low ionization energy, so a large concentration will make the crystals highly conducting [Blazey and Weibel, 1984].

Oxygen vacancies and complexes thereof are introduced into pure STO by a high temperature reduction followed by rapid cooling [Blazey and Weibel, 1984, Yamada and Miller, 1973]. Slowly cooling the sample in the oven back to room temperature, even for reduction anneals, causes the sample to return to its nearly clear insulating state [Wild et al., 1973]. Reduction and oxidation can take place at temperatures as low as 400°C, indicating a high diffusion mobility for oxygen vacancies [Faughnan, 1971]. Electrocoloration studies have shown that oxygen vacancy-ion complexes make a significant contribution to conductivity above 400 K [Morin and Oliver, 1973]. At least for Fe doped single crystal STO, the defects are partially frozen in for temperatures below approximately 750 K [Denk et al., 1995].

High temperature measurements of the self-diffusion coefficient of oxygen ions indicate that it is independent of the oxygen partial pressure [Morin and Oliver, 1973]. This means the electrical conductivity depends on the oxygen partial pressure during reduction treatment [Stocker et al., 2010, Yamada and Miller, 1973]. Heating changes the relative amounts of donors and acceptors and hence the Fermi level [Stocker et al., 2010] but will not eliminate these vacancies from the lattice [Morin and Oliver, 1973]. Strontium vacancies often have a similar concentration as oxygen vacancies, and they compensate each other [Moos and Hardtl, 1997]. Additionally, there is some evidence to indicate that the presence of oxygen vacancies can dramatically change the energy level scheme of transition metal ions, and selectively enhance the intensity of certain transitions [Dischler and Räuber, 1975]. However, hydrogen can act as a catalyst for the production of oxygen vacancies, so the problems of hydrogen and oxygen cannot be cleanly separated [Scott et al., 2001].

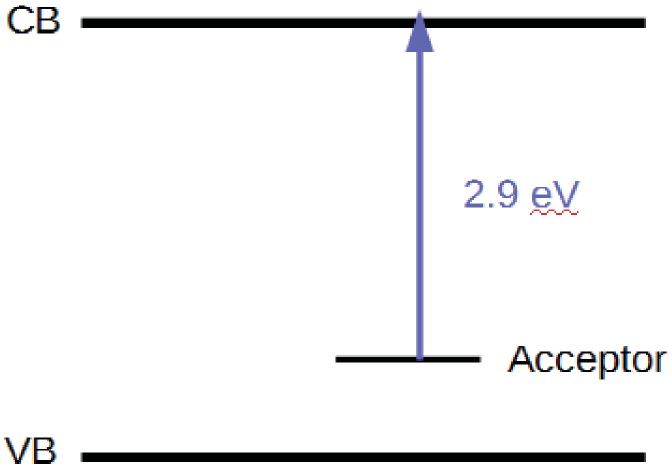

Figure 28: Model of PPC showing light exciting electrons from an acceptor level to the conduction band.

We will discuss hydrogen in Section 4.3.

As discussed in the literature, oxygen vacancies are very important and it is easy to change their concentration. Since the growth process is prone to excess oxygen concentrations, different batches of crystals may have differing initial oxygen vacancy concentrations. This can be experimentally confirmed by looking at an EPR comparison of working (good PPC) and non-working (bad PPC) batches of as-received samples of STO (Figure 29). The iron-oxygen-vacancy complex, (Fe-V_{O}), is over an order of magnitude larger in the working samples. Annealing in an oxygen deficient atmosphere, such as under vacuum or in the presence of a reducing gas, should allow the creation of enough oxygen vacancies so that this vacancy complex will form.

In conclusion, we know that oxygen vacancies are necessary for PPC, but not exactly why. Fujishiro [Fujishiro and Mochizuki, 2005] noticed that oxygen vacancies will trap photo-generated carriers and ultra-violet light will lead to a change in the dielectric and transport properties of STO. Additionally, titanium oxygen vacancy complexes (V_{Ti} - V_{O}) can act as hole traps. Sub-gap light causes an electron to go from the acceptor level to the conduction band, resulting in PPC (Figure 28).

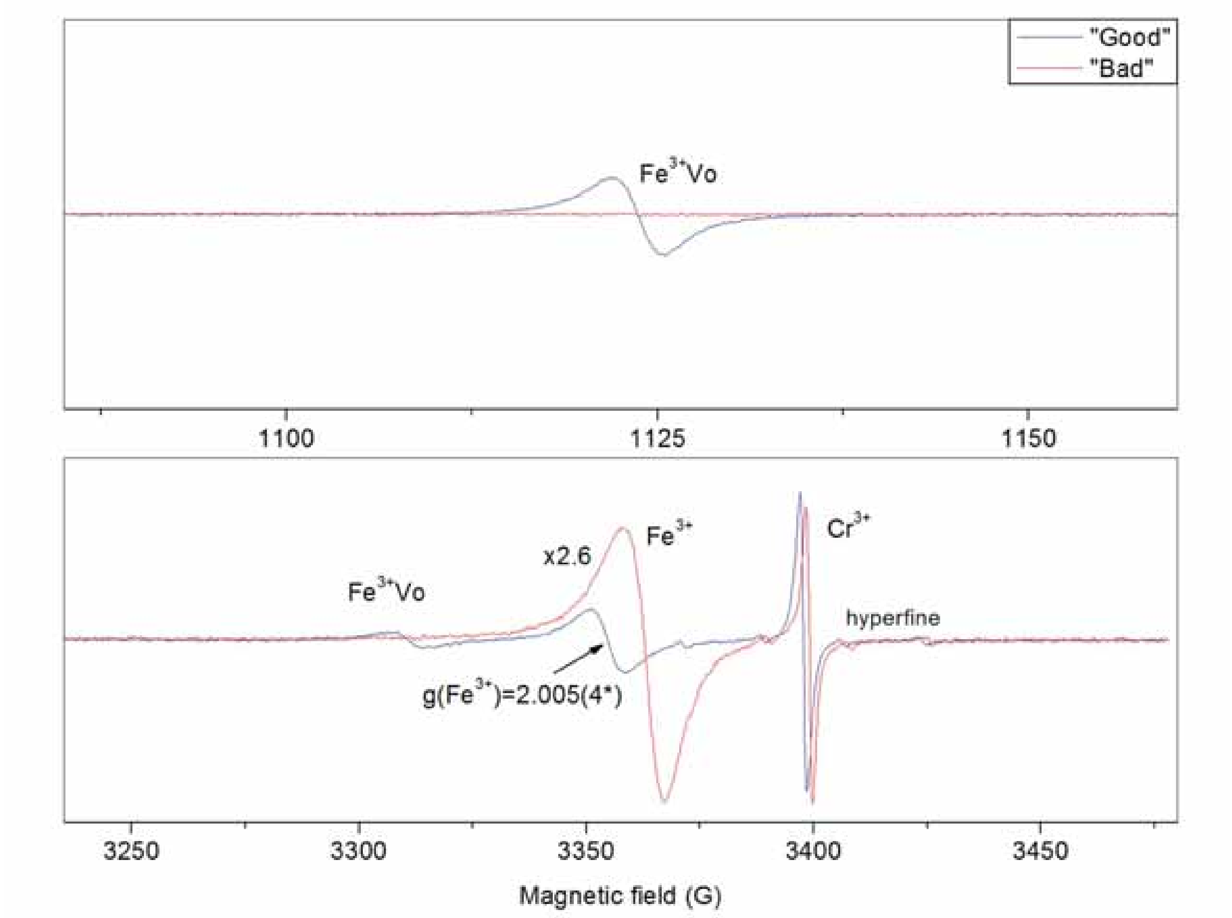

Figure 29: EPR Spectra, courtesy of M.E. Zvanut, comparing working (Marketech unnumbered batch) and non-working (Mateck 14032715) batches, in regards to the ability of an SrO anneal to induce PPC in the sample. Notice that Fe-V_O is over an order of magnitude higher in working samples.

4.2 Vacuum Annealing

It is known that the process of crystal reduction results in the formation of anion vacancies, particularly oxygen vacancies (V_O) and complexes thereof [Badalyan et al., 2013]. Many studies on the effects of oxidation and reduction of STO use a temperature of 900°C for all or part of their work [Faughnan, 1971, Blazey and Weibel, 1984, Wild et al., 1973, Stocker et al., 2010], so this temperature was mainly used for the vacuum annealing step. A few samples were annealed at a lower temperature of 800°C, although even lower temperatures might be sufficient. Figure 11 shows the spectra, before and after 405 nm LED light exposure of a sample annealed under rough vacuum, and then allowed to cool rapidly in the ambient air. A roughing pump was used to evacuate the three inches of airspace in the ampoules to approximately 50-100 mTorr, as measured by a convectron gauge, calibrated for N_2, on the sealing stand. Other ampoules were evacuated with a turbo pump, which has a built in pressure gauge. These high vacuum anneals, like that displayed in Figure 30, occurred around pressures of 10^{-4} to 10^{-5} mbar.

While in both vacuum anneals (rough and high vacuum) the FTIR spectra change with light exposure, this change is not due to PPC. Compare the vacuum anneals (Figure 11 and Figure 30) with Figure 12, which has PPC. The vacuum annealed samples are much more conductive to begin with, resulting in lower IR transmission. Only the InSb detector is sensitive enough to even get a signal through the vacuum annealed chips, which are much darker in color. Another sign that the change is not due to PPC is the behavior of the peak at 520 nm. Although it is present in both types of vacuum annealed samples, it has much less of a change after light exposure than PPC samples do.

Several experiments were performed to determine whether a vacuum anneal is a necessary step to condition the chip for the PPC-inducing SrO anneal. Chips from previously non-working batches were subjected to various vacuum annealing conditions, before SrO annealing. Figure 31 and Figure 32 show the spectra of two chips from the same batch (Mateck 14032715) that were first rough vacuum annealed at 900°C for different durations (1 hr or 19 hr), then SrO annealed at 1200°C for 1 hr. Note that this is the same batch as Figure 10, which did not work with only an SrO anneal. It is also the same batch as the non-working EPR sample in Figure 29, which had

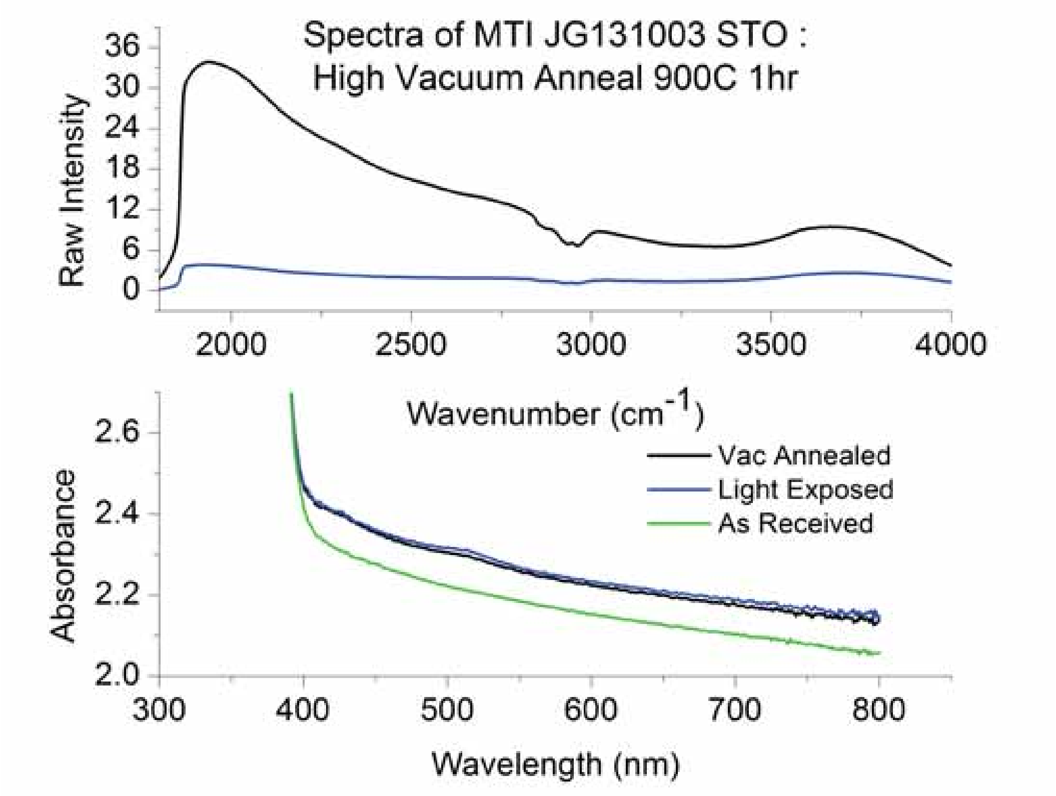

Figure 30: (top) FTIR spectra with InSb detector of a high vacuum annealed STO. Notice that unlike Figure 12, which has PPC, the annealed intensity is much lower to begin with, so the drop with light exposure is much smaller. (Bottom) UV Vis spectra of the same sample. Note that the peak at 520 nm has much less of a change with light exposure, than PPC samples do.

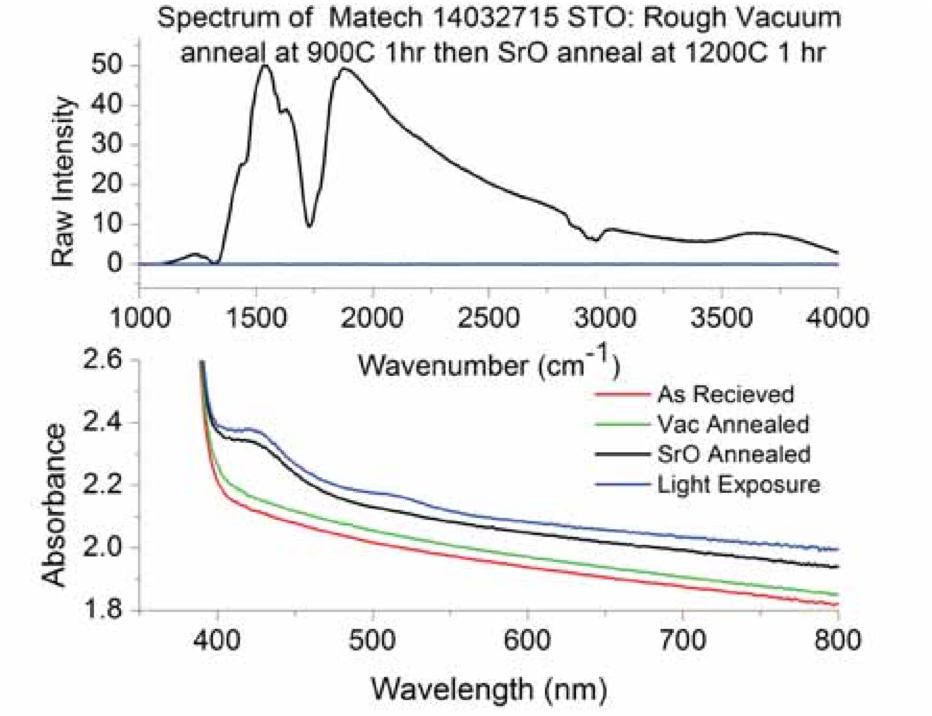

Figure 31: (top) FTIR spectra with MCT detector showing PPC. (bottom) UV Vis spectra. Note that the 430 nm peak is not present after the vacuum anneal, and grows with light exposure after SrO anneal.

a low concentration of iron oxygen vacancy complexes ($\mathrm{Fe}^{3+} - V_{\mathrm{o}}$). Both long and short duration vacuum pre-annealed chips display PPC.

Another batch (Marketech 0047786) that did not have PPC upon an SrO anneal only (Figure 9) was made to have PPC by doing either a high vacuum anneal (Figure 33) or a rough vacuum anneal (Figure 34) for 1 hr at 900°C, before the 1200°C SrO anneal. Again, both chips, rough or high vacuum, displayed PPC after the SrO anneal. In conclusion, adding a vacuum annealing step introduces more oxygen vacancies and complexes thereof that are needed for the SrO anneal to induce PPC.

While all the vacuum annealed samples displayed PPC after SrO annealing, the presence of the peak at 430 nm before light exposure depends on the details of the vacuum pretreatment. The difference in behavior depends on the oxidation state of the iron impurity ions within the crystal. Reduction changes the charge states of the impurities, so it make sense that the degree of reduction would influence the behavior of this peak. Both the duration (long or short) and level of vacuum (rough or high) affect the degree of reduction and hence the behavior of the 430 nm

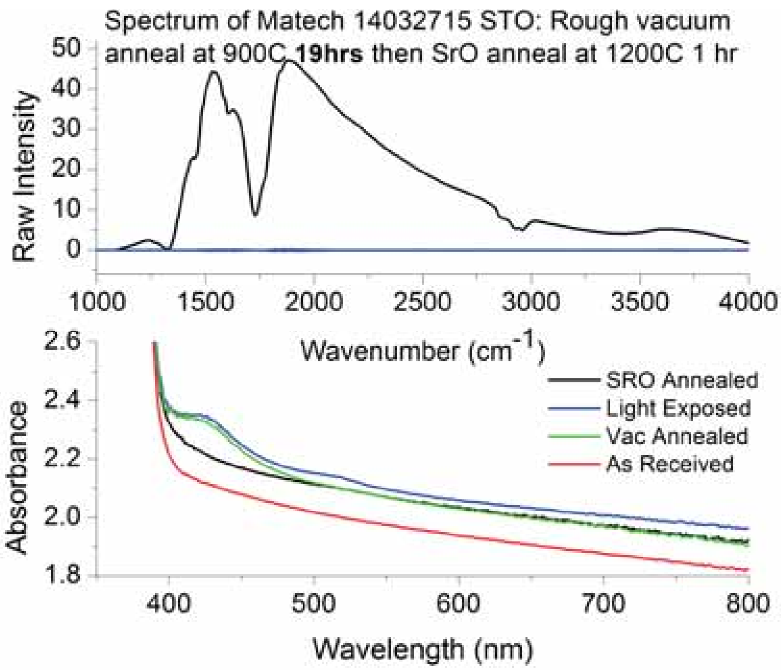

Figure 32: (top) FTIR with MCT detector showing PPC. (bottom) UV Vis spectra. Note that the 430 nm peak is present after the vacuum anneal and does not change with light exposure.

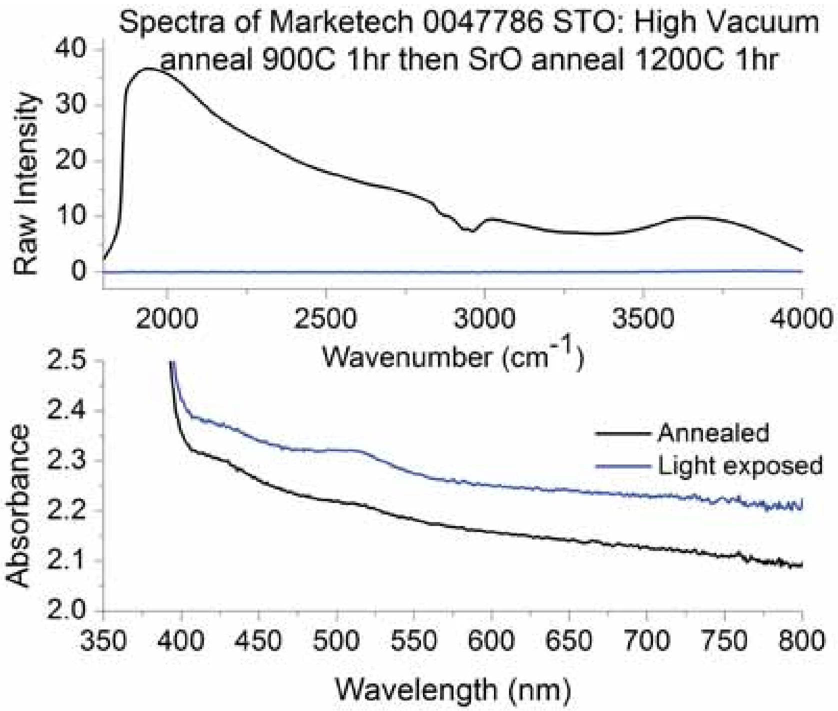

Figure 33: (top) FTIR spectra with InSb detector showing PPC. (bottom) UV Vis spectra showing 430 nm peak present after annealing.

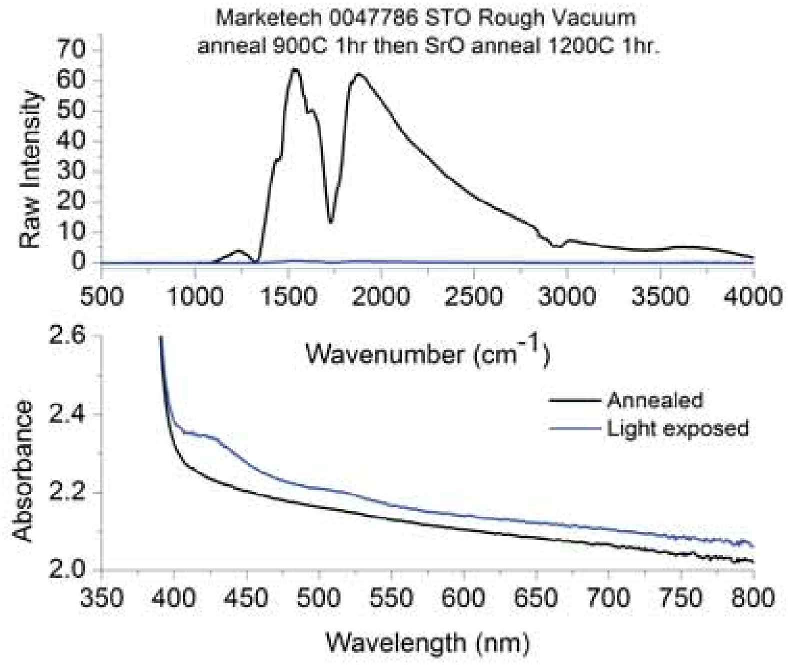

Figure 34: (top) FTIR spectra with MCT detector showing PPC. (bottom) UV Vis spectra showing 430 nm peak growing with light exposure.

peak. A short duration vacuum anneal (Figure 31) does not have the peak after SrO anneal and before light exposure, while a long duration vacuum anneal does (Figure 32). In vacuum anneals of a short duration, the high vacuum pretreatment results in the 430 nm peak being present before light exposure (Figure 33), while the rough vacuum annealing (Figure 34) does not.

The reason is that more of a reduction treatment from a higher vacuum anneal, or an anneal of longer duration, induces more oxygen vacancies and complexes thereof into the chips. Recall that the peak at 430 nm indicates iron is in the Fe^{4+} state in the crystal. More oxygen vacancies result in iron appearing as Fe^{4+}, the details of which are not obvious and are given in 4.4. This is in agreement Section 3.2 where the cooling rate affected the appearance of this peak. A faster cooling rate also locks in more oxygen vacancies into the chip resulting in the Fe^{4+} charge state [Wild et al., 1973, Szot and Speier, 1999].

Spectrally, the duration or level of vacuum (high or rough) used in the vacuum annealing step is not critical, as long as it introduces enough oxygen vacancies to induce PPC with the SrO anneal. A light to moderate reduction is suggested, which results in a light to medium grey chip. This color indicates there are some oxygen vacancies present in the crystal, but not so many that the sample is too conductive before the SrO anneal. Additionally, performing a vacuum annealing pretreatment on samples that will display PPC with just an SrO anneal, still exhibit PPC. So adding more oxygen vacancies than needed does not prevent PPC. However, a sample that is very conductive initially will have its change in conductivity muted, since it already has many free electrons to start with. Chapter 6 will discuss the electrical difference that occurs depending on the presence of the 430 nm peak before light exposure.

4.3 Role of Hydrogen

Hydrogen (H) is an abundant impurity and can have a strong effect on the electrical conductivity of semiconductors [McCluskey and Haller, 2012]. Experiments indicate that H is a shallow donor and can readily be incorporated into STO [Weber et al., 1986, Tarun and McCluskey, 2011]. This places its energy level near the conduction band (Figure 27). Hydrogen can attach to dangling bonds, and fully or partially passivate acceptor levels, improving electrical mobility [McCluskey and Haller, 2012]. Understanding hydrogen interactions with native defects such as vacancies is crucial. These interactions may play a role in the proton conduction of perovskite oxides, which is an important issue for fuel cell development [Norby, 2009]. The concentrations and positions of hydrogen impurities in the unit cell are important considerations for applications in nonlinear optics and holographic storage [Houde et al., 1987].

Hydrogen can act as a catalyst to produce oxygen vacancies and other positive charge centers [Scott et al., 2001]. H acts exclusively as a donor in most oxide materials, and prefers to stay close to the oxygen atoms, forming strong O-H bonds [Fongkaew et al., 2013]. Across all types of oxides, the proton activation energy is usually around two-thirds the activation energy for oxygen vacancy migration [Norby, 2009]. This is because the proton is reliant on the oxide sublattice. Hydrogen substituting for an oxygen causes the formation energy of this configuration to be intimately linked with the oxygen chemical potential, and hence the dependence of proton conductivity on the oxygen partial pressure [King and Veal, 2011].

Characterizing hydrogen impurities is best done by the technique of infrared spectroscopy. In as grown STO, an IR absorption peak near 3500 cm^{-1} is observed [McCluskey and Haller, 2012, Klukhuhn et al., 1970]. Using the same naming convention as [Tarun and McCluskey, 2011], we will call this line H_I. It has been established that this line is due to the stretching mode of the O-H dipole [Weber et al., 1986, Houde et al., 1987, Klukhuhn et al., 1970, Brebner et al., 1981]. Applications of uniaxial stress and electric field in polarized IR absorption spectroscopy and polarized Raman scattering measurements above and below the transition temperature allowed much information about the O-H dipole environment to be deduced [Weber et al., 1986].

Two models for the position of the hydrogen atom emerged from all these data. One assigned the hydrogen atoms to the position on the faces of the cubic cell, between the Sr and O atoms [Houde et al., 1987]. The other proposed a model where the O-H dipole vibrates along the line that connects oxygen neighbors [Weber et al., 1986]. However, one theory [T-Thienprasert et al., 2012] calculated the ground state configuration of the O-H vibrational frequency to be 2745 cm^{-1}, in a direction inconsistent with the measured polarized IR results. This peak is not observed experimentally. They assigned the 3500 cm^{-1} mode to H in a Sr vacancy (H-V_{Sr}). Complexes of H and cation vacancies have been found in many oxides, so this a plausible explanation [Lavrov et al., 2002]. Other theoretical calculations have the H_I line at 3500 cm^{-1} as being due to an interstitial hydrogen ion, H_i^+ [Varley et al., 2014].

Other signatures of hydrogen can also be present in the IR region of the spectrum. Two absorption peaks at 3355 and 3384 cm^{-1}, denoted H_{II}, are introduced by annealing in hydrogen [Tarun and McCluskey, 2011]. Both the H_I and the H_{II} peaks showed the expected isotope shift to lower frequencies when samples were annealed in deuterium [McCluskey and Haller, 2012]. However, the ratio of H_I to H_{II} peak areas varies between samples, and their thermal kinetics are different [Tarun and McCluskey, 2011]. Annealing samples in a mixture of hydrogen and deuterium, new H_{II} peaks appeared, showing that the H_{II} center contains two hydrogen atoms [McCluskey and Haller, 2012]. Theoretical modeling indicates these two peaks may be the result of two hydrogen molecules in a titanium vacancy, 2H-V_{Ti} [Fongkaew et al., 2013]. The coupling between the stretch vibration modes leads to a split in the vibrational frequencies. Additionally, annealing temperatures of 400-500°C cause the release of 'hidden' hydrogen, which cannot be detected with IR spectroscopy [Varley et al., 2014]. It has been found that hidden hydrogen exists in the form of a hydrogen molecule, H_2, in ZnO and dissociates around 400°C [Shi et al., 2004].

Figure 35 shows the behavior of hydrogen in STO observed with low temperature FTIR, especially in regards to PPC. Notice that the H_I line is present after annealing, and increases upon light exposure. The "3500 cm^{-1} line" shifts almost linearly to higher wavenumbers with decreasing temperature, so at 180 K it is at 3505 cm^{-1} [Klukhuhn et al., 1970]. Another line at 3521 cm^{-1} appears after light exposure. High resolution spectra show multiple (around 4) satellite lines that sharpen with decreasing temperature above the phase transition around 105 K, but the relative intensity of these lines varies from sample to sample [Houde et al., 1987]. In iron doped samples, these peaks were tentatively attributed to hydrogen complexes with Fe^{3+} and $(Fe^{3+} - V_O)$ by EPR measurements [Grone et al., 1990]. The line at 3521 cm^{-1}, which the authors labeled C, is attributed to a $(Fe^{3+} - V_O)$ center. They also measured the temperature dependence of the H_I line and a total of 13 satellite lines above the phase transition temperature. These satellites have the same temperature dependent shift as the main H_I line [Houde et al., 1987, Grone et al., 1990]. Theoretical calculations [T-Thienprasert et al., 2012] yield several lines around 3500 cm^{-1} that involve a strontium vacancy and hydrogen: (H-V_{Sr}) line at 3505 cm^{-1}, (2H-V_{Sr_I}) line at 3523 cm^{-1} and (2H-$V_{Sr_{II}}$) line at 3527 cm^{-1}. No other hydrogen lines are present in the spectra. UV Vis spectra of the same sample are shown in Figure 36, where the appearance of the 520 nm peak indicates PPC.

Since the peaks are temperature dependent and sharpen at lower temperatures, we also looked at FTIR spectra at 125 K (Figure 37). Here we observe the same general behavior, with a few differences, due to the lower temperature. The H_I line is now shifted to 3510 cm^{-1}, and there are now two, and possibly a third, satellite line that appears after light exposure. Continuing to use the naming convention of Grone [Grone et al., 1990], the C line is now at 3527 cm^{-1}, and a new satellite line at 3518 cm^{-1} is the B line. The B line has also been tentatively attributed to a $(Fe^{3+} - V_O)$ center. The possible peak at 3530 cm^{-1}, if not a noise blip, would be the C3 line.

The change in behavior of these satellites suggest that the defect responsible for PPC may involve hydrogen. If the satellite lines are due to hydrogen near a $(Fe^{3+} - V_O)$, hydrogen is forming the O-H bond, but the presence of the vacancy defect complex nearby perturbs its frequency. The various satellite lines may depend on the direction the defect complex is relative to the O-H molecule. During annealing the hydrogen would change its position within the lattice, perhaps occupying the V_O. The frequency of this defect would be very low, 1000 cm^{-1} or less, which is

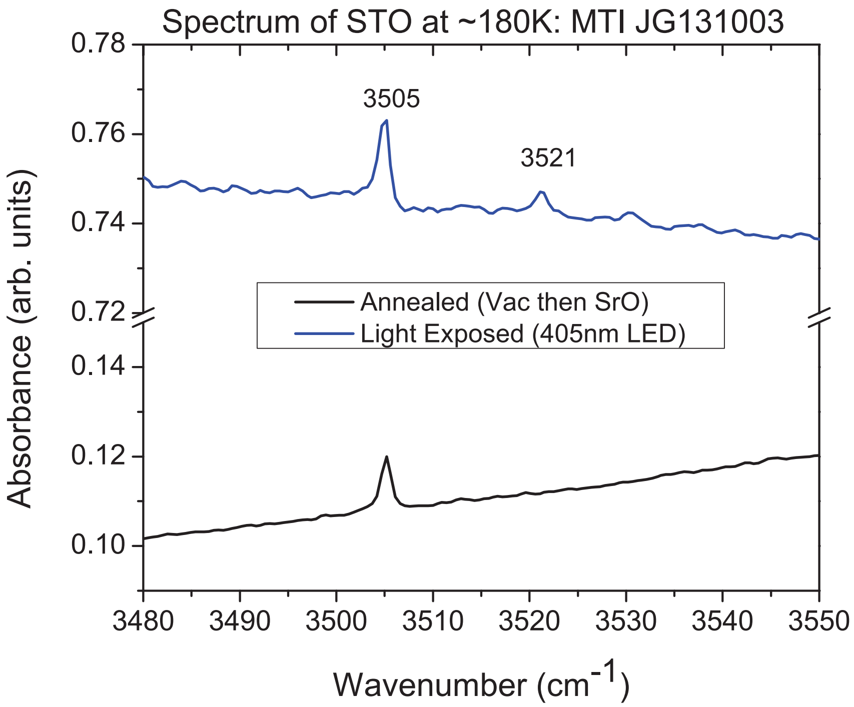

Figure 35: FTIR spectra at 180 K with InSb detector of STO with PPC. The 3505 cm^{-1} peak increases and the 3521 cm^{-1} peak appears after light exposure.

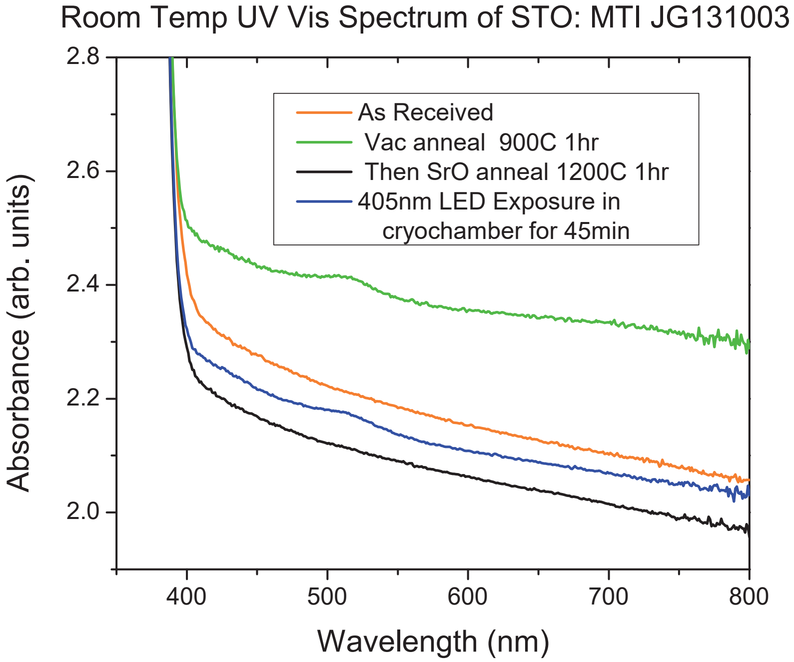

Figure 36: UV Vis of the sample in Figure 35. The 520 nm peak appears after light exposure, indicating PPC.

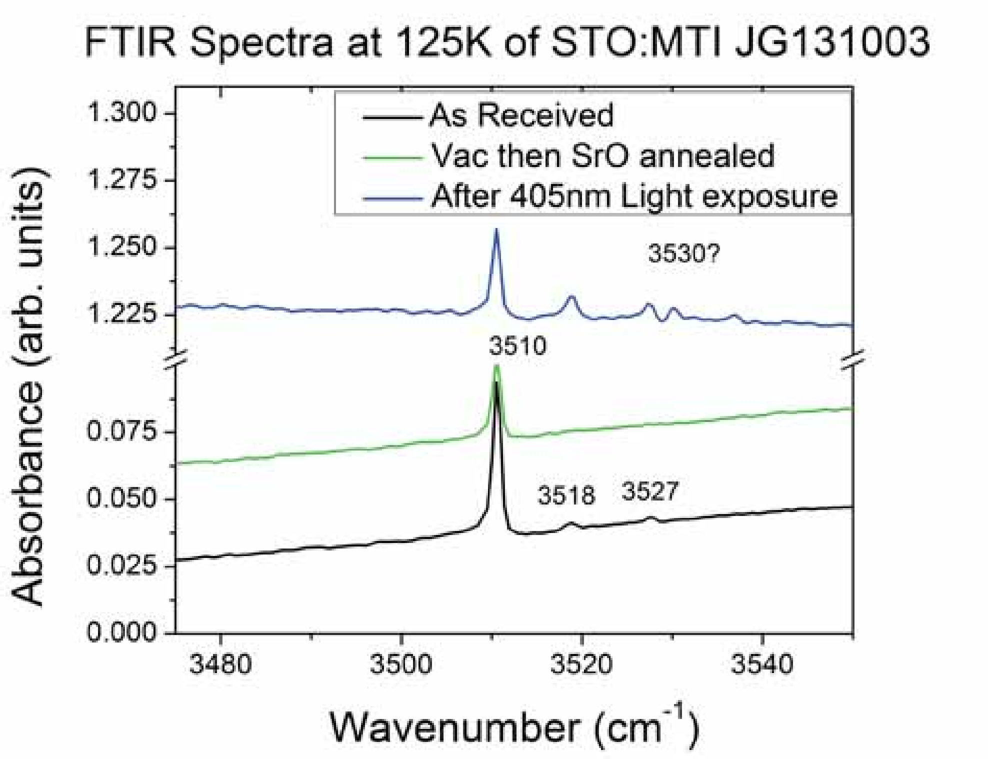

Figure 37: Hydrogen line and satellites behavior during PPC at 125 K. Notice that the intensity of the main peak at 3510 cm^{-1} decreases with annealing and slightly increases with light exposure. The satellite lines, which are present in as received crystal, disappear upon annealing and return upon light exposure.

outside the range we observe in the IR. During light exposure it would then move back onto the oxygen atom, again forming the O-H bond.

However, if the H_I and satellite lines are actually various complexes of a strontium vacancy and hydrogen, a different explanation emerges. During annealing, the hydrogen atoms rearrange themselves forming H_2 molecules within the strontium vacancies. This H_2 would be invisible in the IR, since the molecule is symmetric and would not have a changing dipole moment. Light exposure then results in the dissociation of the hydrogen molecule, allowing the individual hydrogens to decorate the strontium vacancies again and the return of the satellite lines. Hydrogen is a shallow donor, so would explain the large increase in free carriers seen during PPC. Conversely, this theory does not explain why oxygen vacancies are needed for PPC (Section 4.1). Additionally, the annealing conditions argue against the formation of strontium vacancies, which would be crucial to this mechanism of PPC (Chapter 8).

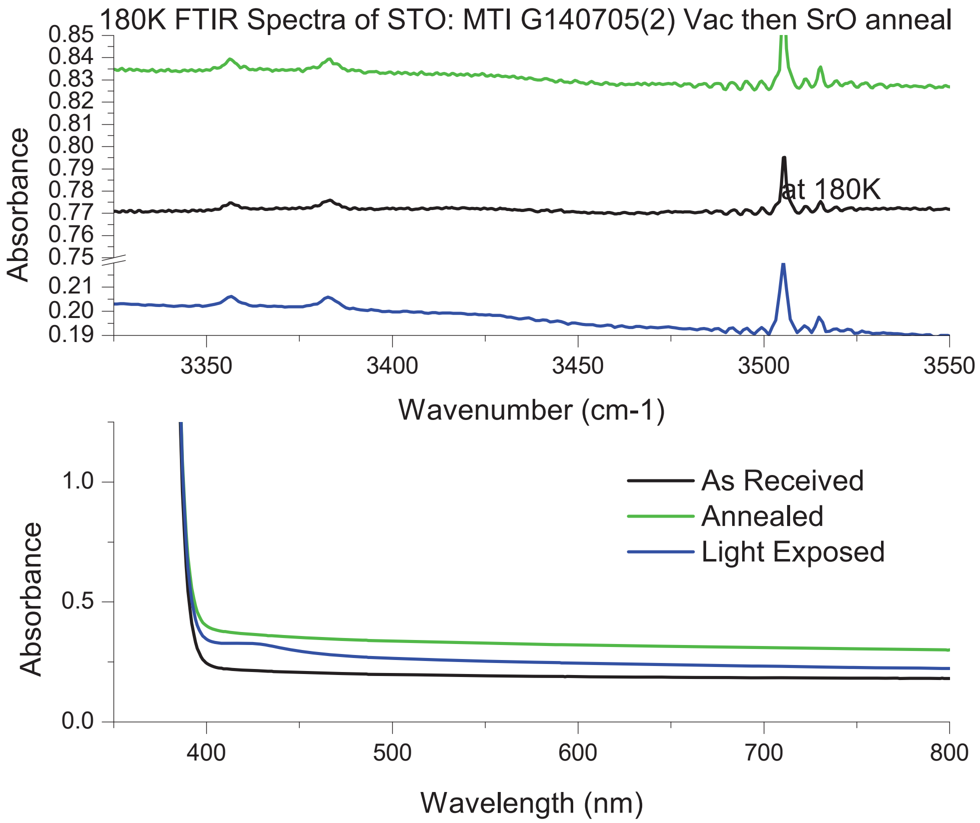

Figure 38: H_{II} lines are present in this sample, which is not usually the case. This sample did not show PPC after the usual treatments.

We discovered something interesting when testing some 2 sided EPI polished samples from MTI. We could not induce PPC following our usual procedure of a vacuum anneal followed by an SrO anneal (Figure 38). The main difference between this sample and other samples that worked is the presence of the H_{II} lines. Additionally, the UV Vis spectrum is flatter than any other samples, although the slope does vary a little between batches. Next we tried to see if we could find a way to make this batch work. Annealing in the open air at temperatures around 1200°C will remove hydrogen from STO crystals, as evidenced by both the H_I and H_{II} peak intensities dropping to zero [Tarun and McCluskey, 2011].

We annealed the EPI polished chip by placing it in an ampoule with one end open and putting in the tube furnace at 1200°C. A 1 hour anneal failed to noticeably change the amount of hydrogen. A 19 hour anneal significantly decreased the intensities of both the H_I and H_{II} lines, although they are still present (Figure 39). We decided to then try our normal recipe of a vacuum anneal

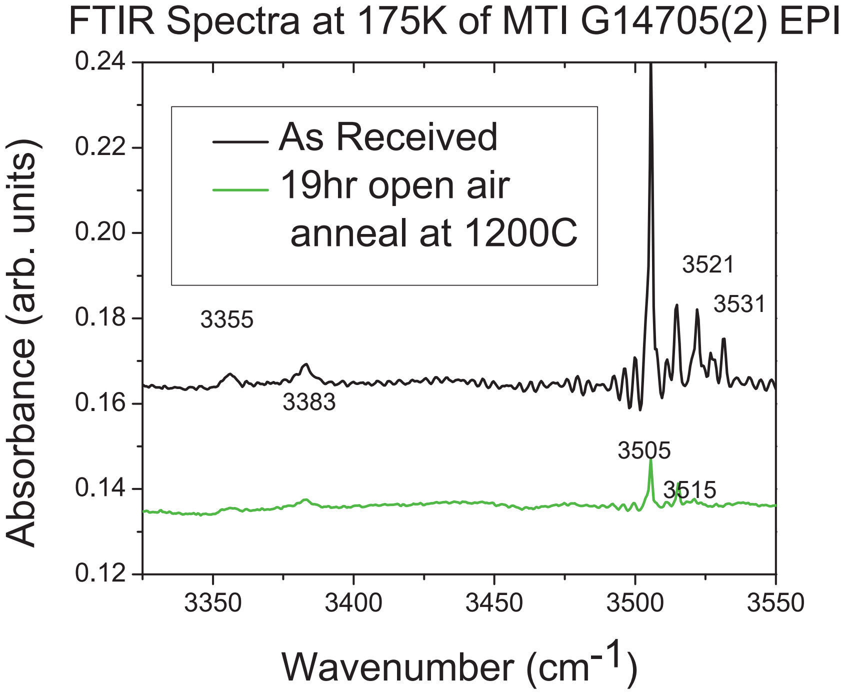

Figure 39: The intensity of the H_{II} lines reduce after a long open air anneal.

followed by an SrO anneal. After removal of most of the hydrogen in the H_{II} lines, we were able to induce PPC in the sample. See Figure 40 and Figure 41 for the FTIR and UV Vis spectra, respectively. This shows that too much hydrogen, at least in the form of H_{II} lines, will prevent PPC. This could be due to hydrogen passivating the titanium vacancy. If the PPC defect is a $V_{\mathrm{Ti}} - V_{\mathrm{O}}$ pair, filling the titanium vacancy with hydrogen would prevent it from being able to participate in PPC.

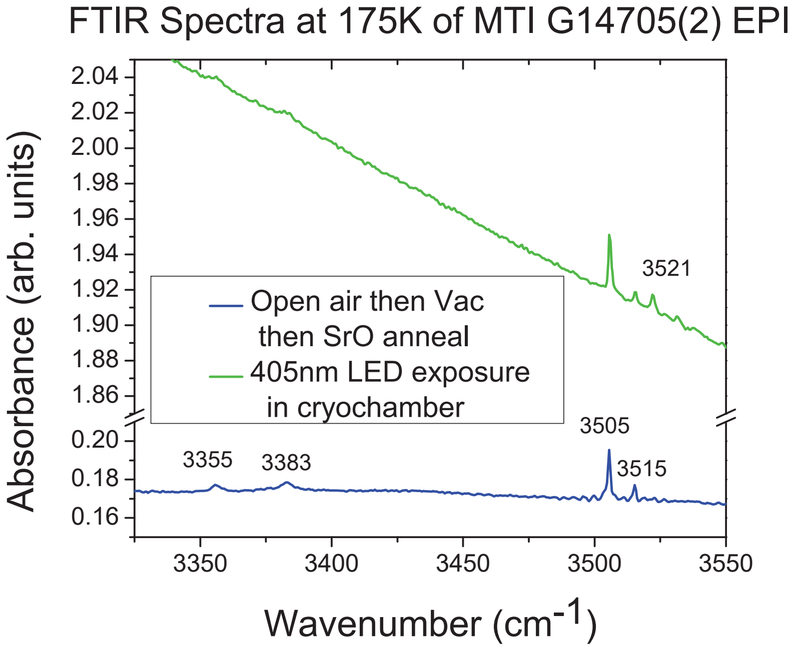

Figure 40: PPC could be induced in this sample by the usual method after removing the H_{II} via a long air anneal. See Figure 41 for UV Vis spectra of this chip.

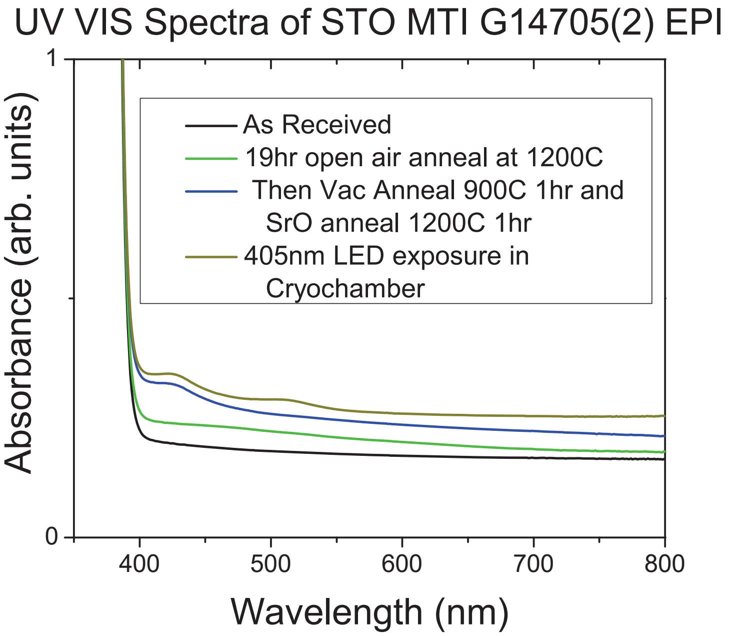

Figure 41: UV Vis spectra of the same chip as in Figure 40. PPC could be induced in this sample by the usual method after removing the H_{II} via a long open air anneal.

4.4 Iron Doped

Transition metals are believed to enter the lattice substitutionally on the Ti^{4+} sites, and have been seen in photochromic studies [Faughnan, 1971]. Iron is one of the most common transition metal impurities found in semiconductors and its defect levels within the band gap have been studied [Morin and Oliver, 1973]. Iron can occur in multiple valence states, from 2+ to 5+, with the $\mathrm{Fe}^{3+/4+}$ level being higher in the band gap than the $\mathrm{Fe}^{4+/5+}$ level (Figure 27). Additionally, iron-oxygen vacancy complexes introduce an additional set of energy levels within the band gap that are lower than the corresponding iron level with no associate oxygen vacancy.

Cooling is a non-equilibrium process, and faster cooling will lock in more oxygen vacancies and vacancy complexes $(\mathrm{Fe}^{3+}-V_{\mathrm{O}})$ (See Section 4.1). When $(\mathrm{Fe}^{3+}-V_{\mathrm{O}})$ is present it reacts with Fe^{3+} trapping an electron in the following way:

$$\mathrm{Fe}^{3+}+(\mathrm{Fe}^{3+}-V_{\mathrm{O}})\rightarrow \mathrm{Fe}^{4+}+(\mathrm{Fe}^{2+}-V_{\mathrm{O}}) \tag{4.1}$$

resulting in Fe^{4+} and the metastable complex $(\mathrm{Fe}^{2+}-V_{\mathrm{O}})$ [Morin and Oliver, 1973]. It makes sense that iron would want to be in the 4+ state, since iron is substituting for Ti^{4+} and would be in the same valence state as the normal lattice site occupant. The Fe^{4+} charge state is correlated with a higher free-electron density, as discussed in Section 6.3.

Iron has a complex role in STO, as evidenced by its many valence states and ability to form reactive complexes with oxygen vacancies. Additionally, EPR results suggest that iron, in the form of iron oxygen vacancy complexes, are needed for PPC (Section 4.1). Therefore, we investigated the effects iron doping has on PPC. Performing the standard SrO anneal on iron doped STO did not yield PPC. Figures 42 and 43 show the case for 0.005 wt% and 0.01 wt% Fe doped STO, respectively.

Since not all batches work with an SrO anneal only, pre-treating the chip with a vacuum annealing was also tried. As we have seen, this is often a necessary step to condition the chip by introducing more oxygen vacancies. Figure 44 shows an iron doped sample that was first treated with a high vacuum anneal (900°C for 1 hr) followed by an SrO anneal. There is no PPC, so the amount of oxygen vacancies is not the issue.

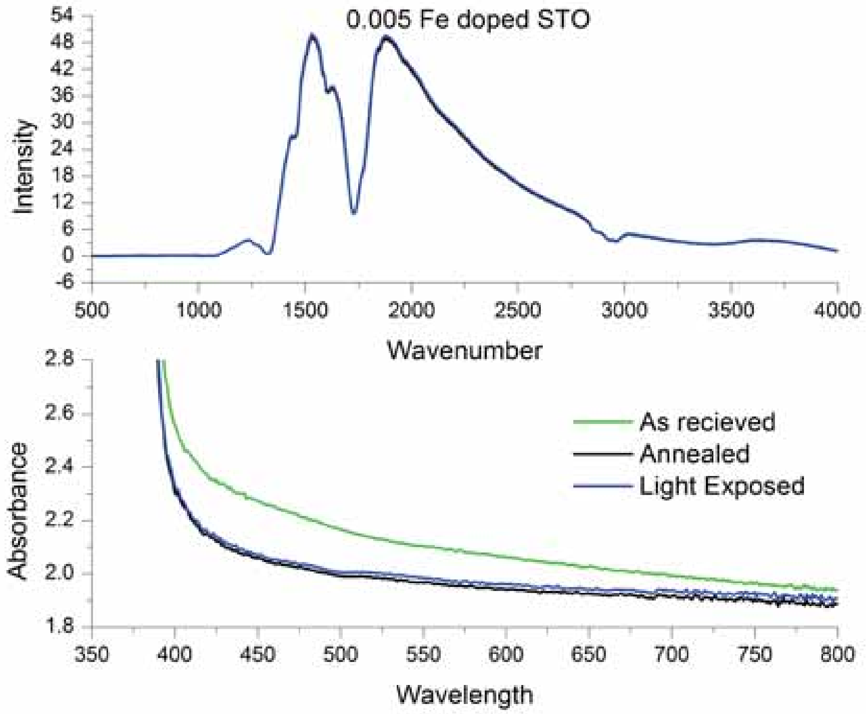

Figure 42: SrO anneal on a 0.005 wt% Fe doped STO does not show PPC. Top: Room temperature FTIR spectra. Bottom: UV Vis spectra.

One possible reason that we have not been able to induce PPC in iron doped samples is the presence of the H_{II} lines in the as-received samples (Figure 45). As we have seen previously, strong H_{II} lines will prevent PPC. Additionally, open air annealing for a long duration ($\sim$ 44 hrs) failed to significantly reduce the H_{II} lines. Despite this, we tried to induce PPC in the air annealed crystal per our usual procedure of a vacuum anneal followed by an SrO anneal. Figure 46 shows the lack of PPC, confirming the correlation between H_{II} peaks and non-working samples.

As previously discussed, the presence of the H_{II} peaks may be due to hydrogen in a titanium vacancy. Its presence passivates the titanium vacancy, preventing it from participating in PPC. This provides evidence that a titanium vacancy oxygen vacancy pair may be responsible for PPC. Iron may make the H_{II} complexes more stable, and we have already seen that these defects inhibit PPC. Too high of an iron concentration might suppress PPC, similar to how a large iron impurity concentration will prevent a crystal from exhibiting color switching properties [Luiskutty and Ouseph, 1973]. This also rules out theories that PPC may involve an iron oxygen vacancy complex, because more iron would be good in that case.

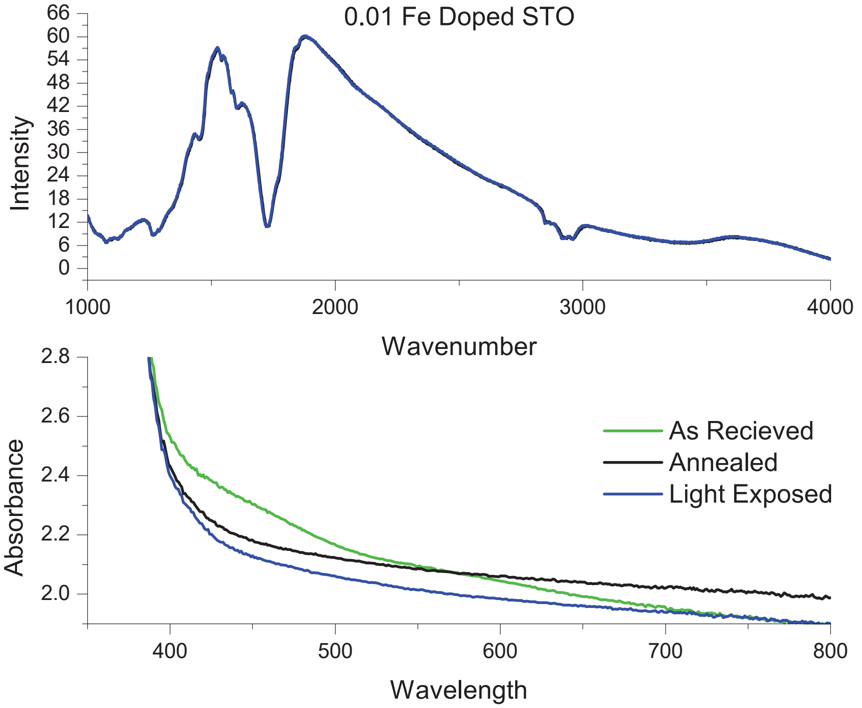

Figure 43: SrO anneal on a 0.01 wt% Fe doped STO does not show PPC. Top: Room temperature FTIR spectra. Bottom: UV Vis spectra.

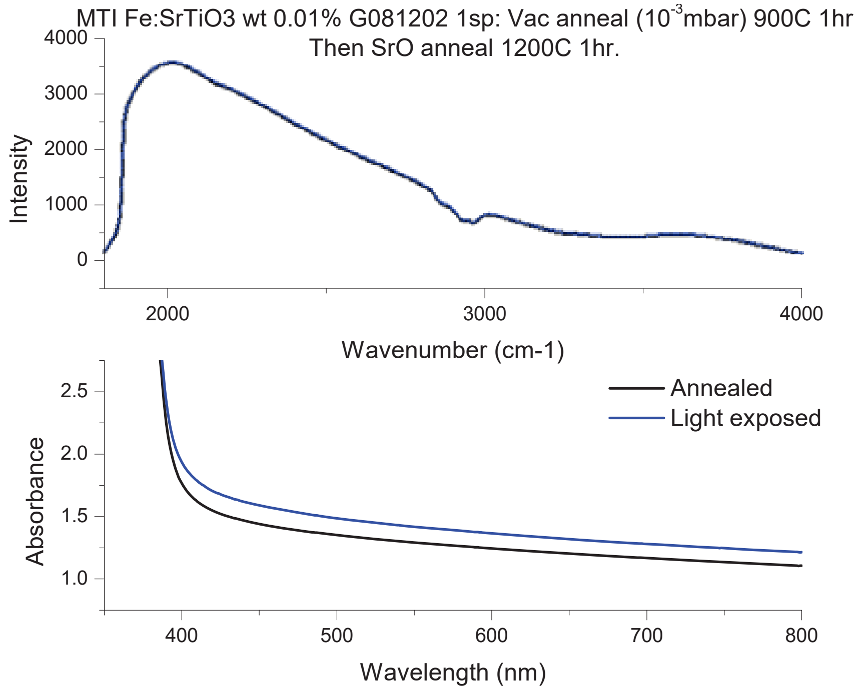

Figure 44: Vacuum anneal followed by SrO anneal on 0.01wt% Fe doped STO. Sample does not exhibit PPC. Top: Room temperature FTIR spectra. Bottom: UV Vis spectra.

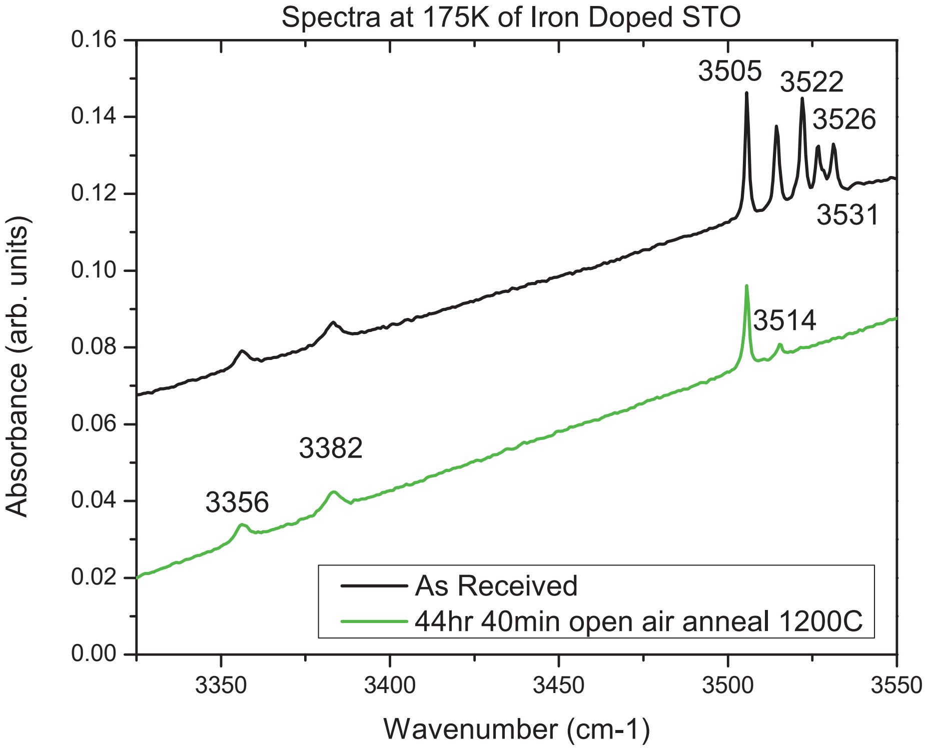

Figure 45: Low temperature FTIR spectra at 175 K of iron doped STO. Notice the presence of the H_{II} lines which are not normally observed in as received samples. Unlike undoped samples, open air annealing failed to remove the H_{II} line.

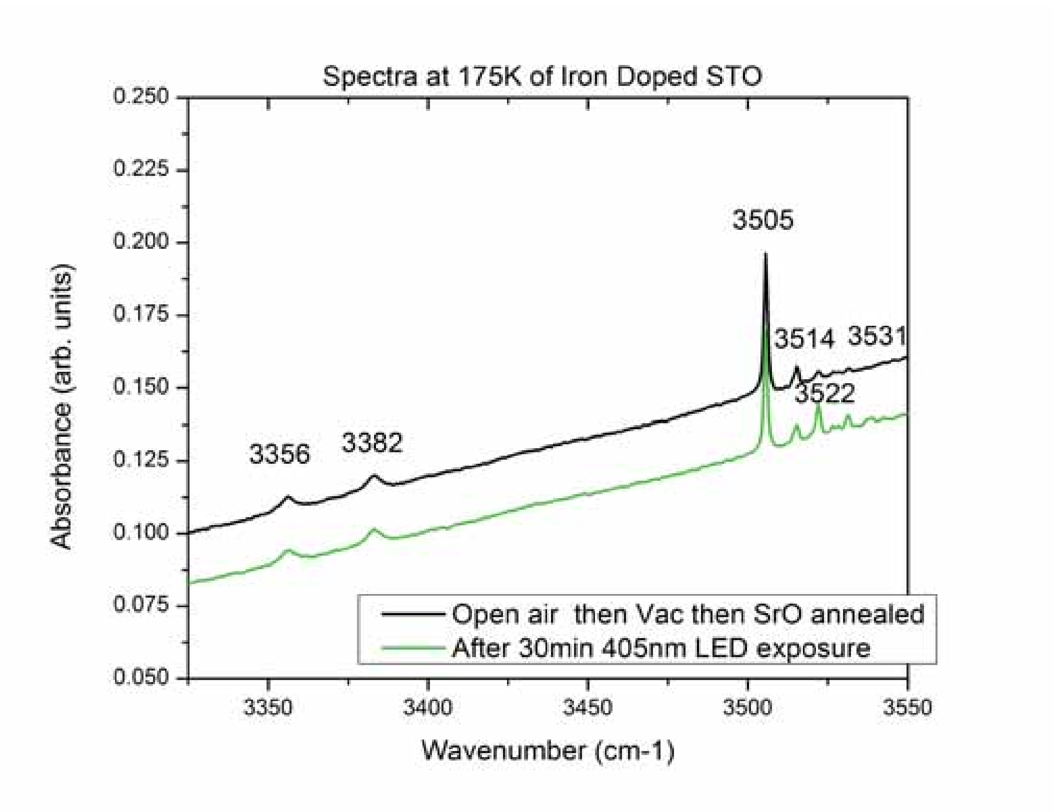

Figure 46: Low temperature FTIR spectra at 175 K of iron doped STO. No PPC is observed after the usual annealing procedure of a vacuum then SrO anneal after the long duration open air anneal.

4.5 EPR Changes with PPC

As-received STO chips contain Fe^{3+} and Cr^{3+} signatures. SrO annealing removes the Fe^{3+} lines, while Cr^{3+} remains. Exposing to light removes the Cr^{3+} line (Figure 47). This indicates that chromium might be involved in PPC, although the disappearance could just be due to the changing charge states of the impurities that happens with light exposure. Additionally, another line grows by a factor of 3. This line is similar to the Fe^{3+} resonance (g=2.007), but has a slightly different g value (g =2.0131). Ensign and Stokowski [Ensign and Stokowski, 1973] observed a line with a similar g value to Fe^{3+}. The element responsible for this line was never identified, but they designated it a $X - O^-$ center. Their possible guesses for the identity of the $X - O^-$ center could be a Sr or Ti vacancy, Mg or another Al line (one Al line was already observed) [Ensign and Stokowski, 1973]. This center is a hole trap that is stable at room temperature. The intensity of this band is constant and present in Al doped and quenched samples, but not observed in iron doped samples. Additionally, the $X - O^-$ center corresponds to an optical absorption band around 500 nm, which is quite close to our PPC peak around 520 nm.

While it is not certain if we are seeing the same center Ensign and Stokowski observed, if so, it is possible that this center could be very important to PPC. A hole trap could be a necessary defect needed for PPC to occur. Titanium vacancies are known to be hole traps [Fujishiro and Mochizuki, 2005], so of the possible centers Ensign and Stokowski discuss, this seems most likely. This model is also consistent with the idea that the SrO anneal creates titanium vacancies [Tarun et al., 2013, Poole and McCluskey, 2016].

Ensign and Stokowski's $X - O^-$ center has a corresponding optical absorption around 500 nm [Ensign and Stokowski, 1973]. This peak is in the same (though not exact) region of the spectrum as our PPC peak at 520 nm, so it is worth considering that they observed the same EPR signature we see. Additionally, the intensity of the optical absorption band does not correlate well with the concentration of impurities such as aluminum, but is observed in quenched samples and not in iron doped samples [Ensign and Stokowski, 1973]. As we have shown, iron doped chips did not have PPC, and the peak at 520 nm was not observed. Other literature shows that quenching locks in the peak at 520 nm, while a slow cooling will destroy it [Wild et al., 1973]. The behavior of our

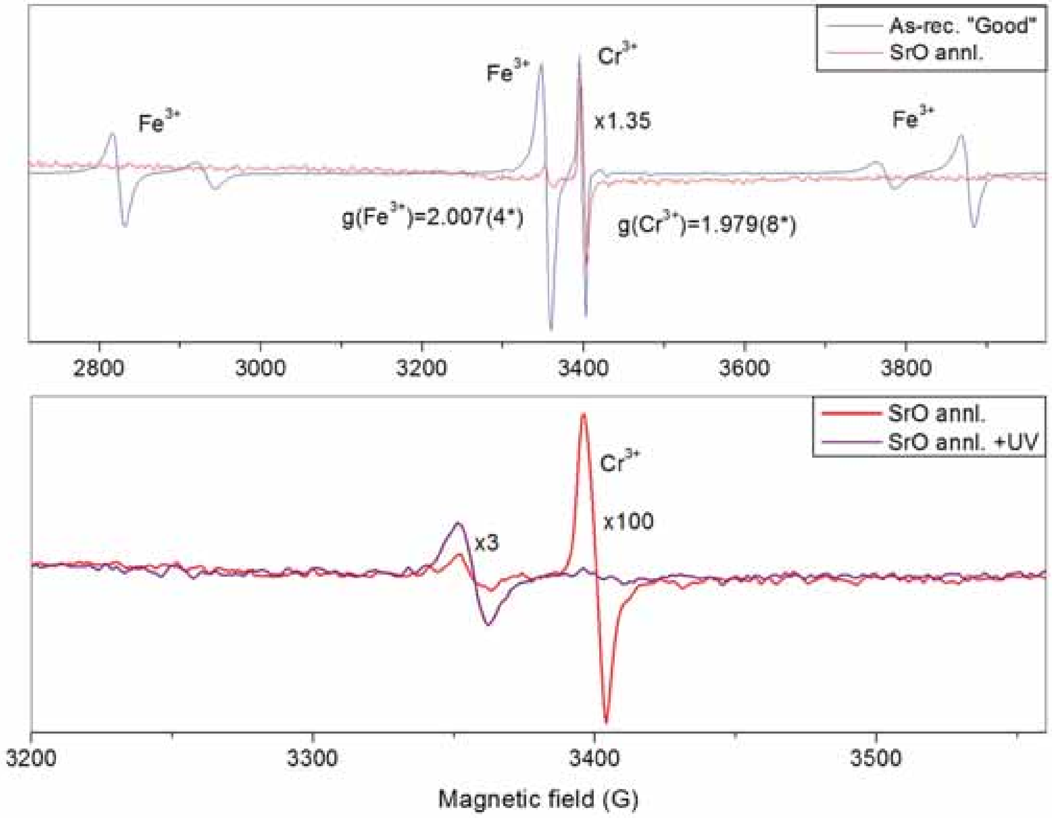

Figure 47: EPR spectra, courtesy of M.E. Zvanut. EPR changes during annealing and light exposure. Unknown PPC defect increases while Cr^{3+} decreased. Uncertainty in g value is given in parenthesis. UV is actually a 405 nm LED.

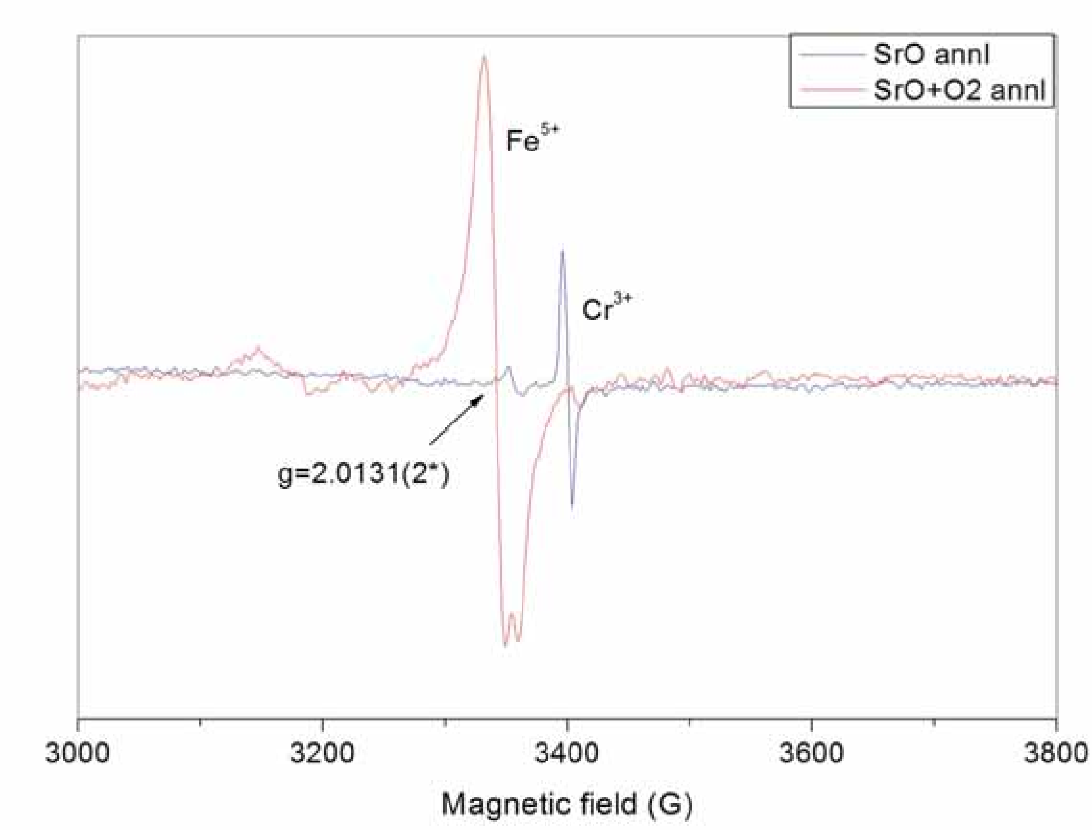

Figure 48: Changes that occur when an SrO annealed sample is then oxygen annealed. Uncertainty in g value is given in parenthesis. The unidentified center with g=2.0131 is see in the SrO annealed sample. EPR spectra, courtesy of M.E. Zvanut.

PPC peak and the unidentified EPR line are similar to the unidentified $X - O^-$ center.

If an SrO annealed sample is later oxygen annealed at 800°C for 1 hour, the Cr^{3+} line disappears and a Fe^{5+} line appears (Figure 48). This helps to establish that the line of unknown identity, $X - O^-$, is not related to iron in another oxidation state, such as Fe^{5+}. Additionally, Fe^{5+} is lower in the band gap than Fe^{3+} [Morin and Oliver, 1973], and we know oxidation lowers the Fermi level within the band gap [Berney and Cowan, 1981].

EPR measurements were repeated for the special batch G150101 from MTI (Figures 49 and 50). This batch was used in the creation of the *p*-type samples described in Chapter 7. The main difference between batch G150101 and the old samples is the Cr^{3+} and Fe^{3+} have 2 orders of magnitude larger concentrations (Figure 49). In addition, oxygen annealing causes manganese in the 2+ charge state to appear.

With light exposure the Cr^{3+} and Fe^{3+} lines in the special batch decrease by about a factor

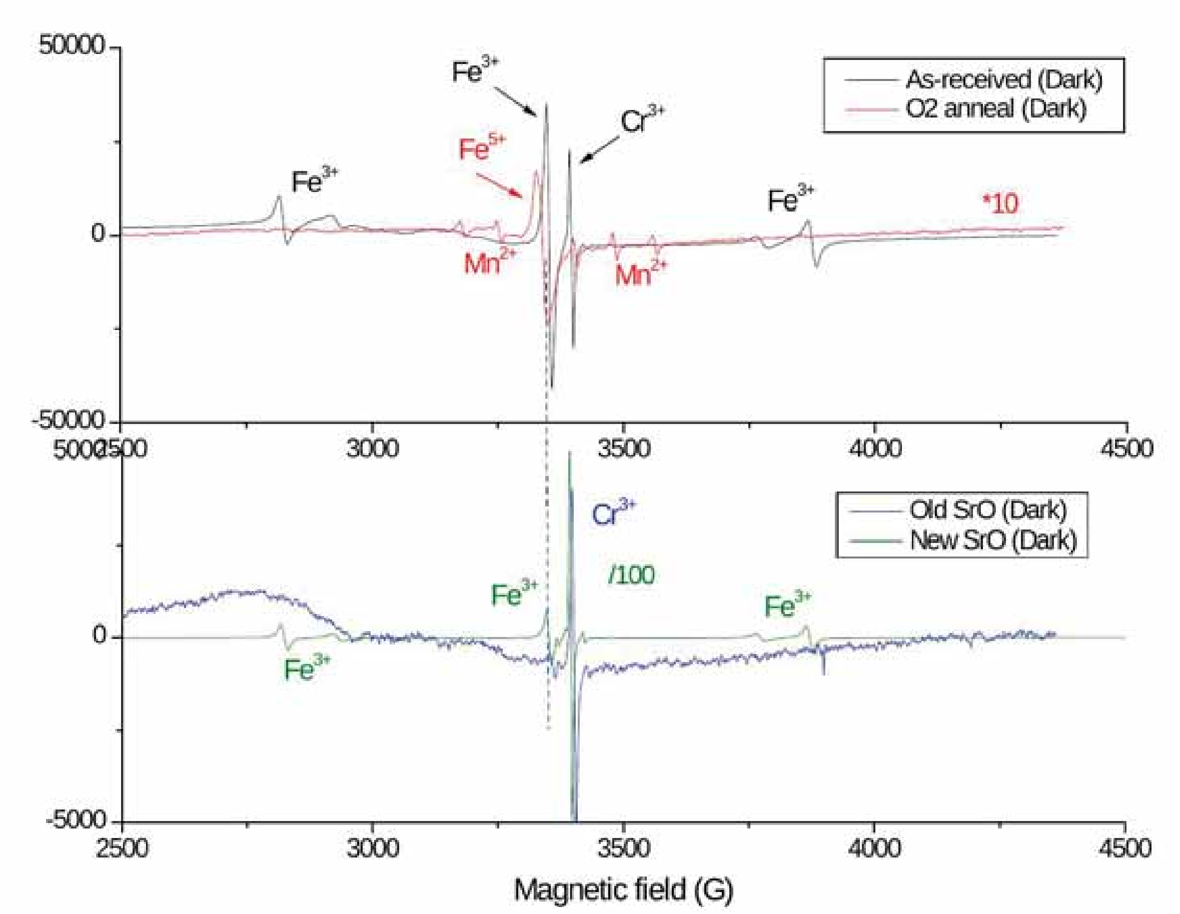

Figure 49: EPR Spectrum, courtesy of M.E. Zvanut. top: Old sample as received and after O_2 anneal. Show to illustrate the position of where Fe^{5+} should be. Bottom: Comparison of EPR spectra of old vs new (Batch G1510101) samples before light exposure and after SrO anneal. The dashed line marks the 'zero crossing' of Fe^{3+}. The main difference is the Cr^{3+} and Fe^{3+} have 2 orders of magnitude larger concentrations.

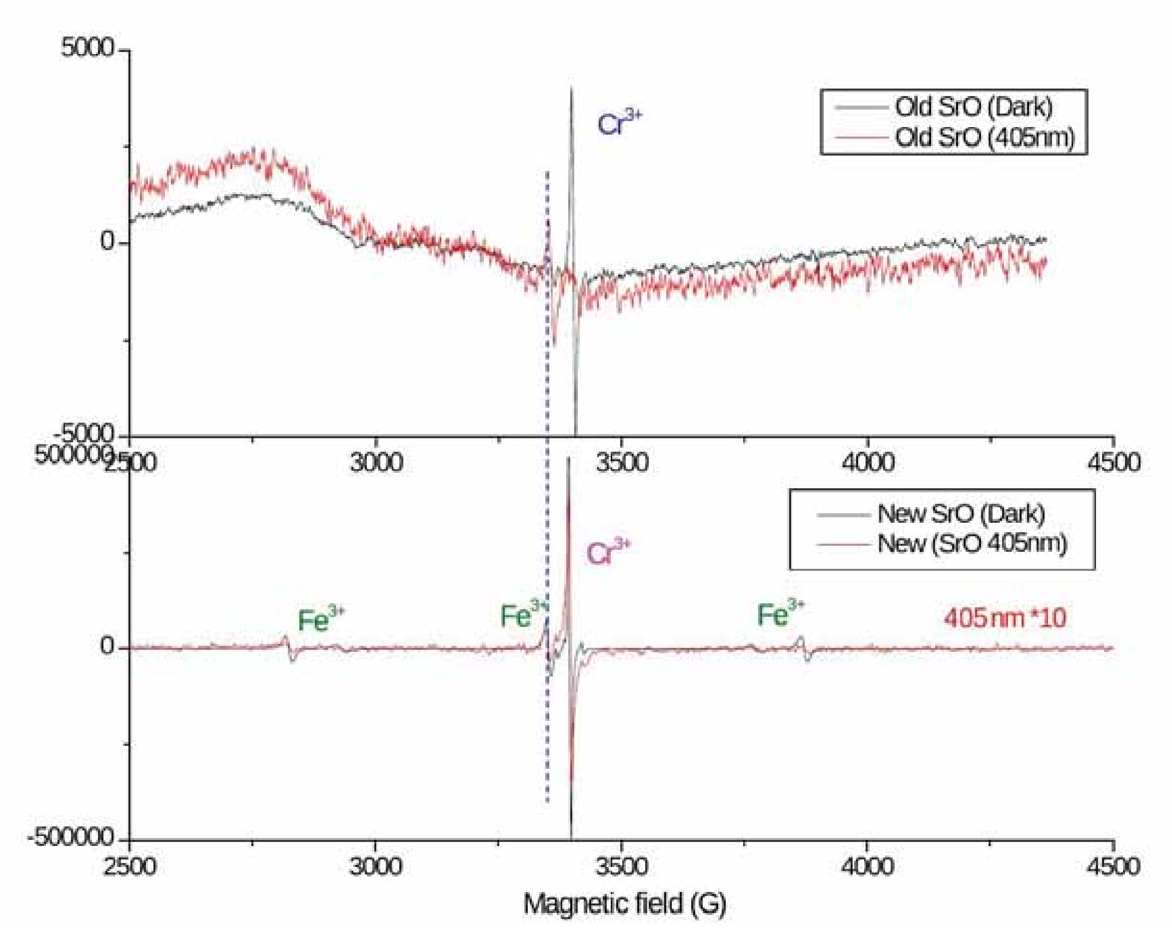

Figure 50: EPR spectra, courtesy of M.E. Zvanut. Comparison of EPR spectra of old vs new samples with light exposure. The dashed line marks the 'zero crossing' of Fe^{3+}. In the new batch, G150101, both Cr^{3+} and Fe^{3+} decrease by about a factor of 10. While previously, the unknown defect increased while Cr^{3+} decreased.

of 10. The behavior of chromium is the same in both samples, despite the 2 orders of magnitude increase in concentration. This may mean that chromium is involved in the mechanism responsible for PPC. There is some other circumstantial evidence to suggest this. Cr^{3+} has a crystal field transition at 2.2 eV which is close to our PPC peak at 2.4 eV. While chromium is present in almost all samples, even undoped, at the ppm level, this explanation was dismissed because the oscillator strength of this peak is too high [Wild et al., 1973].

The behavior of iron is different in the new batch G150101, since we now see its presence after SrO annealing and before light exposure. Examining the UV Vis spectra (Figure 51), shows that the old sample has iron in the 4+ state before light exposure as evidenced by the peak at 430 nm. Because iron is already in the 4+ charge state we do not see it in the 3+ charge state in EPR. Our new batch, G150101, does not have iron in the 4+ state before light exposure (Figures 22 and 12). This means the observed difference in the EPR signal is not due to the higher concentration of iron, but rather the starting charge state of iron.

In conclusion, iron, chromium and manganese ions have been observed in STO samples. As-received samples have Fe^{3+}, Mn^{2+} and Fe^{5+} appear after oxygen annealing. Oxygen annealing will lower the Fermi level, and reduce free electrons from oxygen vacancies, resulting in iron losing electrons, and increasing its charge state. Cr^{3+} is present after SrO annealing and decreases or disappears when the sample is exposed to light. Perhaps, Cr^{3+} decreases as the charge state goes to 4+ upon light exposure, and this is the origin of the mysterious PPC peak at 520 nm. Light exposure reduces or removes the Fe^{3+} line when present. Fe^{3+} is present before light exposure when the 430 nm peak (Fe^{4+}) is not seen in the UV Vis. An unidentified EPR peak at g=2.0131 was seen to increase upon light exposure, when the Fe^{3+} was not seen before light exposure. This line has a very similar g value to the Fe^{3+} line (g=2.007) and may be hidden when the Fe^{3+} line is present. This unidentified center may be the $X - O^{-}$ center seen by Ensign and Stokowski [Ensign and Stokowski, 1973] which has a corresponding optical absorption near our PPC peak at 520 nm. Of the many possibilities they list, a titanium vacancy is the most likely candidate for the identity of this unknown line. The annealing process, which is discussed in Chapter 8, suggests the formation of titanium vacancies is likely.

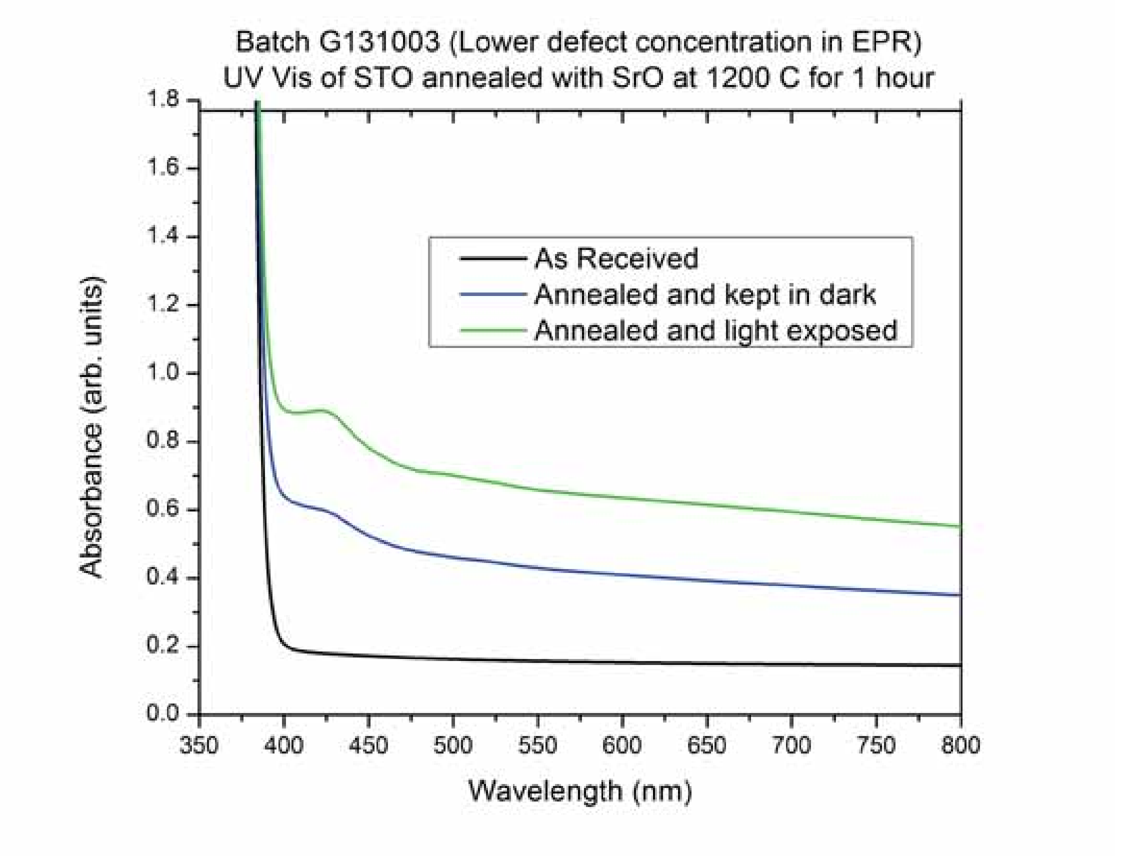

Figure 51: UV Vis spectrum for the old EPR sample with lower concentrations of Cr^{3+} and Fe^{3+}. Notice that the 430 nm peak is present before light exposure.

4.6 Summary

Point defects largely determine the properties of semiconductors. As we have seen, oxygen vacancies are the dominant factor controlling the conductivity of STO. They are also necessary for PPC to occur. Some chips have enough oxygen vacancies as-grown, while others need a light vacuum anneal prior to the SrO anneal for PPC to occur. Too many oxygen vacancies result in the 430 nm peak before light exposure, and the increase in conductivity with PPC being muted.

Hydrogen is another ubiquitous impurity present in STO, and is seen in multiple ways. The H_I line at 3500 cm^1 is due to the O-H dipole, and is often seen in as-grown samples. This line has multiple satellites at higher wavenumbers, which disappear during annealing and return with light exposure. The satellites may be hydrogen complexes with (Fe^{3+} - V_O) or strontium vacancies and hydrogen. Additionally, hydrogen can also be present in the H_{II} lines at 3355 and 3384 cm^{-1}. Its presence here is detrimental to PPC and may be the reason an iron doped chip cannot be made to have PPC.

An unidentified defect has been observed with EPR measurements (g=2.0131) prior to light exposure. Titanium vacancies are a likely suspect and may be connected to our mysterious PPC peak at 520 nm.

Chapter FIVE

ERASING BUT NOT KILLING PPC

There are many applications where being able to write and erase regions of high conductivity on a chip could be useful. To achieve this, a method to undo the effect of light exposure must be found.

Since blue/violet light is used to induce PPC, we investigated whether other colors of light will erase this effect. Transient changes in conductivity have been observed during coloration and bleaching studies of photo-chromic STO [Williams, 1971]. Williams used blue light for the coloration and red light for the bleaching in this study. While photochromism in not same thing as PPC, the color centers involved might be the same.

High intensity LEDs at 660 nm and 640 nm were used as the red light source. A previously exposed sample was placed inside the FTIR with the red light source. A spectrum was taken at room temperature. Then the sample was exposed to red light for 30 minutes and another spectrum was taken, without breaking vacuum. See Figure 52 for the results, which show red light does not erase PPC.

A similar test was done with a high intensity (1 W) green laser (532 nm), where the laser beam traveled through a window outside the FTIR and was directed onto the sample with mirrors. Figure 53 shows that green light is also not an eraser.

While light does not erase PPC, heat treatments will. See Figure 54 for an example where a sample was heated to 500°C for a short duration of 5 min. For the heat erasing treatments, a hot plate was used, where the sample was exposed to the atmosphere for the duration of the heat treatment. The times and temperatures vary, and are indicated where the data are displayed. Approximately the same treatment was used to erase the chip in Figure 55 as in Figure 54, but PPC did not return in Figure 55. Both these chips were from the same batch, but different vacuum treatments were used in the original anneal of the chip. The one that still had PPC return after erasing with the hot plate was treated with a higher vacuum, 10^{-5} mbar, than the one that did not, 10^{-2} mbar. Recall that oxidation and reduction can take place at temperatures as low as 400°C [Faughnan, 1971]. An open air anneal would result in an slight oxidation treatment, and the chip that was treated with a higher vacuum anneal would have more oxygen vacancies to lose.

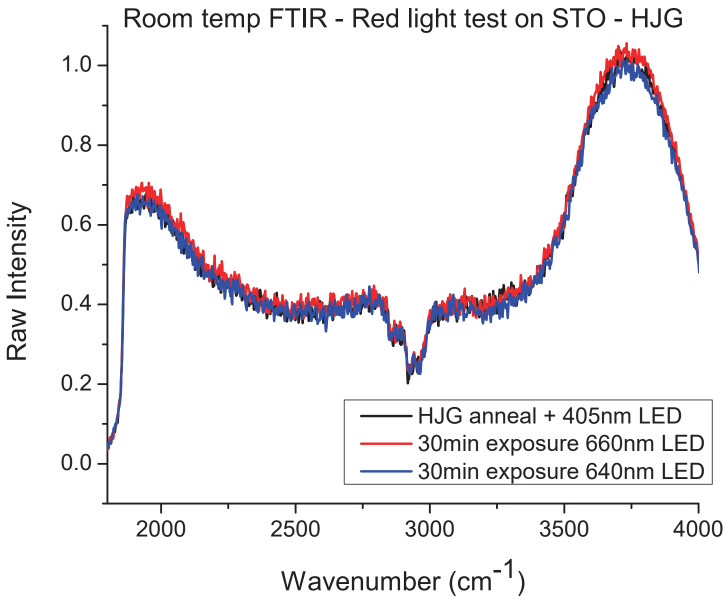

Figure 52: Room temperature FTIR spectrum showing that a previously annealed and light exposed chip does not erase with exposure to red light.

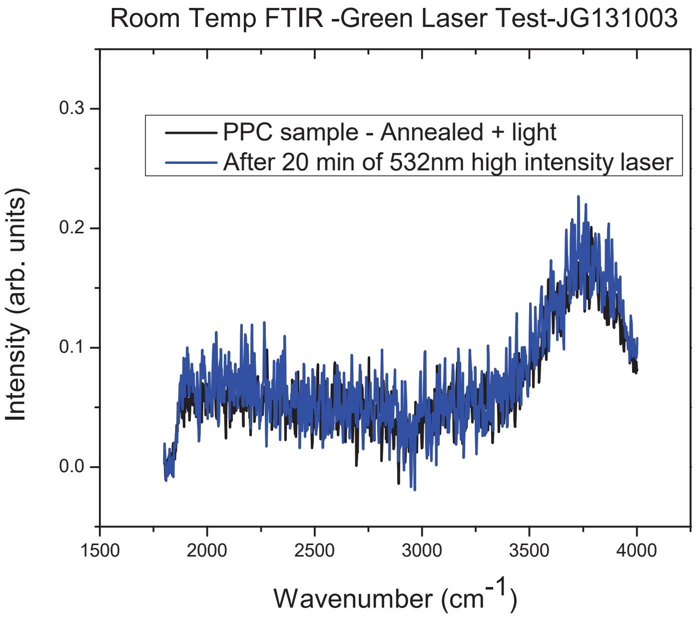

Figure 53: Room temperature FTIR spectrum showing that a previously annealed and light exposed chip does not erase with exposure to a high powered green laser.

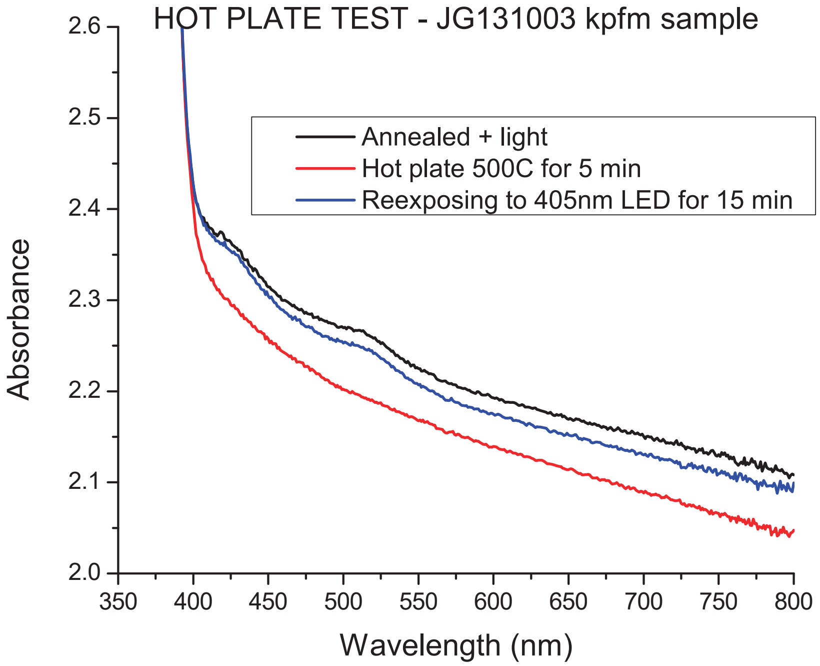

Figure 54: UV Vis spectra showing that a hot plate treatment will erase PPC. Re-exposing to light brings back the PPC peak at 520 nm. Note: this sample was originally vacuum annealed (10^{-5} mbar) then SrO annealed.

This indicates that the temperature used is too high, i.e. it may "kill" PPC.

Heat treatments as low as 200°C conducted for a duration of 30 minutes will begin to erase PPC (Figure 56). This temperature will erase the 520 nm peak and lower the intensity of the 430 nm peak in the UV Vis spectra. Note that in the UV Vis data on this sample the PPC peak at 520 nm is quite weak. This is due to the batch it came from. Every chip from the batch G150101 from MTI has a very weak PPC peak. A hot plate treatment of 225°C for 30 minutes does a better job of erasing the PPC, as seen in Figure 57. It is important to note what happens to the PPC with hot plate treatments, since Hall contacts are usually applied around temperatures of 200 to 225°C.

Performing a series of successive anneals on the same chip can give a better indication of the best temperature to use for erasing a light exposed chip without killing the PPC. Figure 58 shows FTIR spectra for a series of successive heat treatments that were done on the hot plate starting at 300°C. All treatments were done for a duration of 30 minutes in the dark. The raw intensity

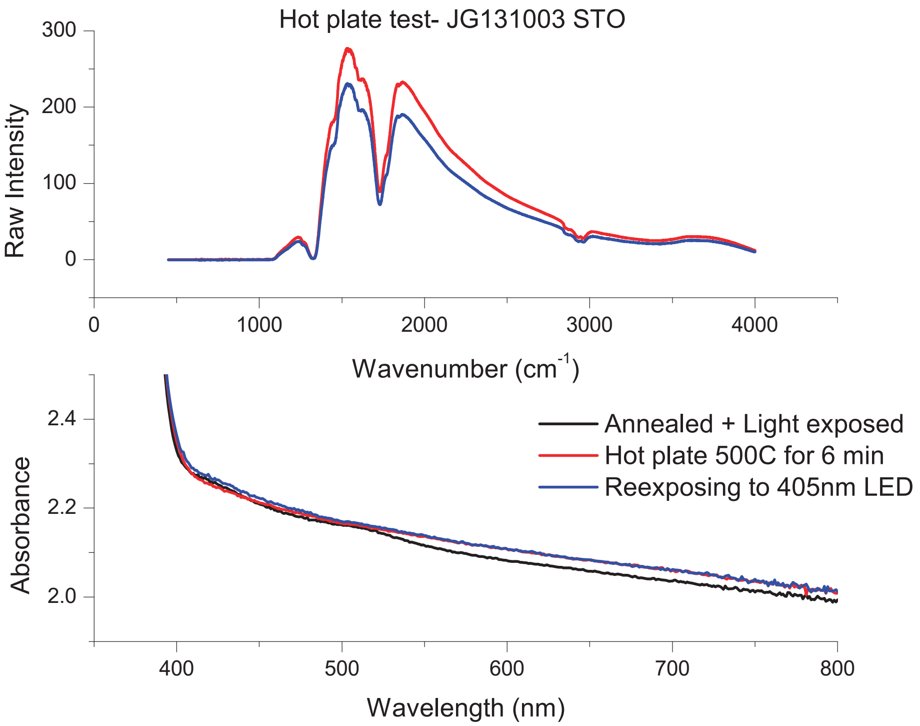

Figure 55: UV Vis and room temperature FTIR spectra of a sample that was hot plate treated. Re-exposing to light failed to bring back PPC. Note this sample is from the same batch as Figure 54 but the vacuum annealing step was done at 10^{-2} mbar.

returns to the same level in both the 300°C and 400°C hot plate treatments, while a treatment of 450°C does not. Higher temperatures cause the loss of oxygen vacancies, which are needed for PPC, as shown in Chapter 4.1. This is in agreement with the fact that oxygen vacancies become mobile above 400°C. The optimal temperature for erasure is around 300°C, which is low enough to be well below the oxygen vacancy mobility limit, and high enough to erase a chip in a short time.

The 200 and 225°C hot plate treatments did not fully erase the iron 4+ peak around 430 nm, although its intensity was reduced, consistent with the literature [Lebedeva et al., 1988]. Treatments of 300°C do fully erase the 430 nm peak (Figure 59). The presence of this peak depends on electrons frozen into a non-equilibruim state. Higher temperatures free the trapped electrons.

Recall from Chapter 4.3 how the hydrogen line and satellites behaved during annealing and light exposure in PPC samples (Figure 37). SrO annealing removed any satellite lines that were present in the as-received chips and decreased the intensity of the main H_I line. Light exposure

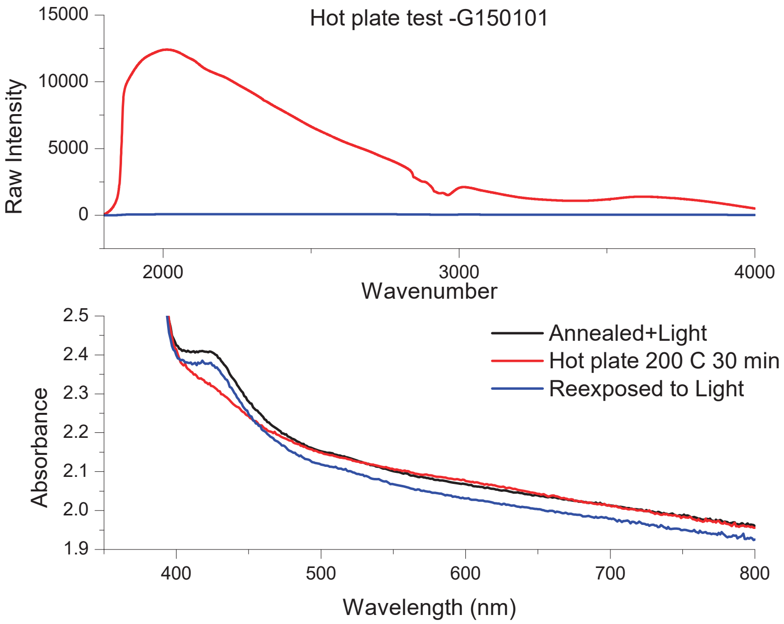

Figure 56: Hot plate treatment at 200°C for 30 minutes just barely erases the PPC. This batch G150101 from MTI has a very small PPC peak, yet it still has the same orders of magnitude increase in conductivity.

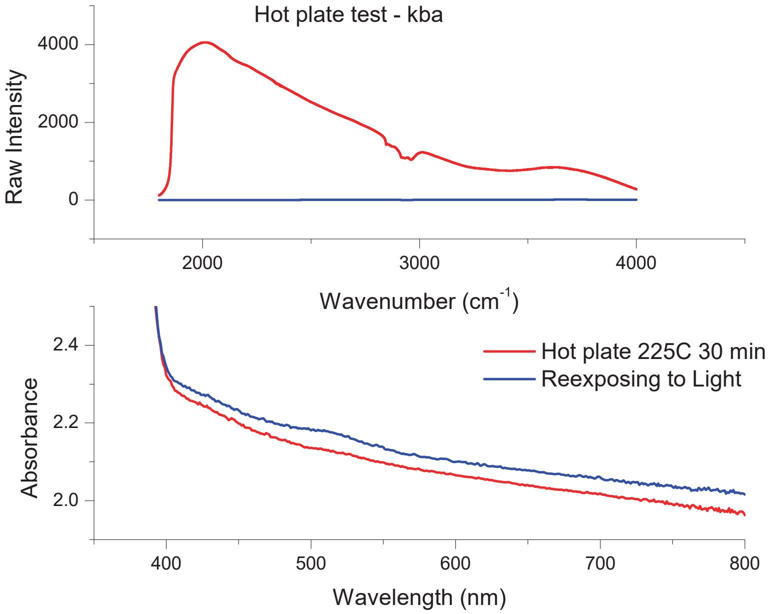

Figure 57: UV Vis and FTIR Spectra showing that a hot plate treatment of 225°C for 30 minutes will erase the 520 nm peak present during PPC. In this sample the iron peak at 430 nm is weak.

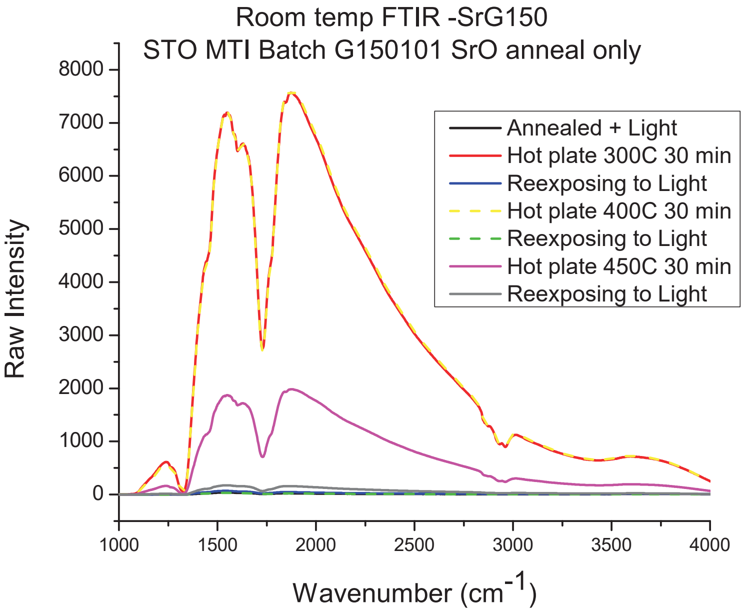

Figure 58: Room temperature FTIR spectra showing a series of successive hot plate treatments starting at 300°C and ending at 450°C. All treatments were done for a duration of 30 minutes in the dark. Notice that 450°C results in the PPC only partially returning with light exposure.

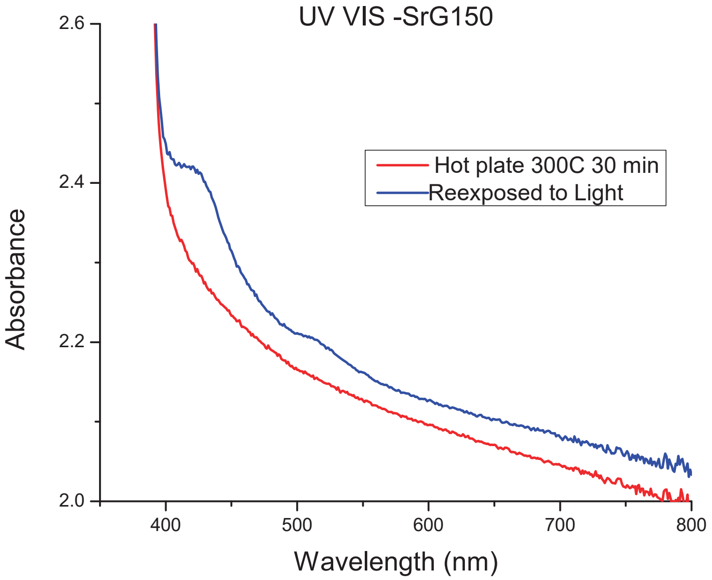

Figure 59: UV Vis spectra for the 300°C hot plate treatment mentioned in Figure 58.

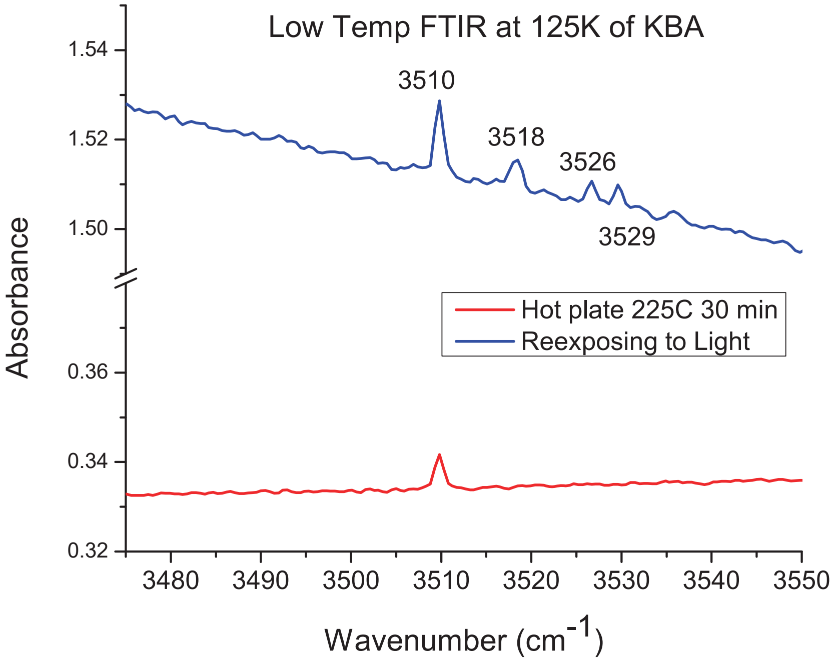

Figure 60: Low temperature FTIR spectra showing the behavior of the main hydrogen line and satellites during hot plate erasure. Satellites disappear after hot plate and reappear with additional light exposure.

resulted in the satellite lines reappearing and a slight increase in the main line. Figures 60 and 61 show that a hot plate treatment removes the side bands, while re-exposing to light makes them return. This confirms that a hot plate treatment as low as 200°C returns the sample to the same condition it was in after the original annealing. The appearance or disappearance of the hydrogen satellite lines near 3500 cm^{-1} and the peak at 520 nm coincide.

To summarize, light cannot be used as an eraser, but heat treatments can. A open air anneal conducted at 300°C for a short duration of $\sim$ 30 minutes is optimal for erasing PPC, since both peaks disappear at this temperature. Heat enables metastable trapped electrons to have enough energy to overcome the thermal barrier and leave the conduction band. Higher temperatures can lead to the loss of too many oxygen vacancies and will permanently erase the chip, since they are needed for PPC.

The PPC defect at 520 nm, the H_I satellite lines, and the absorption due to free carrier in the IR all disappear at 200°C. This temperature is sufficient to return the electrons from the

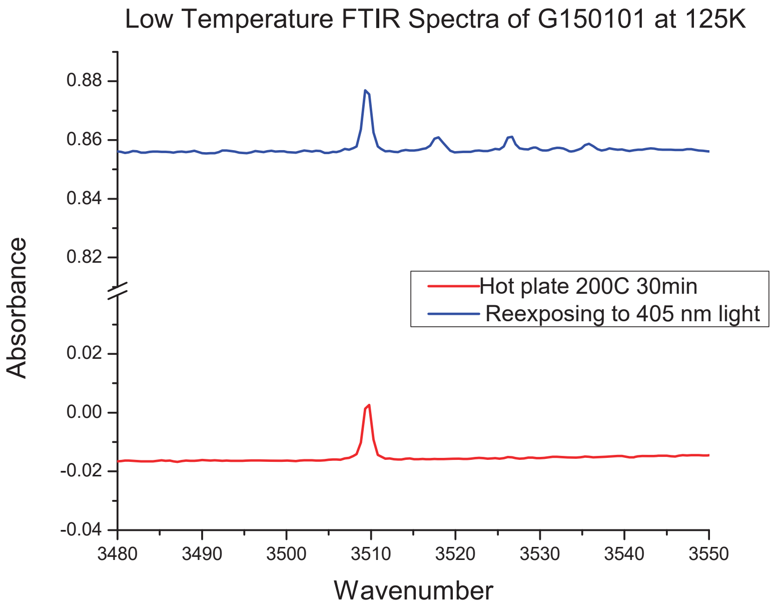

Figure 61: Low temperature FTIR showing that a hot plate at 200°C will erase the satellite lines, returning the chip to a pre-light exposed state.

conduction band to the PPC acceptor level. This shows the behavior of the"PPC peak" at 520 nm and the H_I satellite lines above 3500 cm^{-1} are linked, and not related to iron since the iron 4+ peak is still present at this temperature.

The iron 4+ peak disappears at 300°C, which correspond to the trapped electrons in the iron oxygen vacancy complexes emptying out and returning to the iron 3+ state (See Section 4.4). The changes in conductivity and its relation to the presence of the 430 nm peak are detailed in Section 6.3.

Chapter SIX

ELECTRICAL MEASUREMENTS

The electrical properties of semiconductors are crucial to their use in electronic devices. For instance, one needs to know the resistance of the material, so that current can be chosen for the device to operate at the desired voltage. Conductivity and mobility measurements are also useful in determining the net doping concentration. Knowing the carrier type, electrons or holes, is also necessary to form basic semiconductor circuit elements, such as a $p - n$ junction.

6.1 Hall Measurements

Good contacts are the key to electrical measurements. Indium forms ohmic contacts with n-type STO, of varying degrees of reduction [Carnes and Goodman, 1967, Perluzzo and Destry, 1978, Tufte and Chapman, 1967]. This is why we chose to use melted or occasionally pressed indium to form contacts for the samples measured in this section. Most of our p-type samples are discussed in Chapter 7.

As-received samples have a resistance around 10^9 Ω from linearity check measurements. The samples were too resistive to get reliable Hall measurements with our setup at room temperature. Vacuum annealed samples have resistivities on the order of 1-1000 Ω cm depending on the level of vacuum used.

The change in electrical properties that accompanies PPC is quite dramatic. Table 6.1 shows the change in resistivity, density, and mobility values that accompanies PPC when the 430 nm peak is not present before light exposure. Here the resistivity decreases by 4 orders of magnitude, and the density of charge carriers increases by 3 orders of magnitude. The mobility also increases upon light exposure. Electron mobilities in STO at room temperature are often quite low [Verma et al., 2014, Parker and Yahia, 1968], even in samples with high carrier density from oxygen vacancies. A higher density of free carriers may screen ionized impurities, reducing scattering and increasing the mobility slightly.

A different sample, with the 430 nm peak present before light exposure, was examined. As

Table 6.1: Hall effect measurements before and after light

Exposure status	Resistivity (Ω cm)	Mobility (cm^2/Vs)	Density (cm^{-3})	Carrier Type
Before light	(1.77 ± 0.01) x 10^4	0.72 ± 0.12	(4.98 ± 0.88) x 10^{14}	Electrons
After light	(2.82 ± 0.02)	5.77 ± 0.03	(3.84 ± 0.02) x 10^{17}	Electrons

the temperature is decreased, the mobility of the charge carriers increases dramatically (Figure 62). This follows the general trend observed in the literature [Frederikse and Hosler, 1967, Perluzzo and Destry, 1978, Verma et al., 2014]. The increase in mobility as temperature decreases is due to phonon scattering. At lower temperatures there are fewer phonons around to scatter the electrons. Parker [Parker and Yahia, 1968] has shown $\ln \mu$ vs T^{-1} independent of the degree of reduction, or oxygen vacancy concentration, with the slope of the straight line being 0.06 eV. We find that for temperatures above $\sim$ 180 K the log of mobility vs 1000 / T is approximately linear. Below this temperature the curve turns downward, which is also seen in the literature [Tufte and Chapman, 1967]. Parker only went down to 200 K, so our results are similar for the same temperature range measured. If we do a linear fit of only the points between room temperature and 200 K we get a slope of 0.73. This works out to be 0.07 eV, which is slightly higher that the value reprinted in the literature [Tufte and Chapman, 1967, Parker and Yahia, 1968].

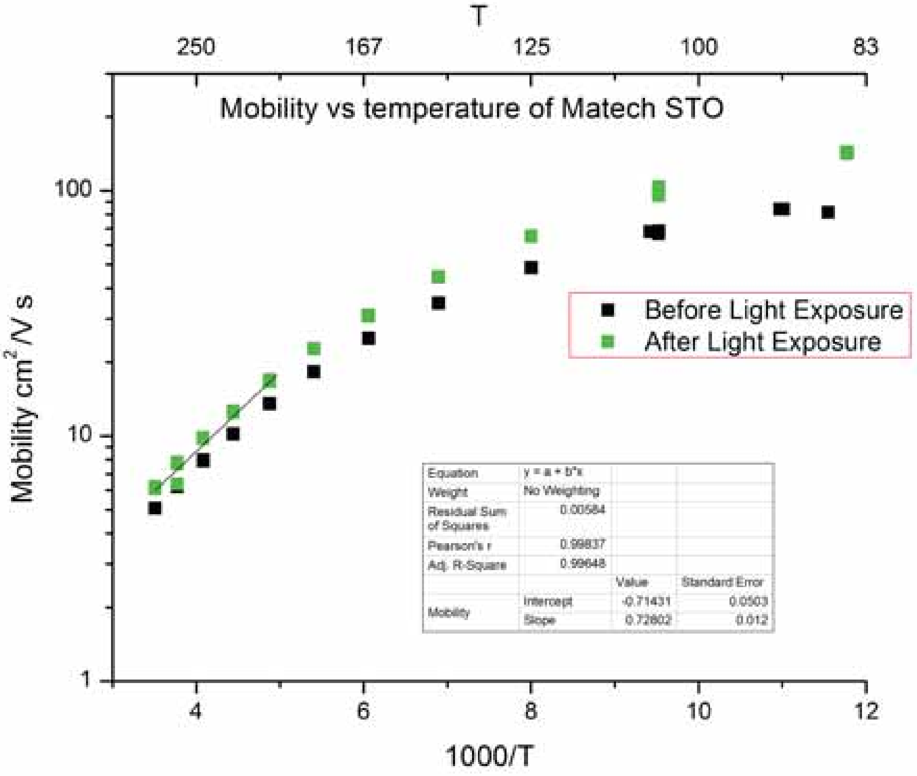

Equation	y = a + b*x		
Weight	No Weighting		
Residual Sum of Squares	0.00584		
Pearson's r	0.99837		
Adj. R-Square	0.99648		
		Value	Standard Error
Mobility	Intercept	-0.71431	0.0503
	Slope	0.72802	0.012

Figure 62: The changes in mobility with temperature for SrO annealed STO.

6.2 Oxygen-annealed Samples

Performing an oxygen anneal at 1200°C for one hour on an as-received chip results in a chip that is too resistive to measure at room temperature. A resistivity of $\sim 1 \times 10^{10}$ Ω cm was measured at 360 K with mixed conduction type. A charge carrier density of 8 x 10^7 cm^{-3} with a mobility on the order of 1 cm^2/Vs was also measured.

Performing an oxygen anneal at 800°C on a sample that was previously SrO annealed again results in a very resistive sample. Hall measurements could only be performed at elevated temperatures, and we are still close to the limit of the machine (Table 6.2). The sample has very few charge carriers after oxygen annealing. This is not unexpected, since oxygen annealing will remove oxygen vacancies, which contribute greatly to the free electrons present in the crystal. High partial pressures of oxygen can cause the chip to be *p*-type [Menesklou et al., 1999], which we see at the higher temperature. A mixture of holes and electrons is present at lower temperatures. As the sample heats up electrons may be removed from the conduction band, leaving just holes. This agrees with our ability to erase a chip, and hence lower its free electron concentration, with heat as discussed in Chapter 5. Its also possible that the electron conduction comes from a surface state and the holes from the bulk, and a deep acceptor level will have increased hole concentration as the sample heats up. No change was observed after exposing to 405 nm light, which makes sense because we removed the oxygen vacancies that are needed for PPC.

Table 6.2: High temperature Hall effect measurements an STO sample annealed in SrO followed by oxygen.

Temperature K	Resistivity (Ω cm)	Mobility (cm^2/Vs)	Density (cm^{-3})	Carrier Type
375	$(7.44 \pm 0.08) \times 10^8$	7.5 ± 1.9	$(1.17 \pm 0.32) \times 10^8$	Mixed
400	$(2.20 \pm 0.25) \times 10^8$	1203 ± 389	$(4.08 \pm 4.17) \times 10^7$	Holes

6.3 Correlation with 430 nm Peak

Let us return to a topic we discussed in Chapters 4, whether the 430 nm peak is present before light exposure or not. Table 6.3 shows that samples that have the peak before light exposure have a lower resistance to start with than those that do not have this peak. A change in resistance or carrier density is still observed, just less so for samples that have this peak present before light exposure. Instead of the 3-4 orders of magnitude change, we see about 1-2 orders, when the 430 nm peak is present. For the largest change in conductivity to occur with light exposure, having the 430 nm not present before light exposure is best. These same arguments apply to not having the iron peak present after erasing.

In Table 6.3 the values of resistance are given in Ω from the linearity check that is performed prior to Hall effect measurements. This value was chosen since Hall effect measurements could not be performed successfully on all samples. Those samples often had bad measurements, characterized by negative resistivities. This can be caused by bad contacts or inhomogeneities within the sample. The density of electrons is given when Hall measurements were successful. Additionally, contacts were removed before the sample was exposed to light and then reapplied for the after light measurements, since the contacts could block a region of the chip, and non uniform exposure will lead to surface inhomogeneities that could prevent good Hall effect measurements.

While not all measurements were taken for each sample, we can still observe the smaller change in carrier concentration for samples with this peak present prior to light exposure. In conclusion, for the most dramatic change in the electrical properties with PPC, it is desired to not have the 430 nm peak present before light exposure (or after erasure). Iron in the 4+ charge is correlated with more free electrons in the conduction band. When some free carriers are already present, the increase in free carriers from PPC with light exposure results in less of a change.

Table 6.3: Hall effect measurements at room temperature and the presence of the peak at 430 nm. Resistances are from linearity check measurements and are given in Ω, while carrier density is from Hall effect and given in cm^{-3}.

Sample Name	430 nm peak before light	Before light: Resistance	Density	After light: Resistance	Density
KBA	yes	6×10^3	-	5×10^2	-
Matech	yes	1.0×10^4	10^{16}	10^3	10^{17}
JG131M	yes	6×10^3	-	1×10^1	-
HBA	no	6.0×10^5	5×10^{14}	5×10^2	3×10^{17}
Tarun[Tarun et al., 2013]	no	-	5×10^{15}	-	2×10^{18}
T8V	no	10^9	10^{10}	10^4	10^{14}

6.4 Surface Layers

In the literature, there is evidence of a surface layer different from that of the bulk, with rather complex behavior. Oxygen vacancies have been known to form a conductive layer on the surface and contribute to downward band bending [Takeyasu et al., 2013]. From atomic force microscopy (AFM), drastic differences in the surface morphology have been observed for oxidized and reduced crystals compared to the original stoichiometric surfaces [Szot and Speier, 1999]. AFM and secondary ion mass spectrometry (SIMS) show the growth of surface features (droplet and even triangular crystallites) after oxygen anneal and rapid cooling [Szot et al., 2000]. AFM measurements will be discussed in Appendix B: KPFM results.

Some of the surface phenomena may be related to the formation of non-perovskite phases, such as layers of SrO. Additionally, Ruddlesden-Popper phases can accommodate excess SrO into the structure between the $\mathrm{SrTiO_3}$ perovskite blocks, forming a homologous series $n\mathrm{SrTiO_3}\cdot\mathrm{SrO}$ [Balachandran and Eror, 1982, Ruddlesden and Popper, 1958].

Experimentally, a difference between the surface before and after sanding has been observed. For instance, in a lightly vacuum annealed sample with indium contacts the resistance value from

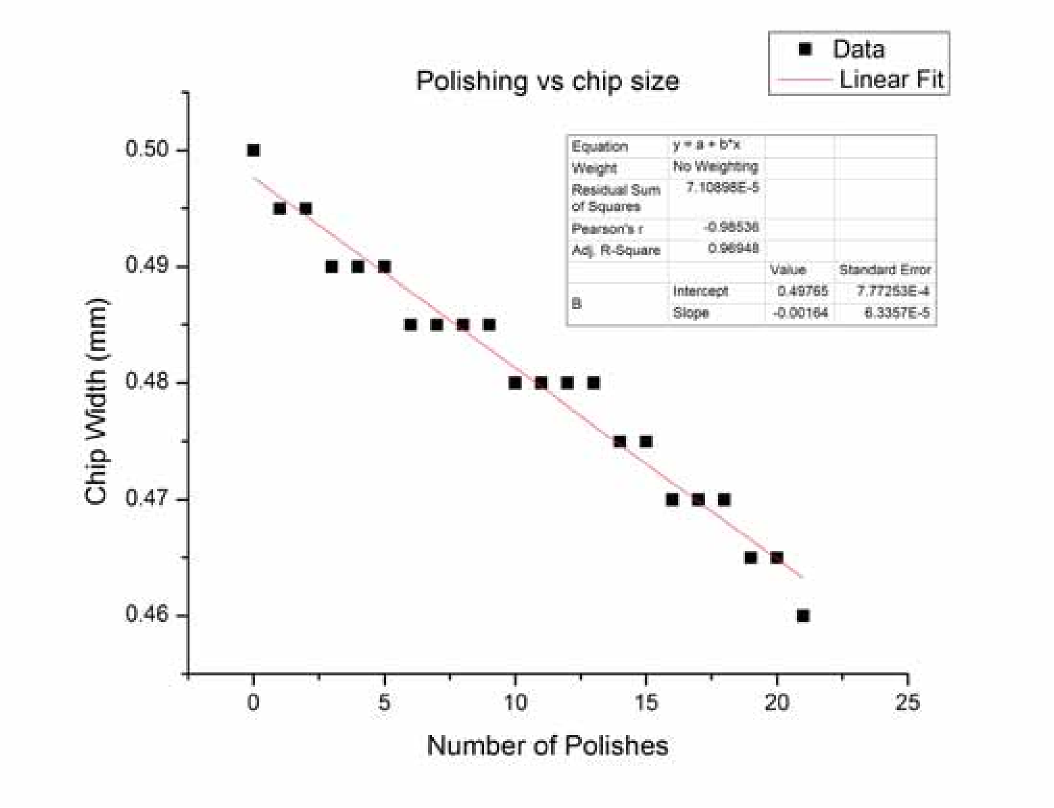

Equation	y = a + b*x		
Weight	No Weighting		
Residual Sum of Squares	7.10898E-5		
Pearson's r	-0.98536		
Adj. R-Square	0.96948		
		Value	Standard Error
B	Intercept	0.49765	7.77253E-4
	Slope	-0.00164	6.3357E-5

Figure 63: Amount of surface removed by polishing with 220 grit sandpaper.

linearity check was 2.2 x 10^3 Ω. (Note that linearity check values include the contact resistance and are therefore not directly comparable to the resitivity value given by Hall measurements.) Contacts were then removed and the chip was sanded, which removes ~ 1 μm of material (Figure 63). Contacts were then reapplied, and the resistance value is now 2.5 x 10^4 Ω. Sanding the surface increases resistance by about an order of magnitude.

This phenomenon of a sanded chip having an order of magnitude higher resistance has been noticed in many other types of samples. TiO_2 and SrO annealed samples show this as well. Additionally, continuing to sand the surface does not increase the resistivity more. This indicates a thin surface layer that is different from the bulk. Sanded samples still exhibit PPC [Tarun et al., 2013], so this surface layer is not related to the bulk defects involved in PPC.

6.5 Summary

Hall measurements show as-received chips are very resistive. This is typical for wide band gap semiconductors. Oxygen annealing further increases the resistance, while vacuum annealing decreases the resistance dramatically. This is consistent with oxygen vacancies being the dominant factor controlling the conductivity. STO's mobility increases dramatically as the temperature decreases due to phonon scattering. This pattern is still observed in chips with PPC, both before and after light exposure.

Measurements show a dramatic change in electrical properties during PPC. The decrease in resistance is largest when the 430 nm peak is not present before light exposure. A high temperature (800°C) oxygen anneal will kill PPC, demonstrating oxygen vacancies are crucial for PPC.

Additionally, surface layers are observed in a wide variety of samples. Removing ~ 1 micron of material results in an order of magnitude increase in the resistance for a wide variety of samples. This surface phenomenon, while interesting, is not responsible for PPC.

CHAPTER SEVEN

P-TYPE STO

Weakly p-type STO has been observed in STO, after two specific types of treatments. In both circumstances they are very resistive, and only occur after heat erasure to remove electrons from the conduction band. One situation that results in this behavior is after SrO treatments and hot plate erasure at 300°C [Poole et al., 2015a, Poole and McCluskey, 2016]. The other can occur after a TiO_2 treatment and then erasure at $\sim$ 600°C described in Chapter 8.

As previously published[1,2]:

To create the defects that give rise to PPC, crystals are sealed in an evacuated ampoule, along with SrO powder, and annealed at 1200°C. From positron annihilation measurements, these defects were tentatively assigned to titanium vacancy - oxygen vacancy ($V_{\mathrm{Ti}} - V_{\mathrm{O}}$) pairs, which act as deep acceptors [Tarun et al., 2013]. Subsequent work showed that annealing in vacuum prior to the 'SrO anneal' yields optimal PPC behavior [Poole et al., 2015b]. This finding is consistent with the $V_{\mathrm{Ti}} - V_{\mathrm{O}}$ model, since the vacuum anneal introduces oxygen vacancies [Meyer et al., 2003]. In this Chapter, we report p-type conductivity, presumably from the same acceptors that give rise to PPC.

Single crystals of STO,[3] 10 x 10 x 0.5 mm, were annealed in a three-step process. The first step was a vacuum anneal at 800°C for 1 hr in a silica ampoule that was sealed with a hydrogen-oxygen torch. The pressure at room temperature in the ampoule, prior to sealing, was 50-100 mTorr. The sample space had a diameter of 1.6 cm and a length of 7.6 cm. After the vacuum anneal, the ampoule was allowed to cool in the open air. It took about 5 min to reach room temperature, which is rapid enough to freeze in oxygen vacancies [Blazey and Weibel, 1984]. (The vacuum anneal was skipped for one sample, BGP.)

The second annealing step was an SrO anneal. SrO powder (0.5 g) was placed into an ampoule with the STO sample and sealed. The pressure was 50-100 mTorr at room temperature, prior to

---

[1] V. M. Poole, C. D. Corolewski and M. D. McCluskey. P-type conductivity in annealed strontium titanate. *AIP Adv.,* 5(12):127217, 2015.

[2] V. M. Poole, M. D. McCluskey. Large persistent photoconductivity in strontium titanate single crystals. *Proc. SPIE 9749,* Oxide-based Materials and Devices VII, 97490N (February 27, 2016): doi:10.1117/12.2207714

[3] Vernuil-grown, MTI batch G150101, manufactured in Japan

sealing. The sealed ampoule was then annealed at 1200°C for 90 minutes. As with the vacuum anneal, the ampoule cooled in the open air. Because the SrO anneal causes PPC, however, the cooling took place in the dark. All subsequent steps were performed in the dark or under red/yellow illumination, which does not induce PPC.

The third step, crucial for p-type conductivity, was an open-air anneal at 300°C. The sample was placed on a glass slide on a hot plate and annealed for 30 min. The sample was taken off the hot glass slide and placed on a room-temperature slide to cool. This annealing step removes excess free electrons, which are excited into the conduction band by thermal treatments or unintentional light exposure [McCluskey and Tarun, 2014]. Without this step, the sample will be lightly n-type [Poole et al., 2015b].

Prior work showed exposure to light ($>$ 2.9 eV) increased the free-electron density from 5 x 10^{15} to 2 x 10^{18} cm^{-3}, with essentially no decay at room temperature over several days [Tarun et al., 2013]. This effect was attributed to excitation of an electron from an acceptor to the conduction band. In the present work, we used an open-air anneal to remove metastable electrons from the sample prior to illumination. This revealed *p*-type conductivity, consistent with the acceptor model.

The sample was polished by hand with fine grit (220) sandpaper for 1-2 min, which removes ~ 1 μm of material. We tried two different contacts, melted indium (In) and rhenium dioxide (ReO_2). In contacts were melted onto the sample with a hot plate at 200°C (Table 7.1). The sample was transferred to a room-temperature slide to cool, and silver paint was used to attach copper wires.

Hall-effect measurements were conducted in the Van der Pauw geometry at room temperature using a DC system (H-50, MMR Technologies) with a magnetic field of 1.2 T. To minimize electrical transient signals, a 90 s delay was taken after each current-voltage reading. A complete Hall-effect measurement took 25-30 min. All data were acquired within 30 hr of applying the contacts.

After performing Hall measurements, the sample was re-polished and ReO_2 contacts were applied. ReO_2 has a high work function [Baikie et al., 2000], making it a suitable choice for *p*-type STO. The ReO_2 particles were mixed in a solution of ethylene glycol and sonicated for 5 minutes. The STO sample was placed on the hot plate on a glass slide and kept at a temperature of 225°C.

Table 7.1: Results of room temperature Hall effect measurements on annealed STO samples with indium contacts

Sample	Current (A)	No. of Points	Mobility (cm^2/Vs)	Density (cm^{-3})	Resistivity (Ω cm)
BVR	5.0×10^{-10}	7	2.9 ± 0.9	$(1.0 \pm 0.3) \times 10^{11}$	$(2.35 \pm 0.01) \times 10^{+7}$
T8V	5.0×10^{-10}	5	2.5 ± 0.8	$(1.1 \pm 0.3) \times 10^{11}$	$(2.3 \pm 1.8) \times 10^{+7}$

The ReO_2 solution was dropped onto the corners of the sample with a needle. When the first drop evaporated, another drop was placed on top. This was done ~ 6 times (5-15 min), until a visibly thick layer of ReO_2 formed. Copper wires were attached to the contacts with silver paint.

Three different samples were studied with the two different contacts: ReO_2 and In. As shown in Table 7.2 and 7.1, the data indicate *p*-type conductivity for all three samples and both contact types. The In contacts result in a much lower hole mobility. It is possible that there are more electrons than holes, but the higher hole mobility leads to a positive Hall coefficient. The hole densities listed are derived from the Hall coefficient via $p = 1/|e|R_H$. For sample T8V, multiple Hall measurements were performed with different currents. The current used for the measurements did not appear to change the results significantly. Figure 64 shows a plot of the Hall coefficient R_H as a function of measurement number. For all 60 measurements, R_H was positive, indicating *p*-type conductivity.

As a repeatability check, after the Hall measurements, sample BVR was polished and contacts were reapplied. The Hall data obtained for this sample, BVR*, are similar to those for BVR. Sample BGP, which did not undergo the vacuum anneal, is more resistive and shows a lower hole mobility than the other samples. This suggests that the vacuum anneal, which optimizes PPC, also optimizes *p*-type behavior. To confirm that the *p*-type conductivity is due to annealing, an as-received sample was polished and ReO_2 contacts were applied. Two-point measurements of this sample showed very high resistance ($> 10^{10}\ \Omega$) such that Van der Pauw measurements could not be performed.

For samples that included the vacuum anneal, room-temperature hole mobilities ranged from 200-500 cm^2/Vs (Table 7.2). These values are much larger than room-temperature electron mo-

Table 7.2: Results of room temperature Hall effect measurements on annealed STO samples with ReO_2 contacts.

Sample	Current (A)	No. of Points	Mobility (cm^2/Vs)	Density (cm^{-3})	Resistivity (Ω cm)
T8V	1.0×10^{-9}	20	175 ± 48	$(1.2 \pm 0.2) \times 10^{+10}$	$(3.2 \pm 1.2) \times 10^{+6}$
T8V	3.0×10^{-10}	20	216 ± 69	$(9.3 \pm 2.1) \times 10^{+9}$	$(3.3 \pm 1.3) \times 10^{+6}$
T8V	1.0×10^{-10}	20	256 ± 90	$(8.9 \pm 4.3) \times 10^{+9}$	$(3.2 \pm 1.2) \times 10^{+6}$
BVR	1.0×10^{-10}	10	457 ± 79	$(4.2 \pm 0.7) \times 10^{+9}$	$(4.8 \pm 3.3) \times 10^{+6}$
BVR*	1.0×10^{-10}	2	380 ± 69	$(6.8 \pm 1.0) \times 10^{+9}$	$(2.4 \pm 1.5) \times 10^{+6}$
BGP	1.0×10^{-10}	23	23 ± 5	$(2.0 \pm 0.4) \times 10^{+9}$	$(1.4 \pm 0.2) \times 10^{+8}$

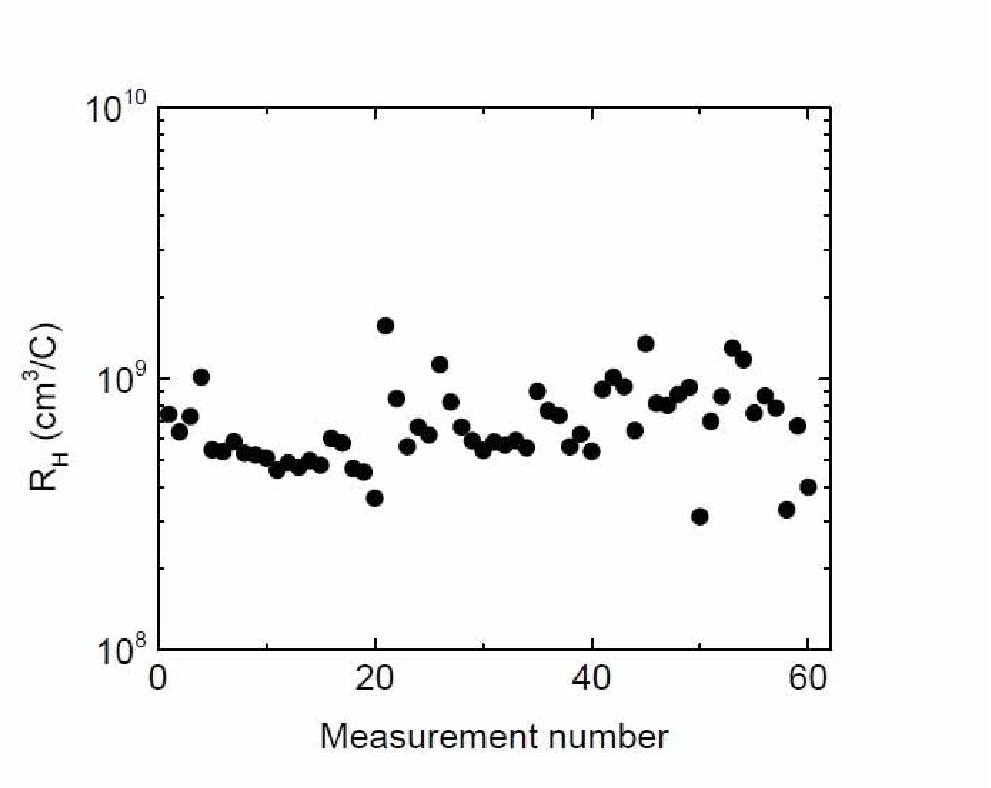

Figure 64: Hall coefficient (R_H) as a function of measurement number for samples T8V.

bilities, 5-10 cm^2/Vs [Poole et al., 2015b, Frederikse and Hosler, 1967]. Above 100 K, optical phonon scattering is the primary process limiting electron mobility [Frederikse and Hosler, 1967, Tufte and Chapman, 1967, Verma et al., 2014, Himmetoglu et al., 2014]. Our results suggest that holes experience less phonon scattering than electrons, resulting in higher mobilities. The range of mobilities may result from different levels of ionized impurity scattering. In addition, if there are metastable electrons in the conduction band, they may contribute to the conduction and reduce the average mobility determined by the Hall effect [McCluskey and Haller, 2012]. The hole densities are very low (10^9-10^{10} cm^{-3}), consistent with a deep acceptor level and/or heavy compensation by donors. However, these are average densities. If the holes are confined to a near-surface layer, then the density in that layer is higher than the average density for the entire sample.

In the 1990s, some researchers claimed that Sc acceptors may produce *p*-type STO. Bulk crystals doped with Sc showed high resistivity (10^7-10^8 Ω cm) near room temperature, but Hall-effect measurements were not performed [Sata et al., 1996]. Photoemission spectroscopy indicated that the Fermi level was ~ 0.7 eV below the conduction band minimum [Higuchi et al., 1998]. This indicates *n*-type conductivity, at least near the surface. More recently, STO:In thin films have also been discussed [Dai et al., 2002]. However, the reported room-temperature hole densities (10^{19} cm^{-3}) and mobilities (0.3-9 cm^2/Vs) are incompatible with our results. Furthermore, there was no clear dependence of these values on In concentration [Fix et al., 2008].

In conclusion, we have observed *p*-type conductivity in annealed STO single crystals, with surprisingly high Hall mobilities in the 200-500 cm^2/Vs range with ReO_2 contacts. While the specific acceptor defect has not been identified, the results are consistent with a native defect such as the $V_{\mathrm{Ti}} - V_{\mathrm{O}}$ pair. Another possibility is the strontium vacancy (V_{Sr}), which has a calculated acceptor level 0.2 eV above the valence-band maximum [Janotti et al., 2014]. Finally, we note that thermally stimulated current measurements by Morin and Oliver suggested the presence of a 0.18 eV acceptor level [Morin and Oliver, 1973]. The authors assigned the level to Al acceptors; however, EPR spectra on our samples do not show the Al signature [Ensign and Stokowski, 1973, Poole et al., 2015b].

Weeks later the *p*-type samples; T8V, BVR, and BGP, were repolished and Hall measurements were attemped again without success. Then Seebeck measurements were performed. All three samples showed n-type conductivity. Most likely, the surface layer is n-type and can form, after polishing, over the period of “days”. This may occur though a slow oxidation process on the surface from being in contact with the atmosphere [Henrich et al., 1978]. Seebeck and Hall effect measurements determine charge carrier types differently, Seebeck determines the majority charge carrier, while Hall effect does a weighted average. The weighting is determined by the mobility, and if the holes have a very high mobility compared to the lower mobility electrons, its possible Hall effect would say p-type even though there are more electrons present.

Chapter EIGHT

ANNEALING ENVIRONMENT

Conditions during the annealing process are important for the formation of the desired defects. Varying the annealing parameters and observing the changes that occur provide insight into the defects responsible for PPC.

8.1 Annealing Temperature

Persistent photoconductivity can be induced in STO after an SrO anneal at 1200°C, but how important is the annealing temperature? Blazey and Weibel [Blazey and Weibel, 1984] reported that in the optical absorption spectra, changes happen with annealing temperatures of 1200°C. Wild and Rockar [Wild et al., 1973] noticed that heavily Fe doped STO exhibited metallic-like conductivity when reduced above 1200°C in a hydrogen atmosphere and quenched, whereas an 1100°C anneal was still insulating. The reasons for these spectral changes are not clear, but there are several things that are known to happen at 1200°C or above. When a crystal is cooled rapidly from 1200°C, the Fe^{5+} state can be produced [Morin and Oliver, 1973]. Strontium vacancies become mobile within the crystal [Moos and Hardtl, 1997], which can affect the charge neutrality and concentration of oxygen vacancies [Hanzig et al., 2011]. Additionally, temperatures exceeding 1200°C can result in the introduction of a sizeable concentration of oxygen vacancies (x >0.001) in $SrTiO_{(3-x)}$ just like reduction at extremely low oxygen partial pressures [Cordero et al., 2006].

It is worth investigating whether annealing temperatures above or below 1200°C affect the ability of an SrO anneal to induce PPC. Higher temperatures were tried first, but this turned out to be a bad idea, as you can see from the melted chip still in the ampoule in Figure 65. Annealing temperatures of 1250°C and even 1225°C gave this result. This is somewhat unusual since the melting point of pure STO is 2080°C and annealing temperatures higher than 1300°C, even as high as 1800°C, have been reported in the literature [Blazey and Weibel, 1984, Wild et al., 1973, Perluzzo and Destry, 1978]. However, there is some evidence to indicate the perovskite structure may not be stable above 1200°C [Menesklou et al., 1999]. Strontium and vacancies thereof be-

Figure 65: STO crystal from MTI G130406 melted into the ampoule after an anneal at 1225°C.

come mobile at this temperature [Moos and Hardtl, 1997, Hanzig et al., 2011] and the annealing environment is rich in strontium from the SrO powder.

Annealing temperatures lower than 1200°C were tried next. So far, chips from the same batch have always had the same behavior, so a batch that would display PPC behavior with an SrO anneal was found first (Figure 8), and then different annealing temperatures of 900°C, 1000°C and 1100°C were tried. These results can be seen in Figure 66, Figure 67 and Figure 68 respectively. None of these annealing temperatures yielded strong PPC, although higher temperatures yielded larger changes with light exposure. The UV Vis data after light exposure of samples SrO annealed at 1100°C, 1200°C and an as-received sample are presented in Figure 69. These spectra confirm that the 1200°C anneal produces PPC while the 1100°C does not. In conclusion, 1200°C is an optimal annealing temperature for PPC.

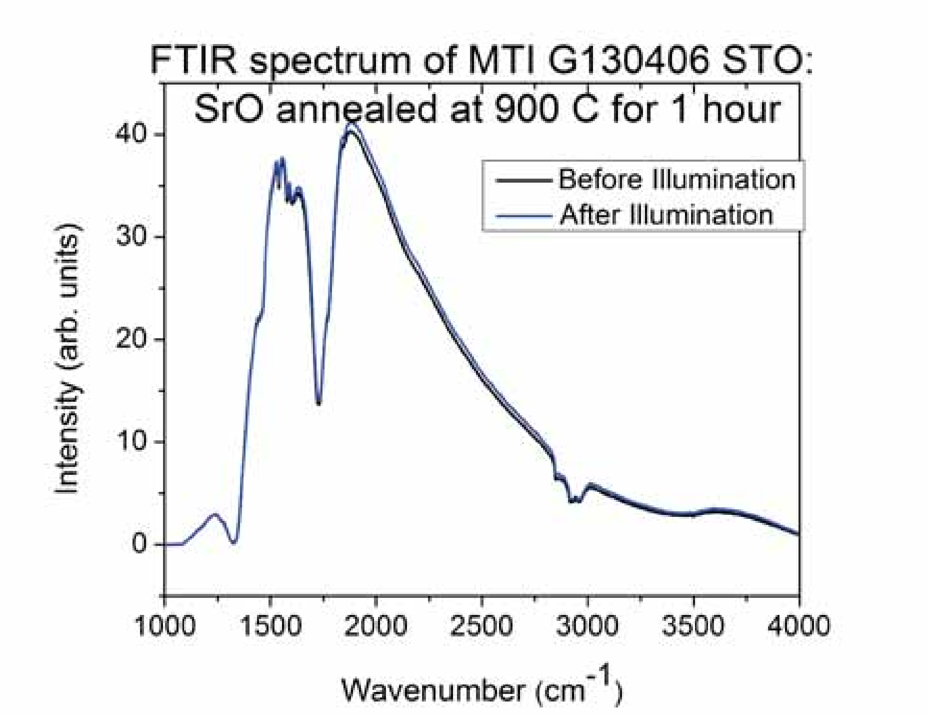

Figure 66: FTIR spectra with MCT detector of MTI G130406 STO chip. SrO annealed at 900°C.

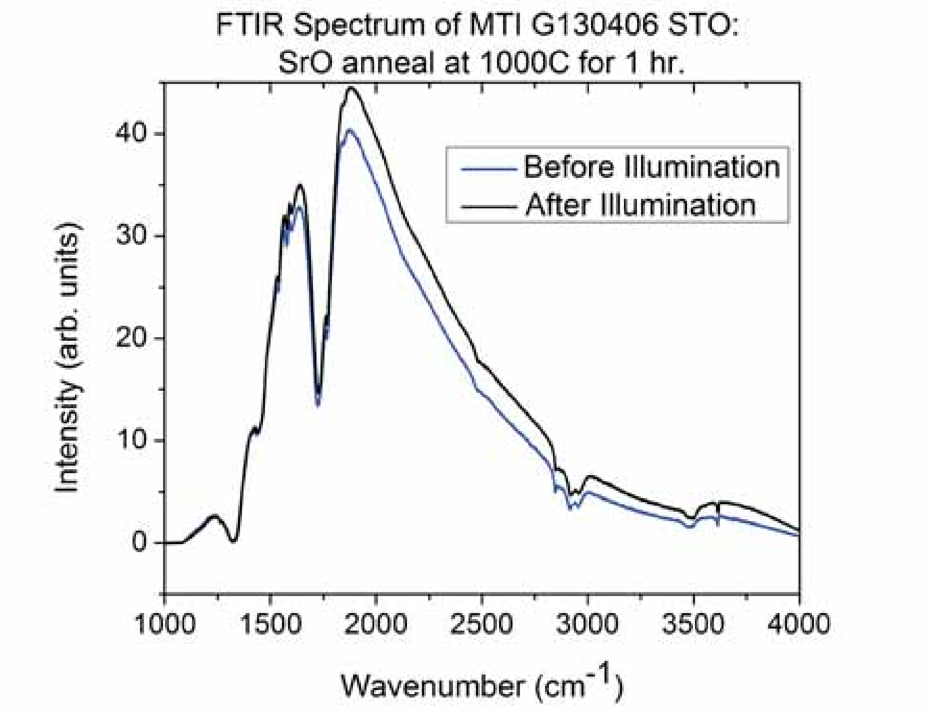

Figure 67: FTIR spectra with MCT detector of MTI G130406 STO chip. SrO annealed at 1000°C.

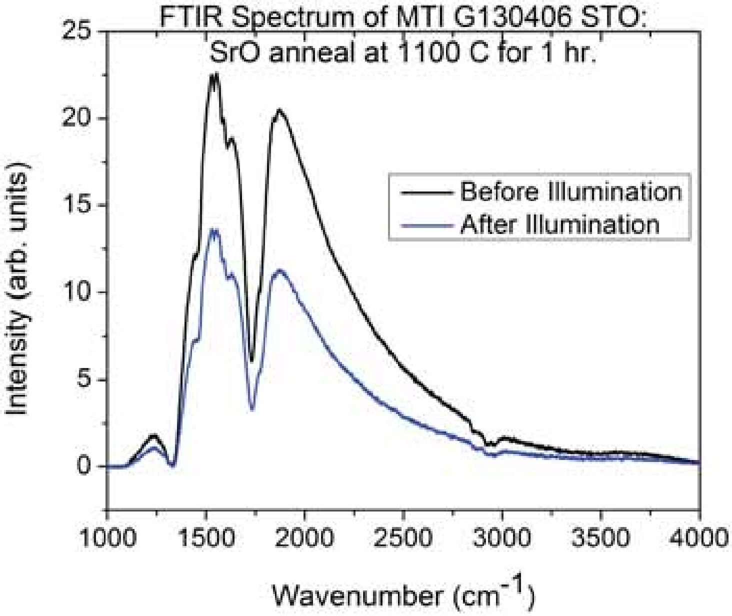

Figure 68: FTIR spectra with MCT detector of MTI G130406 STO chip. SrO annealed at 1100°C.

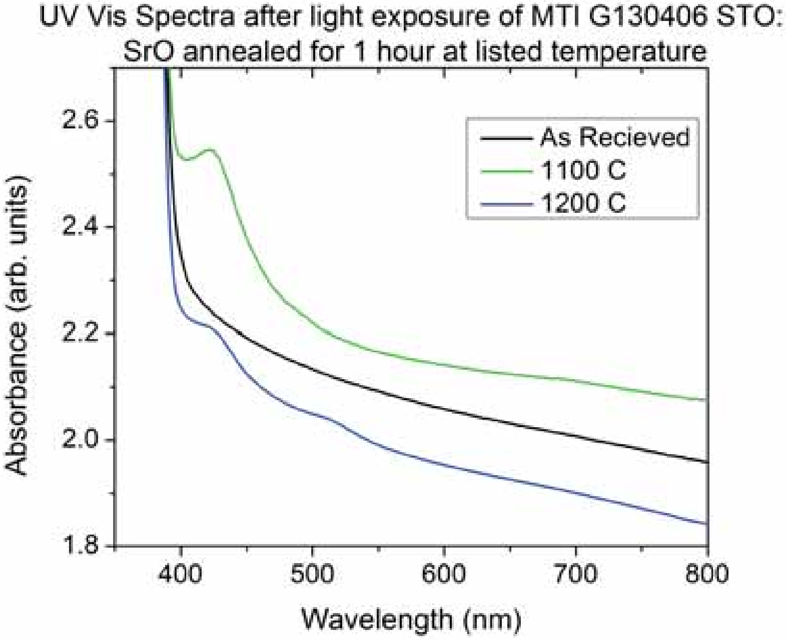

Figure 69: UV Vis spectra of MTI G130406 STO SrO annealed chips after light exposure. The sample annealed at 1100°C does not show the 520 nm peak.

8.2 Role of SrO Powder During Annealing

Understanding what occurs during the SrO anneal can help us identify the defects involved in the PPC phenomenon. We know that the SrO anneal is what causes the creation of PPC in STO, although it is unclear why or exactly what defects are created. Varying the amount of SrO used in the SrO annealing step can help us understand its role. Annealing at 1200^{o}C without SrO powder, essentially a vacuum anneal, results in a very dark, almost black sample. In contrast, after an SrO anneal, the chip is transparent or whitish opaque depending on surface polish. Lower temperature vacuum anneals result in light to medium grey chips depending on the level of vacuum used during the anneal. The two times I have tried this high temperature (1200^{o}C) vacuum anneal the chip stuck to the ampoule and shattered upon cooling, so no data are available.

Two chips from the same batch (Marketech 0049931) that exhibit PPC with only an SrO anneal at 1200^{o}C for 90 minutes were used. One chip had the normal amount of powder, 0.5 grams, added to the ampoule, while the other had only 0.1 grams added to the ampoule. The UV Vis spectra of these samples can be seen in Figure 70. The 0.1 g SrO anneal looks quite similar to some of the vacuum annealed spectra (Figure 11). Additionally, pressed indium two point measurements were made with a multimeter. The 0.5 gram anneal had 31 MΩ before light exposure and 162 Ω after, while the 0.1 gram anneal had 23 Ω before light exposure. The 0.1 gram anneal was too conductive to get a signal through with the FTIR.

The partial pressures of Sr and SrO gas over the SrO powder during annealing are incredibly small. Values of 0.0016 and 0.0004 mTorr, respectively, were measured at temperatures of around 1700 K [Asano et al., 1972]. These values are orders of magnitude smaller than the pressure inside the ampoule at room temperature of 50-100 mTorr. Therefore, it seems unlikely that a SrO anneal could introduce significant amounts of strontium into the chip, especially since the powder is not in direct contact with the chip. SrO could act as a Ti getter, creating Ti vacancies.

At annealing temperatures around 1000^{o}C, a redistribution of strontium and titanium rich phases has been observed on the surface of strontium titanate crystals [Szot et al., 1997]. Specifically, oxidizing conditions lead to strontium rich phases on the surface, while reducing conditions lead to titanium rich phases on the surface. This is somewhat surprising, since it occurs

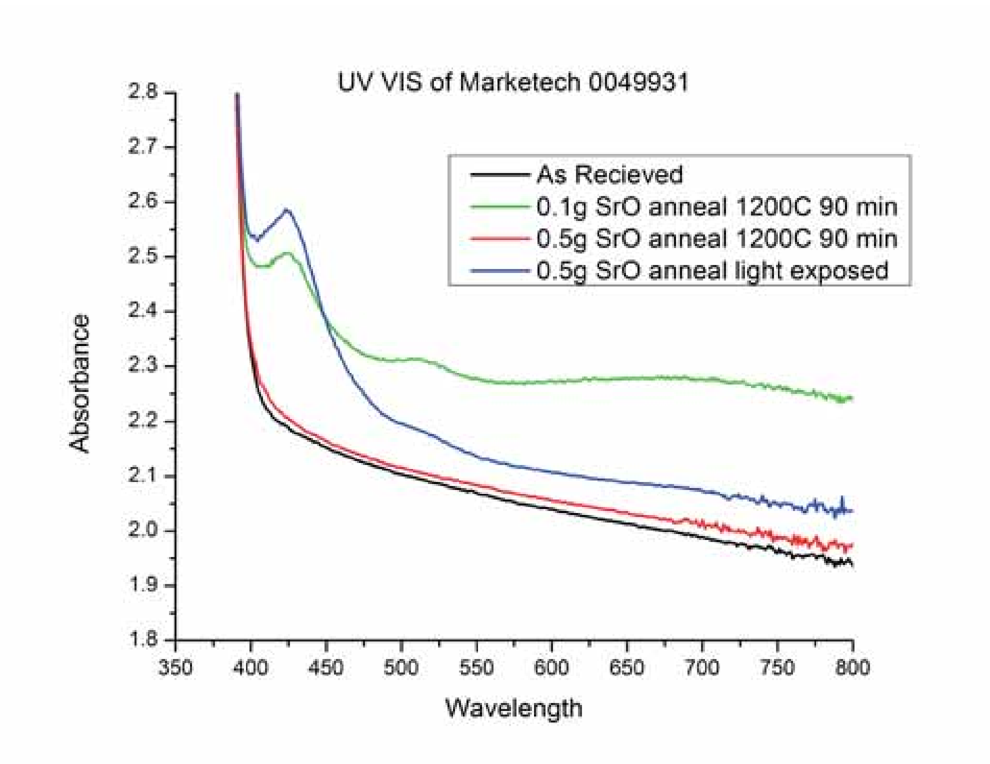

Figure 70: Comparison of anneals with different amounts of SrO powder. The 0.1 gram anneal looks more like a vacuum anneal, rather than the normal 0.5 gram anneal.

at a temperature lower than 1200°C, where strontium vacancies are known to become mobile [Hanzig et al., 2011]. It is believed that the force driving the redistribution of the atomic layers is due to the concentration gradient of oxygen between the bulk of the crystal and the surface in contact with a low or high partial pressure of oxygen [Szot et al., 1997].

The atmosphere around the chip during our SrO anneal is similar to a reducing atmosphere, but with a very small amount of SrO and Sr partial pressure added to the mix. The reducing atmosphere will cause strontium to move inwards and titanium to move outwards in the near surface region. A higher temperature will likely speed up this reaction and possibly increase its region of effect beyond the near surface region, since our anneal is carried out at the temperature where strontium vacancies are also mobile. The additional strontium present in our annealing environment would likely increase this migration tendency, driving more SrO inwards. A possible result would be the formation of titanium vacancies or vacancy complexes in the bulk. STO is known to contain Sr vacancies [Moos and Hardtl, 1997], so it is also possible that the SrO anneal is filling those vacancies. Electrical measurements lend some support to this idea of a segregated layer structure at the surface, since we observe an increase in sample resistance by approximately 1-2 orders of magnitude when the surface is sanded, as previously mentioned in Chapter 6.

8.3 TiO_2 Annealing

Another way to understand the role SrO powder is playing is to replace it with something else. We decided to look at the effect a TiO_2 anneal has. A 1200°C anneal in vacuum with TiO_2 powder (rutile) added to the ampoule results in a very darkly colored, almost black chip. This is similar to what happens after a vacuum anneal at 1200°C. The sample is very conductive (130 Ω) so FTIR measurements showed zero transmission. As shown in Figure 71, the 430 nm and 520 nm peaks are present as well as a large continuum absorption, which explains the dark color. Heat treatments performed in the open air allow us to monitor when these spectral features disappear. After each point a two point measurement was taken with pressed indium contacts and a multimeter until the chip became too resistive to measure.

It is not until 625°C that the peaks in the UV Vis spectrum disappear. This is very different from an SrO anneal, where there is low continuum absorption and the peaks at 430 and 520 nm

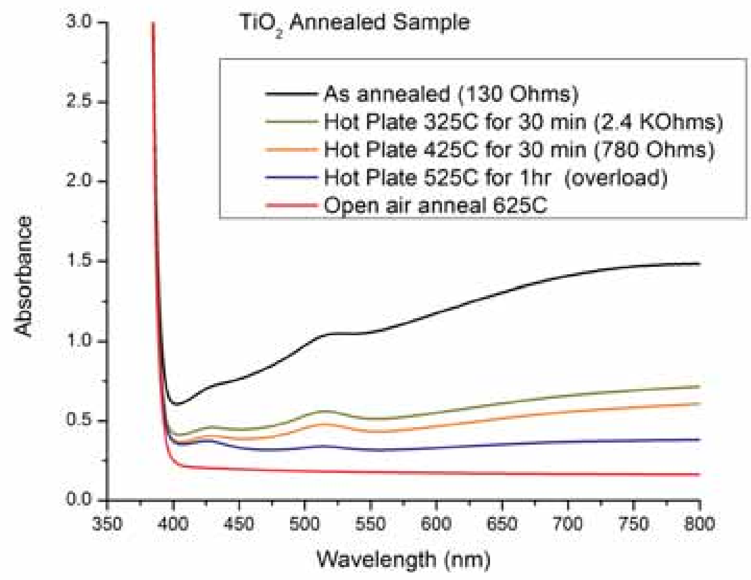

Figure 71: UV Vis of TiO_2 annealed sample and after erasing at various temperatures with an open air anneal. Both peaks (430 and 520 nm) are present after annealing and do not fully disappear until after heating to 625°C. Resistance measurements were taken with a multimeter and pressed indium contacts.

disappear after a heat treatment of only 300°C. After the heat erasure of the TiO_2 chip, it is possible to obtain an FTIR spectrum. Figure 72 shows that the sample contains both H_I and H_{II} lines, as well as the first H_I satellite. Seebeck and Hall effect measurements indicate mostly *p*-type behavior after erasure. A resistivity of (6.0 ± 0.6) x 10^9 Ω cm is obtained, with a mobility of (36 ± 36) cm^2/Vs and a density of (1.6 ± 2.6) x 10^8 cm^{-3} carriers at 400 K. Room temperature measurements were not taken as the resistivity was too high to get a reliable measurement.

The vacuum conditions during the TiO_2 anneal introduce a great number of free carriers, likely due to oxygen vacancies. Therefore, an open air TiO_2 anneal was also investigated, where the chip was buried in contact with 0.7 grams of TiO_2 powder. The chip turned light grey upon cooling. The UV Vis spectrum has no apparent peaks and increases towards the band edge (Figure 73). The low temperature FTIR spectrum is somewhat different (Figure 74). Again the sample contains both the both H_I and H_{II} lines, as well as the first H_I satellite. But here we see a large, broad feature at 3430 cm^{-1} from the open air TiO_2 anneal. Recall from earier, that an open air anneal by itself would tend to remove the H_{II} lines from the chip, and they are usually not

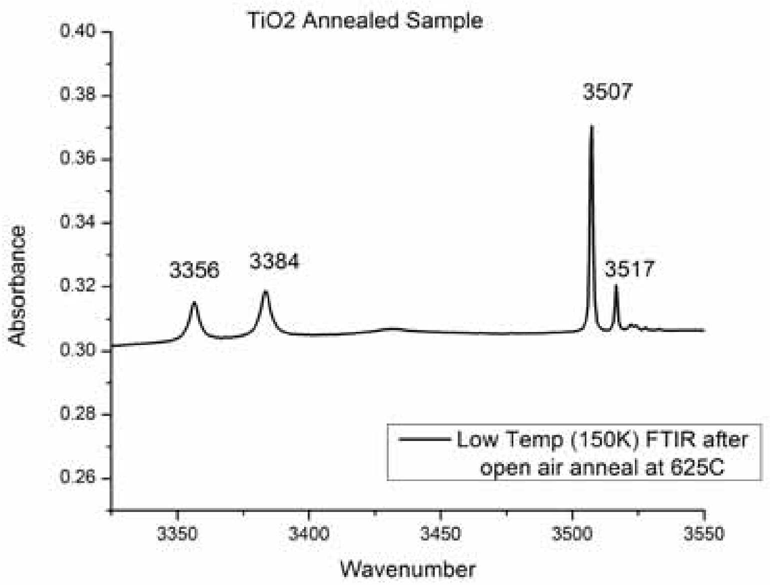

Figure 72: Low temp FTIR spectrum showing the hydrogen peaks present in a TiO_2 annealed sample. Notice that the sample contains both H_I and H_{II} lines, as well as the first H_I satellite.

present in as-received STO. The open air TiO_2 anneal might be encouraging hydrogen defects to be incorporated into the lattice. Electrical measurements with rhenium dioxide contacts showed a resistivity of 10^9 Ω cm. Seebeck measurements indicate p-type conduction, upon heating the sample to 350°C. Room temperature measurements were not possible due to high resistance.

Theoretical calculations from Fongkaew [Fongkaew et al., 2013] have vibrational frequencies for various complexes of hydrogen and titanium vacancies, $(n\text{H-}V_{\text{Ti}})^{-4+n}$, in the range 2900-3400 cm^{-1}. While the new observed peak has a higher frequency than those calculated, the paper also underestimates the frequencies of the H_{II} lines, so it is possible this is an another hydrogen-titanium vacancy complex. Recall that in an oxygen atmosphere, a high temperature anneal will tend to cause titanium to diffuse inwards and strontium to diffuse outwards [Szot et al., 1997]. The inward migration of titanium in an environment rich in titanium, would argue against the formation of bulk titanium vacancies. However, the formation of strontium vacancy complexes (V_{Sr}-H) would be favored in an environment rich in titanium and oxygen.

The properties of STO after a TiO_2 anneal in part depends on the atmosphere. Vacuum conditions result in a very conductive chip, while an open air or an oxygen anneal results in a very

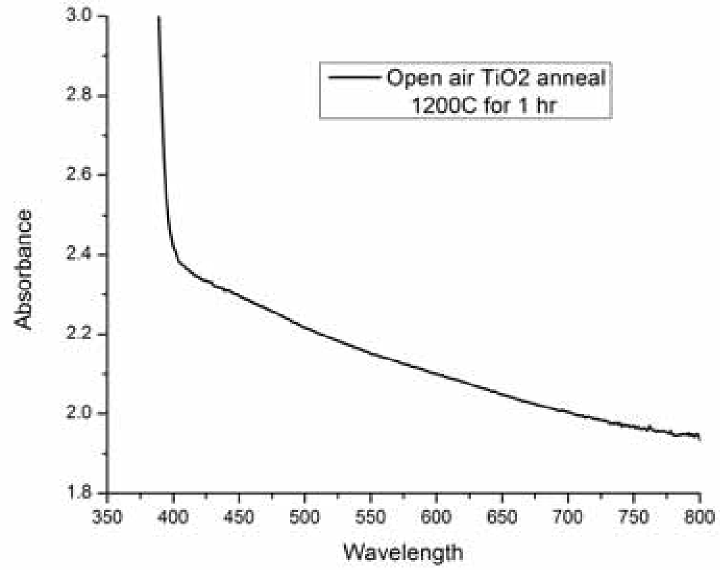

Figure 73: UV Vis spectrum after an open air TiO_2 anneal. No peaks are clearly visible, but the absorbance increases until the band edge.

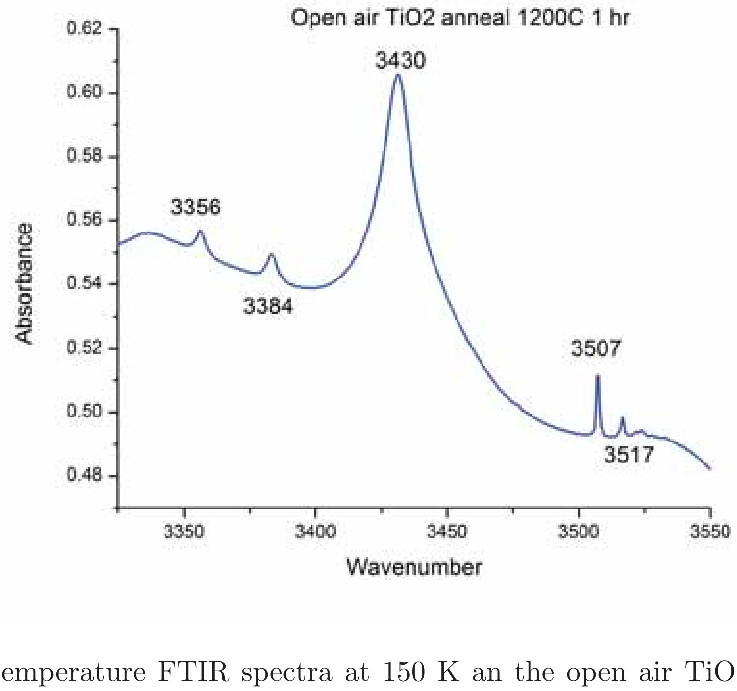

Figure 74: Low temperature FTIR spectra at 150 K an the open air TiO_2 annealed STO chip. The peak at 3430 cm^{-1} is unique to the oxidized titanium anneal.

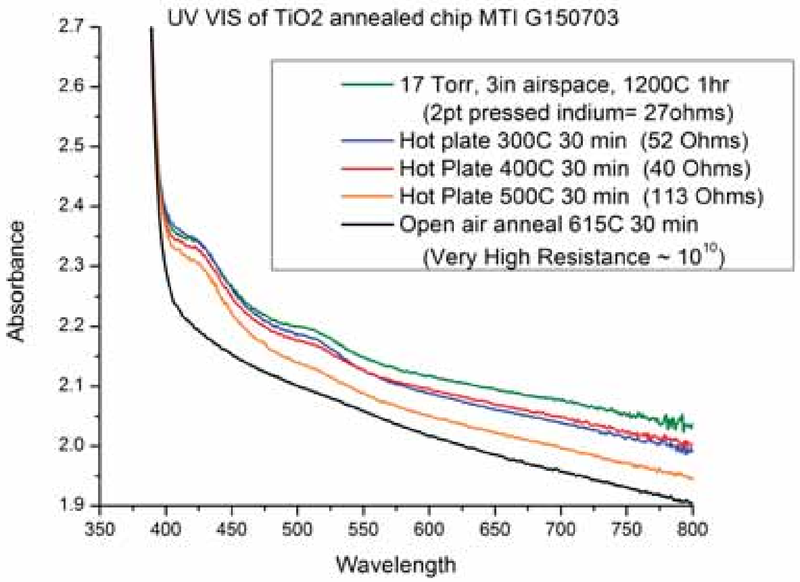

Figure 75: UV Vis spectra and two point pressed indium multimeter electrical measurements on the TiO_2 annealed sample conducted under an atmosphere of about 17 Torr at room temperature and after subsequent heat treatment erasing steps.

resistive chip. To investigate this further, a TiO_2 anneal with an intermediate partial pressure of atmosphere was performed. A three inch sample space was used, with an atmospheric pressure of around 17 Torr at the beginning of sealing the ampoule, with 0.5 grams TiO_2 powder. UV Vis spectra and pressed indium two point measurements after annealing, and after each subsequent erasing heat treatment are shown in Figure 75. FTIR spectra was taken after erasure at 615°C and can be seen in Figure 76. This time only the H_I peak and the first satellite are observed.

In general, the TiO_2 annealed samples' main electrical properties are related to the partial pressure of oxygen during the anneal. Samples where the annealing environment was oxidizing are very resistive, while if the annealing environment is reducing they show very low resistance until heat erasure at or above $\sim$ 600°C. Its important to note that erasure occurs at a much higher temperature in TiO_2 annealed samples than in SrO annealed samples (300°C). In SrO annealed samples, electrons are removed from the conduction band at low temperatures (200-300°C), while higher temperatures of 450°C causes oxygen vacancies to leave the chip. In the TiO_2 annealed chips, the oxygen vacancies are more stable and do not leave the chip until somewhere around 525-600°C.

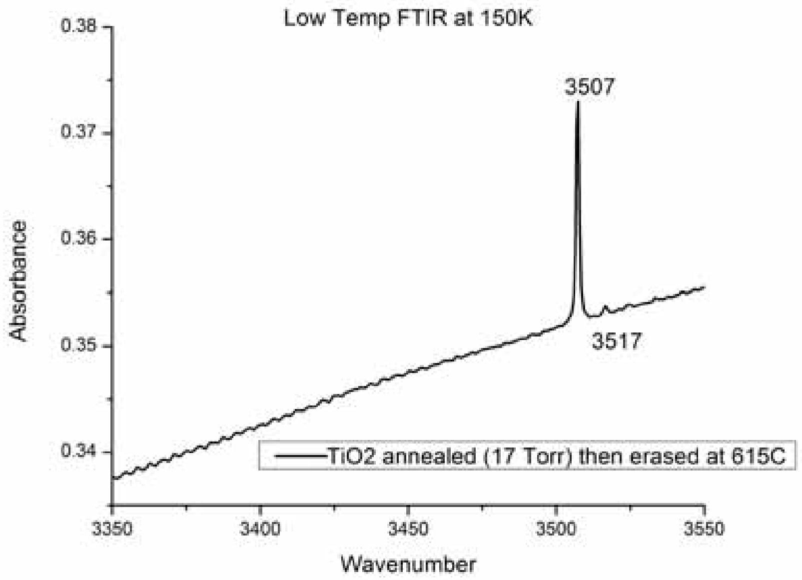

Figure 76: Low temperature FTIR spectrum taken at 150K of TiO_2 annealed at around 17 Torr. Notice that here only the H_I peak and the first satellite are seen.

8.4 Summary

We have explored various details of the annealing environment and have learned that annealing in SrO powder at 1200°C is crucial to the formation of PPC. Lower temperatures do not result in PPC while higher temperatures will destroy the chip. The amount of SrO powder used in the anneal is also important. Too little SrO and one is essentially performing a high temperature vacuum anneal, which results in a chip with drastically different properties.

Vacuum annealing introduces oxygen vacancies and increases the conductivity. Whereas, SrO annealed chips do not display a significant increase in conductivity until after light exposure. The powder is suppressing the immediate increase in conductivity. Other powders, such as TiO_2, do not display large PPC. The SrO powder may be causing the formation of titanium vacancies. A TiO_2 anneal would not result in these same vacancies.

Chapter NINE

CONCLUSIONS

We have investigated many aspects of the PPC phenomenon in strontium titanate. The increased conductivity observed during PPC was measured by Hall effect and increased IR absorption. We have found that PPC is correlated with (1) 520 nm peak in the UV Vis, (2) EPR line at g = 2.0131 and (3) H_I satellite lines. The defect responsible for PPC is possibly a $V_{\mathrm{Ti}} - V_{\mathrm{O}}$ acceptor. This defect complex may also contain hydrogen.

Spectrally, there are several changes that accompany PPC. In the IR region of the spectrum, free carrier absorption increases during PPC, leading to a large drop in the transmission of light through the sample. The shape of the free carrier absorption in PPC is the same as in other conductive STO samples. In the UV Vis region of the spectrum a peak appears at 520 nm. Again, we propose this PPC defect may be due to a titanium vacancy complex. The Fe^{4+} peak at 430 nm is always seen after light exposure, and depending on the amount of oxygen vacancies and complexes thereof, can be present beforehand. This is because more oxygen vacancies results in more $\mathrm{Fe}^{3+} - V_{\mathrm{O}}$ which will react with Fe^{3+} to yield Fe^{4+}. More of a reduction anneal or faster cooling results in a non-equilibrium condition where more oxygen vacancies are 'frozen in'.

The most dramatic changes in resistance are observed when the iron peak is not present before light exposure. After light exposure there are many free electrons in the chip, hence its resistance is low. When iron is in the 4+ charge state, some free electrons are already present in the conduction band. However, when iron is in the 3+ charge state, electrons from oxygen vacancies are not trapped in the conduction band. This results in a higher resistance, so the decrease in resistance is larger when the 430 nm peak is not present beforehand.

EPR results show Cr^{3+} ions are present after the SrO anneal and disappear with light exposure. As-grown samples also show chromium, so we know it is present in our nominally pure samples and could be important for PPC and for *p*-type conductivity. An unidentified defect (g=2.0131) with a similar g value to that of Fe^{3+} (g=2.007) was also observed before light exposure and after SrO annealing. This center is not Fe^{5+}, and disappears upon light exposure. Additionally, this possible PPC defect might have been observed before by Ensign and Stokowski, which they call

$X - O^-$. The most probably identity for this center is a titanium vacancy.

The ability to induce PPC in a sample depends on several factors. Oxygen vacancies are needed for PPC, as we have shown by EPR and by introducing a vacuum anneal in non-working batches. This is consistent with the $V_{\mathrm{Ti}} - V_{\mathrm{O}}$ acceptor model. The oxygen vacancies may also provide a source of free electrons for the acceptors. Additionally, it is necessary that the temperature of the SrO anneal to be 1200°C. This may be because strontium and vacancies thereof become mobile at this temperature. The amount of SrO powder used in the anneal is also crucial – too little and PPC will not be induced. Annealing likely results in the migration of strontium inwards and titanium outwards. Additional strontium from the SrO powder would increase this migration, resulting in the necessary concentration of defects. The annealing conditions probably lead to the formation of titanium vacancies and/or filling of strontium vacancies within the bulk.

Hydrogen present in the H_{II} lines will prevent PPC. We know that the H_{II} center contains two hydrogen atoms, however we do not know if these two hydrogen atoms are attached to a strontium or titanium vacancy or are just neighboring interstitials. Theoretical calculations indicate hydrogen at a titanium vacancy is the most likely defect responsible for the H_{II} lines. Hydrogen in the titanium vacancy may passivate it, preventing the defect from participating in PPC. Iron doped chips could not be made to have PPC, perhaps due to the increased stability observed in the H_{II} lines. The hydrogen present in the H_{II} lines can be removed by open air annealing at 1200°C in pure STO chips but not in iron doped chips.

The H_I line around 3500 cm^{-1} and satellites at higher wavenumber are observed in as-grown STO. The satellites disappear after SrO annealing and return with light exposure. A similar trend is observed in the main line, where the H_I line decreases instead of fully disappearing. The hydrogen satellite lines are strongly correlated with PPC, but we do not know if it is the PPC defect or due to the different charge states of the H defects. While the identity of the satellite lines is not known, they are hydrogen related. Hydrogen interacting with iron oxygen vacancy complexes or strontium vacancies are the most likely culprits from experimental and theoretical evidence, respectively.

The changes induced by light exposure in PPC can be erased, so that re-exposing to light will again introduce PPC. Light will not erase PPC, but a short duration heat treatment conducted at

300^{o}C in the open air will. This temperature is optimal for erasing, since higher temperatures will lead to the loss of too many oxygen vacancies, resulting in permanent erasure. The hydrogen lines, H_I and satellites, have the same thermal kinetics as the peak at 520 nm, since they erase at lower temperatures of 200^{o}C. The iron peak does not completely disappear at this lower temperature. Higher temperatures of 300^{o}C are required to remove the free electrons from the conduction band and decrease the charge state of the iron atoms from Fe^{4+} to Fe^{3+}.

Electrical measurements show a large increase in the free carrier concentration during PPC, around three orders of magnitude. Some samples showed weakly *p*-type behavior if they were heat erased at 300^{o}C to remove any free electrons from the conduction band and then sanded after SrO annealing and prior to light exposure. Sanding may be crucial to the observation of *p*-type behavior, since it removes an *n*-type surface layer, resulting in an order of magnitude increase in the resistance.

BIBLIOGRAPHY

[Alkauskas et al., 2016] Alkauskas, A., McCluskey, M. D., and Van de Walle, C. G. (2016). Tutorial: Defects in semiconductors - Combining experiment and theory. *J. Appl. Phys.*, 119(18):181101.

[Asano et al., 1972] Asano, M., Yamamoto, Y., Sasaki, N., and Kubo, K. (1972). Parital Pressures of Strontium and Strontium Oxide over Strontium Oxide heated on Platinum. *Bull. Chem. Soc. Jpn.*, 45(1):82–87.

[Badalyan et al., 2013] Badalyan, A. G., Azamat, D., Babunts, R. A., Neverova, E. V., Dejneka, A., Trepakov, V. A., and Jastrabik, L. (2013). EPR study of charge compensation of chromium centers in the strontium titanate crystal. *Phys. Solid State*, 55(7):1454–1458.

[Badekar, 1907] Badekar, K. (1907). Electrical Conductivity and Theromoelectric Power of Some Heavy Metal Compounds. *Ann. Phys.*, 22:749.

[Baer, 1966] Baer, W. S. (1966). Free-Carrier Absorption in Reduced SrTiO3. *Phyical Rev.*, 144(2):734–738.

[Baikie et al., 2000] Baikie, I. D., Petermann, U., Speakman, A., Lagel, B., Dirscherl, K. M., and Estrup, P. J. (2000). Work function study of rhenium oxidation using an ultra high vacuum scanning Kelvin probe. *J. Appl. Phys.*, 88(7):4371–4375.

[Balachandran and Eror, 1982] Balachandran, U. and Eror, N. G. (1982). On the defect structure of strontium titanate with excess SrO. *J. Mater. Sci.*, 17(7):2133–2140.

[Berney and Cowan, 1981] Berney, R. L. and Cowan, D. L. (1981). Photochromism of three photosensitive Fe centers in SrTiO3. *Phys. Rev. B*, 23(1):37–50.

[Bierwagen et al., 2008] Bierwagen, O., Ive, T., Van de Walle, C. G., and Speck, J. S. (2008). Causes of incorrect carrier-type identification in van der Pauw Hall measurements. *Appl. Phys. Lett.*, 93(24):242108.

[Blazey and Weibel, 1984] Blazey, K. W. and Weibel, H. (1984). Optical absorption spectra of reduced transition metal ion doped SrTiO3. *J. Phys. Chem. Solids*, 45(8):917–922.

[Brebner et al., 1981] Brebner, J. L., Jandl, S., and Lepine, Y. (1981). Infrared defect absorption in strontium titanate. *Phys. Rev. B*, 23(8):3816–3822.

[Bright, 2007] Bright, C. I. (2007). Review of Transparent Conductive Oxides (TCO). In Mattox, D. M. and Mattox, V. H., editors, *50 Years Vac. Coat. Technol. Growth Soc. Vac. Coaters*, chapter Chapter 7:, page 38. 3M Company, Tuscon.

[Carnes and Goodman, 1967] Carnes, J. E. and Goodman, A. M. (1967). Evaporated Metallic Contacts to Conducting Strontium Titanate Single Crystals. *J. Appl. Phys.*, 38(8):3091.

[Connes and Connes, 1966] Connes, J. and Connes, P. (1966). Near-Infrared planetary spectra by Fourier Spectroscopy. I. Instruments and Results. *J. Opt. Soc. Am*, 56:896–910.

[Cordero et al., 2006] Cordero, F., Franco, A., Calderone, V. R., Nanni, P., and Buscaglia, V. (2006). Anelastic relaxation in SrTiO3 with O vacancies and H. *Mater. Sci. Eng. A*, 442(1-2):55–58.

[Cowley, 1996] Cowley, R. A. (1996). The Phase Transition of Strontium Titanate. *Philos. Trans. R. Soc. A Math. Phys. Eng. Sci.*, 354(1720):2799–2814.

[Dai et al., 2002] Dai, S., Lu, H., Chen, F., Chen, Z., Ren, Z. Y., and Ng, D. H. L. (2002). In-doped SrTiO3 ceramic thin films. *Appl. Phys. Lett.*, 80(19):3545–3547.

[Denk et al., 1995] Denk, I., Munch, W., and Maier, J. (1995). Partial Conductivities in SrTiO3: Bulk Polarization Experiments, Oxygen Concentration Cell Measurements, and Defect-Chemical Modeling. *J. Am. Ceram. Soc.*, 78(12):3265–3272.

[Dischler and Räuber, 1975] Dischler, B. and Räuber, A. (1975). Oxygen vacancy model for chemochromic effects in LiNbO3 doped with Mn, Fe or Cu. *Solid State Commun.*, 17(8):953–956.

[Ensign and Stokowski, 1973] Ensign, T. C. and Stokowski, S. E. (1973). Shared Holes Trapped by Charge Defects in SrTiO3. *Phys. Rev. B*, 1(6):1689–1699.

[Faughnan, 1971] Faughnan, B. W. (1971). Photochromism in Transition Metal Doped SrTiO3. *Phys. Rev. B*, 4(10):3623–3636.

[Faughnan and Kiss, 1968] Faughnan, B. W. and Kiss, Z. J. (1968). Photoinduced Reversible Charge Transfer Processes in Transition Metal Doped Single Crystal SrTiO3 and TiO2. *Phys. Rev. Lett.*, 21(18):1331–1334.

[Fellget, 1958] Fellget, P. (1958). A contribution to the theory of the multiplex interferometric spectrometer. *J. Phys. Radium*, 19:187–191.

[Fix et al., 2008] Fix, T., Bali, R., Stelmashenko, N., and Blamire, M. G. (2008). Influence of the dopant concentration in In doped SrTiO3 on the structural and transport properties. *Solid State Commun.*, 146(9-10):428–430.

[Fongkaew et al., 2013] Fongkaew, I., T-Thienprasert, J., Singh, D., Du, M.-H., and Limpijumnong, S. (2013). First principles calculations of hydrogen titanium vacancy complexes in SrTiO3. *Ceram. Int.*, 39:S273–S276.

[Frederikse and Hosler, 1967] Frederikse, H. P. R. and Hosler, W. R. (1967). Hall mobility in SrTiO3. *Phys. Rev.*, 161(3):822–827.

[Fujishiro and Mochizuki, 2005] Fujishiro, F. and Mochizuki, S. (2005). Photo induced phenomena in SrTiO3. *J. Phys. Conf. Ser.*, 21:142–148.

[Gevorgian, 2009] Gevorgian, S. (2009). *Ferroelectrics in Microwave Devices, Circuits and Systems: Physics, Modeling, Fabrication and Measurements.* Springer Science and Business Media.

[Grone et al., 1990] Grone, A., Wohlecke, M., Kapphan, S., and Waser, R. (1990). High resolution IR absorption spectroscopy of the OH stretch modes in SrTiO3:Fe. *Ferroelectrics*, 107(1):97–102.

[Hanzig et al., 2011] Hanzig, J., Abendroth, B., Hanzig, F., Stocker, H., Strohmeyer, R., Meyer, D. C., Lindner, S., Grobosch, M., Knupfer, M., Himcinschi, C., Muhle, U., and Munnik, F. (2011). Single crystal strontium titanate surface and bulk modifications due to vacuum annealing. *J. Appl. Phys.*, 110(6):064107.

[Harman and Honig, 1967] Harman, T. C. and Honig, J. M. (1967). *Thermoelectric and Thermomagnetic Effects and Applications*. McGraw-Hill Book Company, New York.

[Harris and Bertolucci, 1978] Harris, D. C. and Bertolucci, M. D. (1978). *Symmetry and Spectroscopy: An Introduction to Vibrational and Electronic Spectroscopy*. Oxford University Press, New York.

[Henrich et al., 1978] Henrich, V., Dresselhaus, G., and Zeiger, H. (1978). Surface defects and the electronic structure of SrTiO3 surfaces. *Phys. Rev. B*, 17(12):4908–4921.

[Higuchi et al., 1998] Higuchi, T., Tsukamoto, T., Sata, N., Ishigame, M., Tezuka, Y., and Shin, S. (1998). Electronic structure of p-type SrTiO3 by photoemission spectroscopy. *Phys. Rev. B*, 57(12):6978–6983.

[Himmetoglu et al., 2014] Himmetoglu, B., Janotti, A., Peelaers, H., Alkauskas, A., and Van De Walle, C. G. (2014). First-principles study of the mobility of SrTiO3. *Phys. Rev. B - Condens. Matter Mater. Phys.*, 90(24):1–5.

[Hirsch et al., 1997] Hirsch, M. T., Wolk, J. A., Walukiewicz, W., and Haller, E. E. (1997). Persistent photoconductivity in n-type GaN. *Appl. Phys. Lett.*, 71(1997):1098–1100.

[Hollas, 2004] Hollas, J. M. (2004). *Modern Spectroscopy*. John Wiley and Sons, Ltd., West Sussex, fourth edition.

[Houde et al., 1987] Houde, D., Lepine, Y., Pepin, C., Jandl, S., and Brebner, J. L. (1987). High-resolution infrared spectroscopy of hydrogen impurities in strontium titanate. *Phys. Rev. B*, 35(10):4948–4953.

[Jacquinot, 1960] Jacquinot, P. (1960). New Developments in Interference Spectroscopy. *Rep. Prog. Phys.*, 23:267–312.

[Janotti et al., 2014] Janotti, A., Varley, J. B., Choi, M., and Van de Walle, C. G. (2014). Vacancies and small polarons in SrTiO3. *Phys. Rev. B*, 90(April):085202.

[Janousch et al., 2007] Janousch, M., Meijer, G. I., Staub, U., Delley, B., Karg, S. F., and Andreasson, B. P. (2007). Role of oxygen vacancies in Cr doped SrTiO3 for resistance change memory. *arXiv e-print*, page 13.

[Jarzebski, 1973] Jarzebski, Z. M. (1973). *Oxide Semiconductors*. Pergamon Press, NY, 1st englis edition.

[Jeong et al., 2012] Jeong, E. D., Yu, S. M., Yoon, J. H., Bae, J. S., Cho, C. R., Lim, K. T., Borse, P. H., and Kim, H. G. (2012). The co-dopant concentration dependence on visible light photocatalytic efficiency in perovskite photocatalysts. 13(5):517–522.

[Khanna, 2014] Khanna, V. K. (2014). *Fundamentals of Solid-State Lighting: LEDs OLEDs, and Their Applications in Illumination and Displays*. CRC Press.

[King and Veal, 2011] King, P. D. C. and Veal, T. D. (2011). Conductivity in transparent oxide semiconductors. *J. Phys. Condens. Matter*, 23(33):334214.

[Klukhuhn et al., 1970] Klukhuhn, A. F. W., Bruining, J., Klootwijk, B., and van der Elsken, J. (1970). Electric field dependence of a hydrogen impurity mode in SrTiO3. *Phys. Rev. Lett.*, 25(6):380–383.

[Kulagin and Hieckmann, 2012] Kulagin, N. A. and Hieckmann, E. (2012). Spectra and color centers of strontium titanate crystals. *Opt. Spectrosc.*, 112(1):79–86.

[Lang and Logan, 1977] Lang, D. V. and Logan, R. A. (1977). Large-lattice-relaxation model for persistent photoconductivity in compound semiconductors. *Phys. Rev. Lett.*, 39(10):635–639.

[Lavrov et al., 2002] Lavrov, E., Weber, J., Börrnert, F., Van de Walle, C., and Helbig, R. (2002). Hydrogen-related defects in ZnO studied by infrared absorption spectroscopy. *Phys. Rev. B*, 66:1–7.

[Lebedeva et al., 1988] Lebedeva, N. N., Arushanov, A. G., Pokasova, N. S., and Gadgiev, M. S. (1988). The effect of structural defects in SrTiO3 on the luminescence, optical-absorption and the Conductivity. *Ferroelectrics*, 83:141–145.

[Levin, 1913] Levin, I. H. (1913). Synthesis of Precious Stones. *J. Ind. Eng. Chem.*, 5(6):495–500.

[Li et al., 1999] Li, J. Z., Lin, J. Y., Jiang, H. X., Geisz, J. F., and Kurtz, S. R. (1999). Persistent photoconductivity in GaInNAs. *Appl. Phys. Lett.*, 75(1999):1899.

[Long, 1968] Long, D. (1968). *Energy Bands in Semiconductors.* John Wiley and Sons, Inc., New York.

[Luiskutty and Ouseph, 1973] Luiskutty, C. T. and Ouseph, P. J. (1973). Valence states of iron in photochromic strontium titanate by Mossbauer effect. *Solid State Commun.*, 13(3):405–409.

[Ma et al., 2010] Ma, Q., Tietz, F., Sebold, D., and Stover, D. (2010). Y Substituted SrTiO3-YSZ Composite as Anode Material for Solid Oxide Fuel Cells: Interactions Between SYT and YSZ. *J. Power Sources*, 195:1920–1925.

[McCluskey and Haller, 2012] McCluskey and Haller (2012). *Dopants and Defects in Semiconductors.* CRC Press, Boca Raton.

[McCluskey and Tarun, 2014] McCluskey, M. D. and Tarun, M. C. (2014). Defects and persistent photoconductivity in SrTiO3. In *AIP Conf. Proc.*, volume 319, page 319.

[Melitz et al., 2011] Melitz, W., Shen, J., Kummel, A. C., and Lee, S. (2011). Kelvin probe force microscopy and its application. *Surf. Sci. Rep.*, 66(1):1–27.

[Menesklou et al., 1999] Menesklou, W., Schreiner, H.-J., Hardtl, K. H., and Ivers, E. (1999). High temperature oxygen sensors based on doped SrTiO3. *Sensors Actuators B*, 59:184–189.

[Meyer et al., 2003] Meyer, R., Waser, R., Helmbold, J., and Borchardt, G. (2003). Observation of Vacancy Defect Migration in the Cation Sublattice of Complex Oxides by 18O Tracer Experiments. *Phys. Rev. Lett.*, 90(10):105901.

[Minami, 2005] Minami, T. (2005). Transparent conducting oxide semiconductors for transparent electrodes. *Semicond. Sci. Technol.*, 20(4):S35 – S44.

[Moos and Hardtl, 1997] Moos, R. and Hardtl, K. H. (1997). Defect Chemistry of Donor-Doped and Undoped Strontium Titanate Ceramics between 1000 and 1400 C. *J. Am Ceram. Soc.*, 62(10):2549–2562.

[Moos et al., 1995] Moos, R., Menesklou, W., and Hardtl, K. H. (1995). Hall-Mobility of Undoped N-Type Conducting Strontium-Titanate Single-Crystals Between 19K and 1373K. *Appl. Phys. a-Materials Sci. Process.*, 61(4):389–395.

[Morin and Oliver, 1973] Morin, F. J. and Oliver, J. R. (1973). Energy Levels of Iron and Aluminum in SrTiO3. *Phys. Rev. B*, 8(12):5847–5854.

[Mott and Friedman, 1974] Mott, N. F. and Friedman, L. (1974). Metal Insulator Transitions in VO2, Ti2O3 and alloys. *Philos. Mag.*, 30(2).

[Nassau and Miller, 1988] Nassau, K. and Miller, A. E. (1988). Strontium titanate: An index to the literature on properties and the growth of single crystals. *J. Cryst. Growth*, 91(3):373–381.

[Nilsen and Skinner, 1968] Nilsen, W. G. and Skinner, J. G. (1968). Raman Spectrum of Strontium Titanate. *J. Chem. Phys.*, 48(5):2240.

[Nomura et al., 2003] Nomura, K., Ohta, H., Ueda, K., Kamiya, T., Hirano, M., and Hosono, H. (2003). Thin-film transistor fabricated in single-crystalline transparent oxide semiconductor. *Science (80-.).*, 300:1269–1272.

[Norby, 2009] Norby, T. (2009). Proton Conductivity in Perovskite Oxides. In Ishihara, T., editor, *Perovskite Oxide Solid Oxide Fuel Cells SE - 11*, Fuel Cells and Hydrogen Energy, pages 217–241. Springer US, NY.

[Okamura et al., 2006] Okamura, H., Matsubara, M., Tanaka, K., Fukui, K., Terakami, M., Nakagawa, H., Ikemoto, Y., Moriwaki, T., Kimura, H., and Nanba, T. (2006). Photogenerated carriers in SrTiO3 probed by mid-infrared absorption. *J. Phys. Soc. Japan*, 75(2):2–6.

[Palermo et al., 2006] Palermo, V., Palma, M., and Samori, P. (2006). Electronic characterization of organic thin films by Kelvin probe force microscopy. *Adv. Mater.*, 18(2):145–164.

[Parker and Yahia, 1968] Parker, D. and Yahia, J. (1968). AC Hall Measurements in Crystals of Strontium Titanate from 190 to 500 K: Dependence of Hall Mobility on Charge-Carrier Density. *Phys. Rev.*, 169(3):605–609.

[PerkinElmer Instruments, 2001] PerkinElmer Instruments (2001). Lambda 800/900 User's Guide. Technical report, Shelton.

[Perluzzo and Destry, 1978] Perluzzo, G. and Destry, J. (1978). The characterization of pure and niobium-doped crystals of strontium titanate using Hall, electrical conductivity, and optical absorption data. *Can. J. Phys.*, 56(4):453–467.

[Poole et al., 2015a] Poole, V. M., Corolewski, C. D., and McCluskey, M. D. (2015a). P-type conductivity in annealed strontium titanate. *AIP Adv.*, 5(12):127217.

[Poole et al., 2015b] Poole, V. M., Dashdorj, J., Zvanut, M. E., and McCluskey, M. D. (2015b). Large Persistent Photoconductivity in SrTiO3 at Room Temperature. In *MRS Proc.*, page 1792.

[Poole and McCluskey, 2016] Poole, V. M. and McCluskey, M. D. (2016). Large Persistent Photot-conductivity in Strontium Titanate. *Proc. SPIE 9749. Oxide-based Mater. Devices VII*, 97490N.

[Rochon et al., 1979] Rochon, P., Brebner, J. L., and Matz, D. (1979). The optical properties of SrTiO3 above 0.14 eV. *Solid State Commun.*, 29:63–66.

[Ruddlesden and Popper, 1958] Ruddlesden, S. N. and Popper, P. (1958). The compound Sr3Ti2O7 and its structure. *Acta Cryst.*, 11:54.

[Sata et al., 1996] Sata, N., Hiramoto, K., Ishigame, M., Hosoya, S., Niimura, N., and Shin, S. (1996). Site identification of protons in SrTiO3: Mechanism for large protonic conduction. *Phys. Rev. B*, 54(22):15795–15799.

[Scheel et al., 1976] Scheel, H. J., Bednorz, J. G., and Dill, P. (1976). Crystal growth of strontium titanate SrTiO3. *Ferroelectrics*, 13(1):507–509.

[Scott et al., 2001] Scott, J. F., Redfern, S. A. T., Zhang, M., and Dawber, M. (2001). Polarons, oxygen vacancies, and hydrogen in barium strontium titanate. *J. Eur. Ceram. Soc.*, 21:1629–1632.

[Shi et al., 2004] Shi, G. A., Saboktakin, M., Stavola, M., and Pearton, S. J. (2004). "Hidden hydrogen" in as-grown ZnO. *Appl. Phys. Lett.*, 85(23):5601–5603.

[Stocker et al., 2010] Stocker, H., Zschornak, M., Seibt, J., Hanzig, F., Wintz, S., Abendroth, B., Kortus, J., and Meyer, D. C. (2010). Formation of Schottky-type metal SrTiO3 junctions and their resistive properties. *Appl. Phys. A*, 100(2):437–445.

[Szot and Speier, 1999] Szot, K. and Speier, W. (1999). Surfaces of reduced and oxidized SrTiO3 from atomic force microscopy. *Phys. Rev. B*, 60(8):5909–5926.

[Szot et al., 2000] Szot, K., Speier, W., Breuer, U., Meyer, R., Szade, J., and Waser, R. (2000). Formation of micro-crystals on the (100) surface of SrTiO at elevated temperatures. *Surf. Sci.*, 460:112–128.

[Szot et al., 1997] Szot, K., Speier, W., Herion, J., and Freiburg, C. (1997). Restructuring of the surface region in SrTiO3. *Appl. Phys. A Mater. Sci. Process.*, 64(1):55–59.

[T-Thienprasert et al., 2012] T-Thienprasert, J., Fongkaew, I., Singh, D. J., Du, M.-H., and Limpijumnong, S. (2012). Identification of hydrogen defects in SrTiO3 by first-principles local vibration mode calculations. *Phys. Rev. B*, 85(12):125205.

[Takeyasu et al., 2013] Takeyasu, K., Fukada, K., Matsumoto, M., and Fukutani, K. (2013). Control of the surface electronic structure of SrTiO3(001) by modulation of the density of oxygen vacancies. *J. Phys. Condens. Matter*, 25(16):162202.

[Tarun and McCluskey, 2011] Tarun, M. C. and McCluskey, M. D. (2011). Infrared absorption of hydrogen-related defects in strontium titanate. *J. Appl. Phys.*, 109(6):063706.

[Tarun et al., 2013] Tarun, M. C., Selim, F. A., and McCluskey, M. D. (2013). Persistent Photoconductivity in Strontium Titanate. *Phys. Rev. Lett.*, 111(18):187403.

[Treharne, 2011] Treharne, R. (2011). *RF Magnetron Sputtering of Transparent Conducting Oxides and CdTe/CdS Solar Cells*. PhD thesis, University of Durham.

[Trepakov et al., 2009] Trepakov, V., Dejneka, A., Markovin, P., Lynnyk, A., and Jastrabik, L. (2009). A ‘soft electronic band’ and the negative thermooptic effect in strontium titanate. *New J. Phys.*, 11.

[Tufte and Chapman, 1967] Tufte, O. N. and Chapman, P. W. (1967). Electron Mobility in Semiconducting Strontium Titanate. *Phys. Rev.*, 155(3):796–802.

[Tuller and Bishop, 2011] Tuller, H. L. and Bishop, S. R. (2011). Point Defects in Oxides: Tailoring Materials Through Defect Engineering. *Annu. Rev. Mater. Res.*, 41(1):369–398.

[van der Pauw, 1958] van der Pauw, L. J. (1958). A method of measuring the resistivity and hall coefficient on lamellae of arbitrary shape. *Philips Tech. Rev.*, 20:220–224.

[Varley et al., 2014] Varley, J. B., Janotti, A., and Van de Walle, C. G. (2014). Hydrogenated vacancies and hidden hydrogen in SrTiO3. *Phys. Rev. B*, 89(7):075202.

[Verma et al., 2014] Verma, A., Kajdos, A. P., Cain, T. A., Stemmer, S., and Jena, D. (2014). Intrinsic mobility limiting mechanisms in lanthanum-doped strontium titanate. *Phys. Rev. Lett.*, 112(21):1–5.

[Weber et al., 1986] Weber, G., Kapphan, S., and Wohlecke, M. (1986). Spectroscopy of the O-H and O-D stretching vibrations in SrTiO3 under applied electric field and uniaxial stress. *Phys. Rev. B*, 34(12):8406–8417.

[Weber et al., 1998] Weber, R. T., Jiang, J., and Barr, D. P. (1998). Bruker Emx User's Manual.

[Wild et al., 1973] Wild, R. L., Rockar, E. M., and Smith, J. C. (1973). Thermochromism and Electrical Conductivity in Doped SrTiO3. *Phys. Rev. B*, 8(October):3828–3835.

[Williams, 1971] Williams, R. (1971). Photoconductivity in Photochromic Strontium Titanate. *J. Appl. Phys.*, 42(3):1131.

[Yamada and Miller, 1973] Yamada, H. and Miller, G. R. (1973). Point defects in reduced strontium titanate. *J. Solid State Chem.*, 6(1):169–177.

APPENDIX

A. Kelvin Probe Force Microscopy (KPFM)

The work function ϕ is the minimum energy needed to remove an electron from the surface of the material to just outside of it, usually measured in eV. When two different materials are brought into electrical contact, electrons will flow from the material with the lower work function to the higher one, until the Fermi energies are equal. The difference in work functions between two materials is call the contact potential difference (CPD). Kelvin probe force microscopy (KPFM) measures the local CPD between the sample and the conducting atomic force microscopy (AFM) tip [Melitz et al., 2011]. An external potential, V_c, can be applied to make the surface charges disappear. At equilibrium the electric field is zero and the externally applied potential equals the CPD. If we know the work function of the reference plate ϕ_1, the work function of the sample can be determined, $\phi_2 = \phi_1 - qV_c$, where q is the elementary charge [Palermo et al., 2006]. AFM measurements are also taken during the KPFM measurement process. The sample and the probe tip form a capacitor. The force between them is:

$$F_e = -\frac{1}{2}\frac{\partial C}{\partial z}(\triangle V)^2 \tag{1}$$

where z is the direction normal to the sample surface, F_e is the electric force, C is the capacitance, and $\triangle V$ is the potential difference between the sample and probe.

Vertically vibrating the probe tip causes the capacitance to vary as the distance changes, which causes charges to flow and gives rise to an AC current, $I(t)$, that can be detected. This current is given by:

$$I(t) = V_c \omega \triangle C cos(\omega t) \tag{2}$$

where V_c is the contact potential difference and $\triangle C$ is the change in capacitance.

Scanning the tip over the surface allows very high resolution images to be constructed. An alternating voltage is applied to the tip with frequency ω. The oscillations of the tip is recorded with a laser. The electrostatic tip and sample interaction introduces mechanical oscillations of the cantilever. These oscillations are isolated using a lock-in amplifier and sent to a feedback circuit. The feedback circuit tries to minimize the force from the sample and tip interaction by adding a DC voltage, V_{DC}, to the sample. when the ω component of the electrostatic force interaction is zero, V_{DC} is equal to the difference in work function between the sample surface and the tip ($V_{DC} = \triangle\phi$).

KPFM measurements were performed in Dr. Yi Gu's lab by Shengwen Zhou and Qiaoming Wang at WSU. They have a CryoView 2000 Nanonics Platform AFM that operates in intermittent (tapping) mode. It uses frequency modulation for detecting the signal.

B. KPFM Results

With KPFM we looked at as received pure STO samples, and PPC samples before and after light exposure. For each measurement, the scan was conducted at 0, 1 and 2 Volts DC bias. Two different geometries for the conductive contact were employed in the measurement: (1) two strips on the front side and (2) a back contact. In the two strip method, strips of silver paint were applied to opposite ends of the sample. One strip forms the biased electrode and the other one is floated. Scans of the chip were taken near the biased electrode. In the back contact geometry silver paint is applied to the back side of the chip and forms the biased electrode. Another strip is painted in the middle on the front side and is floated.

As received samples measured with the back contact geometry (Figures 77 and 78) show an average surface potential around 0.28 V regardless of applied bias. These results may not make a lot of sense because the chip is very insulating. Additionally, we see a relatively homogeneous surface with only a few small nodules present.

Next we looked at SrO annealed samples before and after light exposure. Figure 79 shows the surface and its potential before light exposure in the strip geometry. Here we observe nodules on the surface approximately 300 nm high and around 800 nm wide. Since they are not seen in as received samples its probable that they grow on the surface during our annealing procedure. This chip was measured with 0, 1, 2 Volts bias before and after light. The images are all roughly the same, but the surface potential is different in each case. The values are given in Table B.1. The choice of applied bias affects the difference observed with light exposure. This is because the

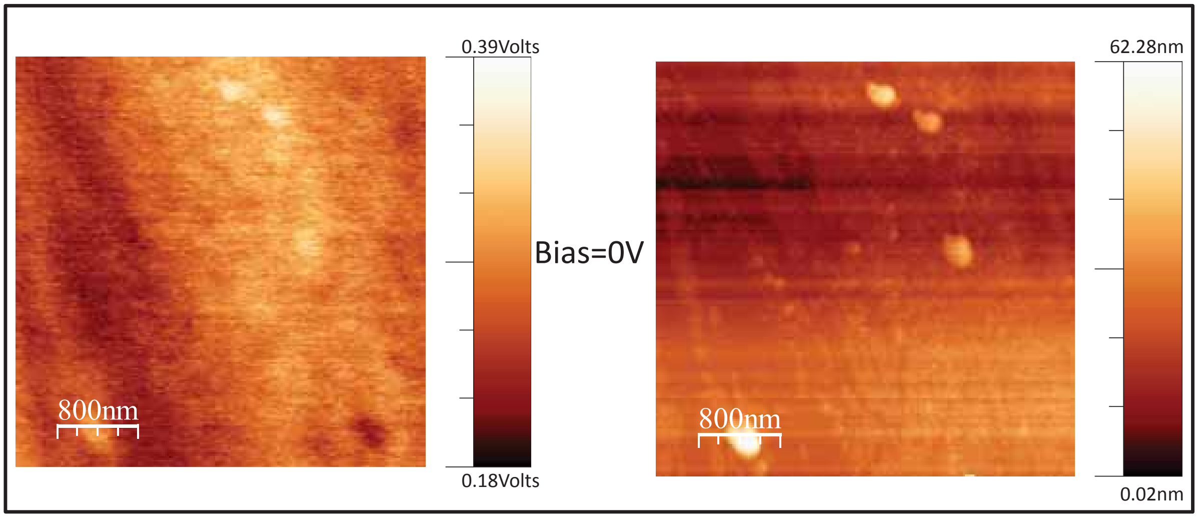

Figure 77: KPFM measurements on as-received sample at 0 Volts bias. Left: local potential map, Right: AFM of the surface topography.

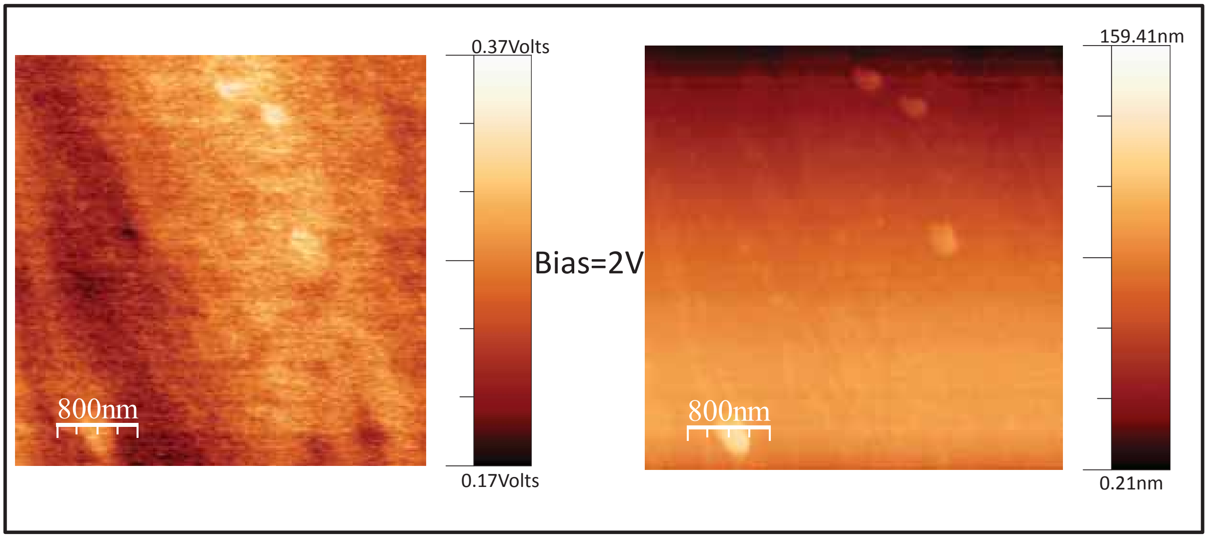

Figure 78: KPFM measurements on as received sample at 2 Volts bias. Left:local potential map, Right: AFM of the surface topography.

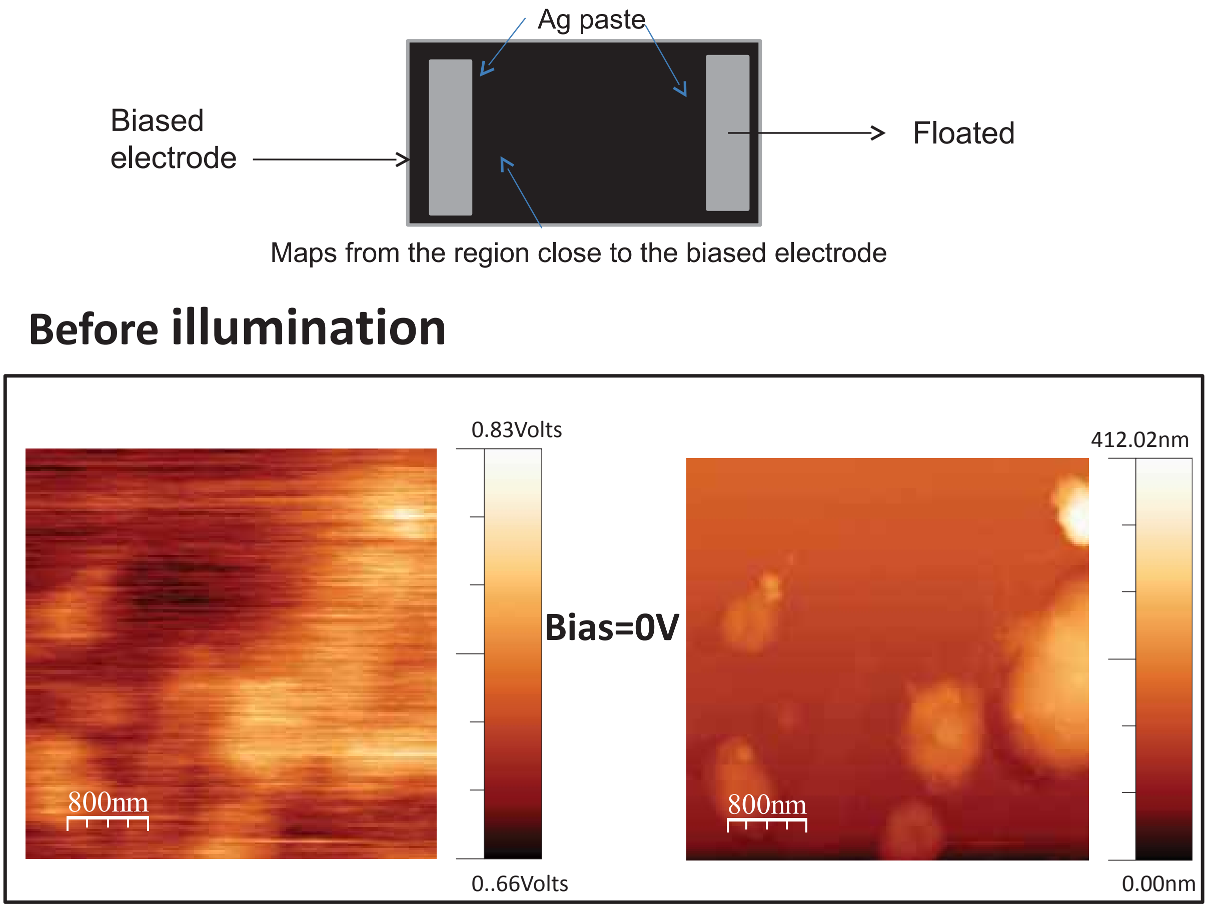

Figure 79: KPFM measurements before light in the strip geometry with 0 Volts bias. Top shows the geometry of the measurements. Left: the local potential map, Right: AFM of the surface topography.

region scanned is right next to the biased electrode.

Performing measurements in the back contact geometry give more consistent results, regardless of applied bias. For the 0 Volts bias, there is a potential increase of ~ 0.11 V, where for the 2 Volts bias a potential increase of 0.10 Volts is observed. Figures 80 and 81 show the measurements before and after light, respectively, for a bias of 2 Volts. Here the surface nodules are even bigger than in the previous sample.

The increase in surface potential observed upon light exposure is consistent with our other measurements. Before light exposure, electrons occupy acceptor levels low in the band gap and the resistivity is high. After light exposure, electrons are promoted to the conduction band, as evidenced by the appearance of the peaks in the UV Vis, and the resistivity dropping dramatically.

Table B.1: Surface potentials before and after illumination on SrO annealed sample with 0, 1 and 2 Volts bias in the strip geometry. All values are given in Volts.

Surface Potential		Applied	
Before light	After Light	Bias	Difference
0.719	0.919	0	0.2
1.593	1.696	1	0.11
2.415	2.408	2	~ 0

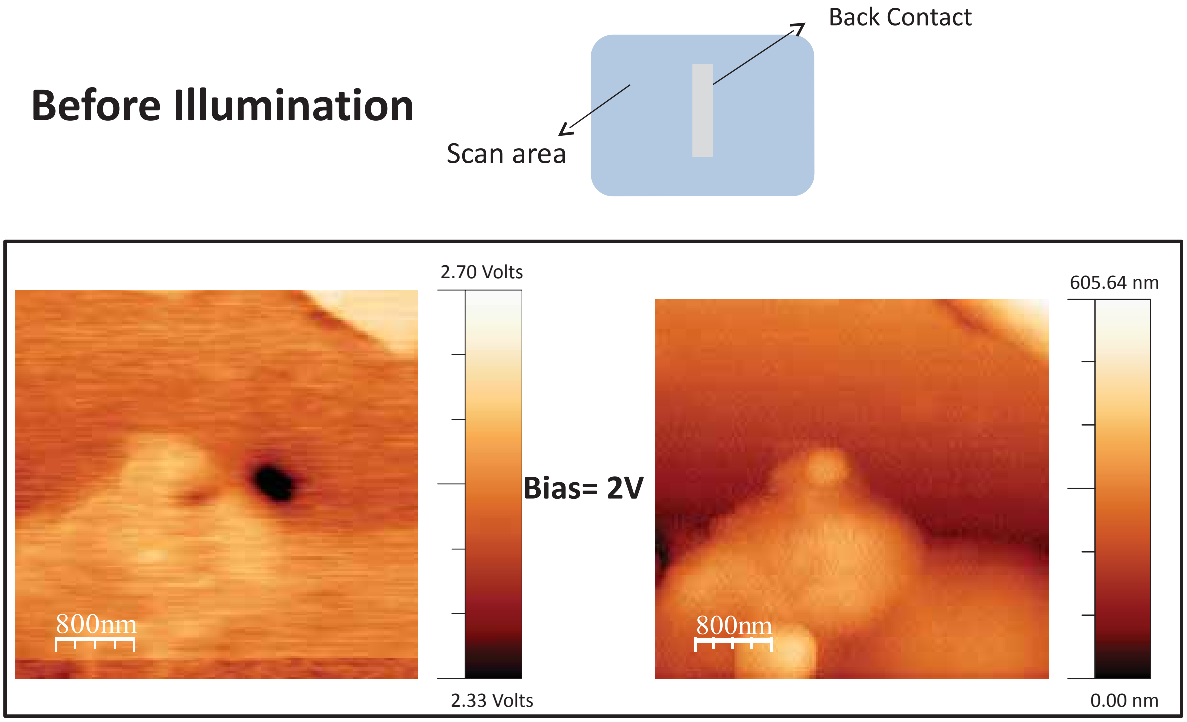

Figure 80: KPFM measurements before light in the strip geometry with 2 Volts bias. Top shows the geometry of the measurements. Left: local potential map, Right: AFM of the surface topography.

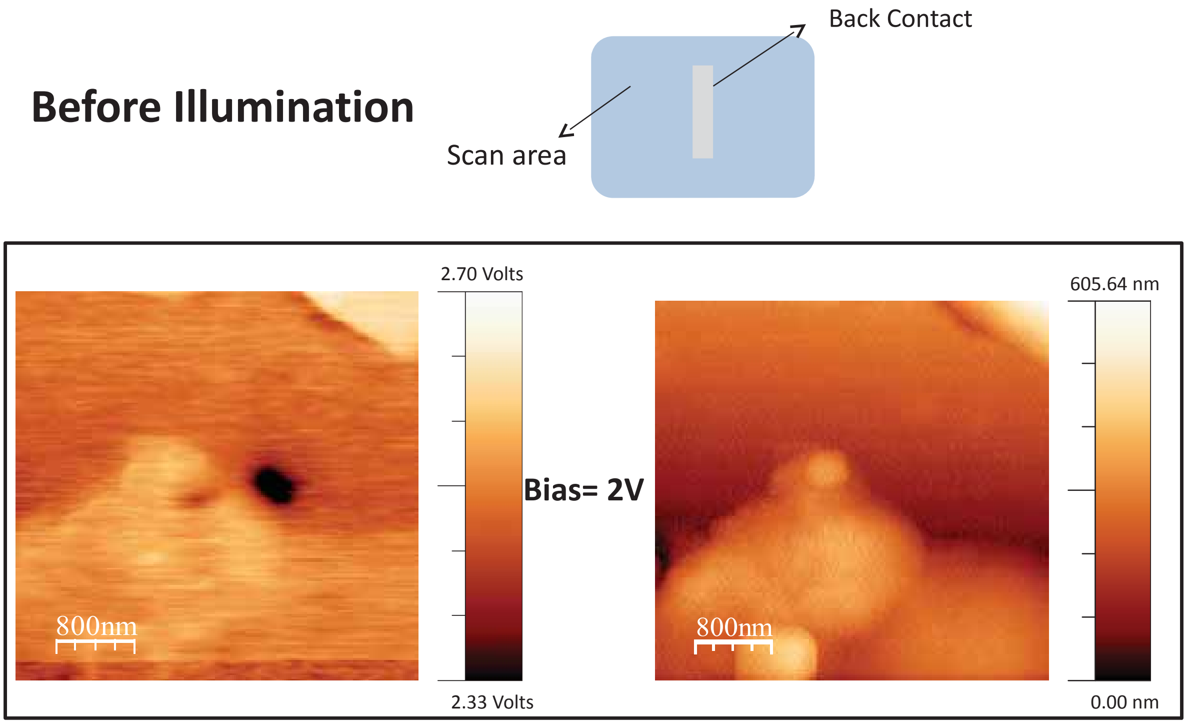

Figure 81: KPFM measurements after light in the strip geometry with 2 Volts bias. Left shows the local potential map and Right shows the AFM of the surface.

This corresponds to an increase in the surface potential. The most interesting result of these measurements is that surface features appear on annealed chips. Szot et al. [Szot and Speier, 1999] observed surface changes, specifically the formation of chemically inhomogeneous regions on chips annealed above 1000°C in either reducing or oxidizing condition that were quickly cooled. There chips had significantly smaller growths on the surface than we observe, around 50 to 100 nm. These surface growths might be SrO powder from the anneal, or outgrowths of the crystal lattice, STO, that form as SrO migrates inward and Ti outwards during the anneal. Diffusion kinetics of the atoms during annealing are briefly touched on in Chapter 8.

C. Free Carrier Line Shape in STO

A small part of this appendix section has been previously published. [1]

Figure 82 shows the increase in free-carrier absorption as an SrO annealed STO sample is exposed to 405 nm light. Absorbance was calculated as $\log_{10}(I_0/I)$, where I_0 and I are the transmitted intensities for the sample before and after light exposure, respectively.

The dip around 1325 cm^{-1} is due to a strong peak in the sample, probably due to two-phonon absorption. Brebner [Brebner et al., 1981] observed this peak in nominally pure samples. It is attributed to an electronic transition at a localized defect. The smaller dip around 1765 cm^{-1} may be a phonon replica of the 1325 cm^{-1} line [Rochon et al., 1979]. Both features are weakly Raman active [Nilsen and Skinner, 1968, Rochon et al., 1979] so the defect must lack inversion symmetry, and is therefore non-hydrogenic in nature [Brebner et al., 1981]. Rochon et al. and references within [Rochon et al., 1979] believe the line is due to an excitation of a defect with simultaneous emission, since similar behavior occurs in a variety of other ionic crystals, doped with various impurities.

The broad peak near 2200 cm^{-1} was tentatively attributed to a defect state by Okamura et al [Okamura et al., 2006]. Overall, the increase in free-carrier absorption due to PPC is proportional to exposure time. Unlike Okamura's study, after an SrO anneal the photo-induced change results from below band gap light and persists long after the light is turned off.

This broad shaped absorption band also occurs in vacuum annealed samples (Figure 83). The vacuum anneal was performed at a low level of vacuum to limit the conductivity, so some signal could still be seen through the chip. Then the sample was erased on a hot plate, and the spectra was taken again. The erased chip is taken as the reference for the absorbance to more easily compare to the increase in conductivity that occurs in PPC samples. This shows that the defect states responsible for this broad absorption band do not depend on the type of anneal. Once again we see features around 1325 cm^{-1} and 1765cm^{-1}, only now they are peaks rather than dips.

Overall, the broad absorption band we see in the infrared demonstrates that there are many in gap states distributed over a wide range of energies, that reach to the band edges

---

[1] V. M. Poole, M. D. McCluskey. Large persistent photoconductivity in strontium titanate single crystals. *Proc. SPIE 9749,* Oxide-based Materials and Devices VII, 97490N (February 27, 2016): doi:10.1117/12.2207714

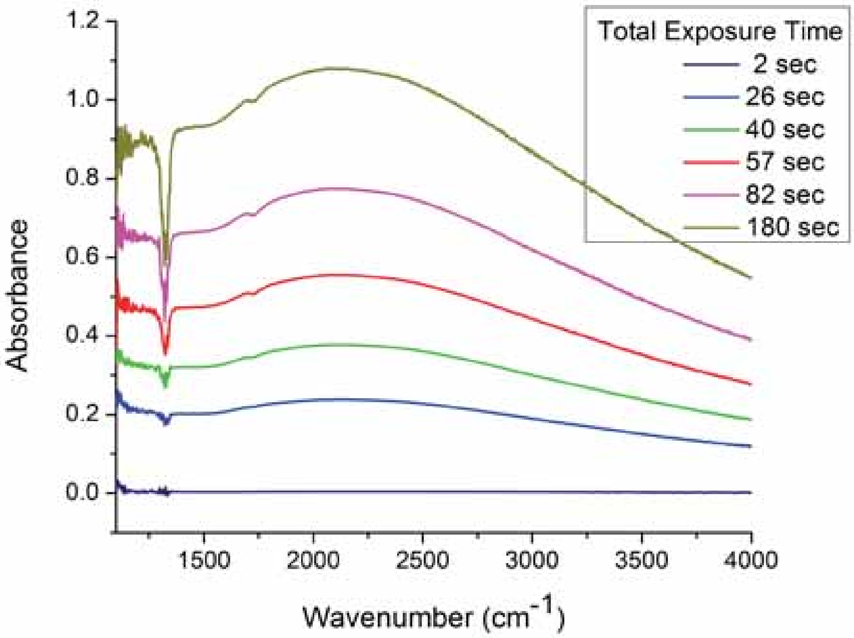

Figure 82: Room temperature IR spectra showing the increase in absorbance as a STO sample is exposed to 405 nm light.

[Okamura et al., 2006]. Both vacuum annealed samples and PPC samples have many free carriers, so this might be the shape free carrier absorption takes in STO. Baer's [Baer, 1966] initial study of free carrier absorption in STO observed increasing optical absorption with increasing wavelength, up to 5 μm. This is approximately 2000 cm^{-1}, which is around where our observerd broad absorption band turns downwards. Two sharper lines were observed, which may correspond to an electronic transition localized to a defect, and a phonon replica of it. Other phonon replicas seen by Rochon [Rochon et al., 1979] and Brebner [Brebner et al., 1981] were not observed.

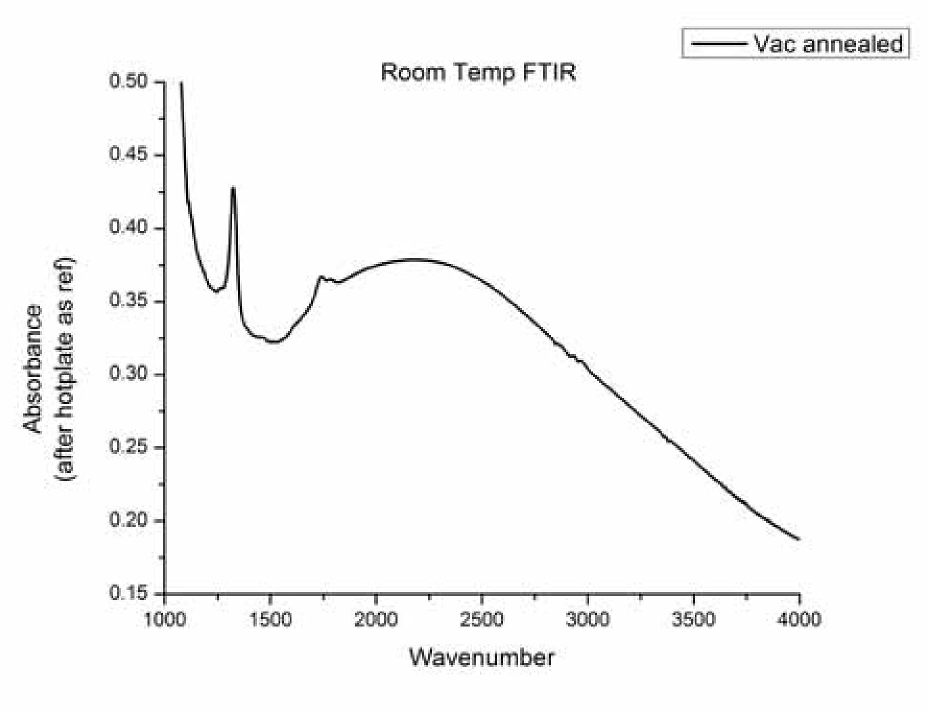

Figure 83: FTIR absorbance spectra with MCT detector of STO sample. The reference is taken as the sample after erasure with a hot plate.